UNIVERSITY OF ROCHESTER
LABORATORY FOR LASER ENERGETICS

Volume 112
July–September 2007
DOE/SF/19460-790

LLE Review

Quarterly Report

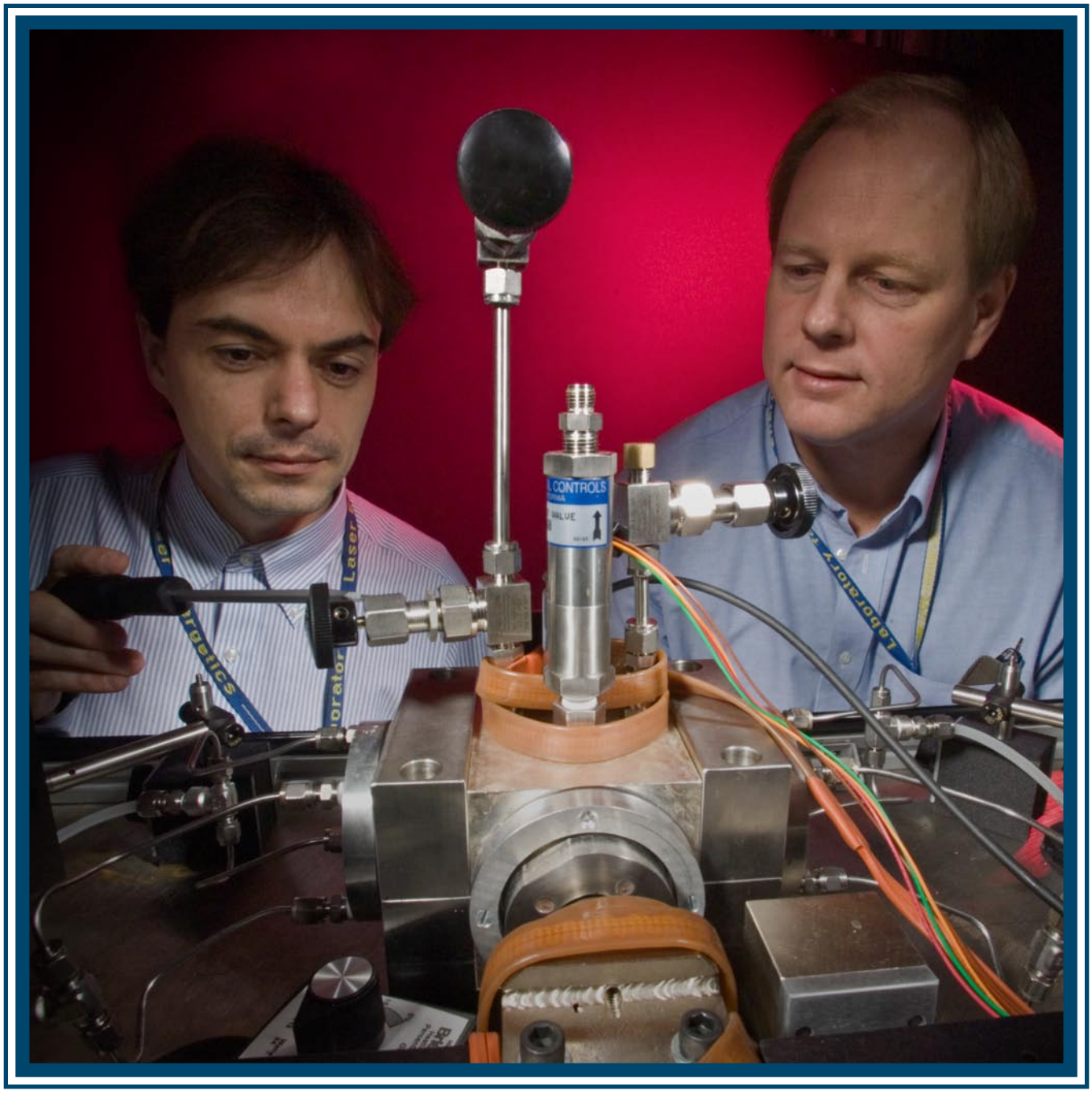

About the Cover:

A high-spatial-resolution neutron detector, based on a high-pressure freon bubble chamber, is being developed at LLE to image the 14-MeV neutrons emitted from the hot-spot region of fusion experiments on the OMEGA Laser System (see **Aperture Tolerances for Neutron-Imaging Systems in Inertial Confinement Fusion** on p. 203). As high-energy neutrons scatter in the supercritical freon, the ion recoil deposits energy locally (within a few microns of the scatter site), raising the temperature above the boiling point and forming a single bubble that quickly grows to more than 100 μm in diameter. The density distribution of these bubbles reflects the spatial distribution of the incident neutron flux. Graduate student Marian Ghilea is shown pointing to connectors and valves used to pressurize and fill the chamber with freon, while LLE Senior Scientist Craig Sangster looks on. A series of pressure and temperature sensors and the overpressure relief valve are found on top of the custom aluminum block that houses the bubble chamber. Water heated to 60°C is circulated within the aluminum housing and around the bubble chamber to maintain a uniform temperature throughout the freon.

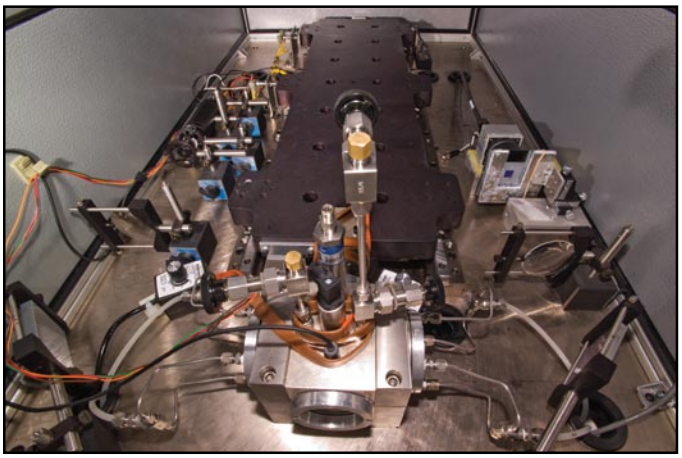

A top-down view of the bubble chamber and the imaging optics is shown. The linear motor used to drive the chamber expansion mechanism (to rapidly adjust the pressure in the freon at shot time) dominates the central area of the optical table. A 653-nm laser is used to probe the bubble density distribution using the Schlieren technique (the bubble density will be too high to count them individually). With proper timing, it should be possible to image the bubble distribution when the bubbles have grown to approximately 100 μm in diameter. The anticipated spatial resolution will be significantly better than more-conventional pixelated scintillator arrays that have a typical resolution of one millimeter. The higher detector spatial resolution will reduce the magnification requirements for neutron-imaging systems on OMEGA and the NIF. Lower magnification requirements relax some of the more costly design constraints for these ignition-relevant diagnostics.

This report was prepared as an account of work conducted by the Laboratory for Laser Energetics and sponsored by New York State Energy Research and Development Authority, the University of Rochester, the U.S. Department of Energy, and other agencies. Neither the above named sponsors, nor any of their employees, makes any warranty, expressed or implied, or assumes any legal liability or responsibility for the accuracy, completeness, or usefulness of any information, apparatus, product, or process disclosed, or represents that its use would not infringe privately owned rights. Reference herein to any specific commercial product, process, or service by trade name, mark, manufacturer, or otherwise, does not necessarily constitute or imply its endorsement, recommendation, or favoring by the United States Government or any agency thereof or any other sponsor. Results reported in the LLE Review should not be taken as necessarily final results as they represent active research. The views and opinions of authors expressed herein do not necessarily state or reflect those of any of the above sponsoring entities.

The work described in this volume includes current research at the Laboratory for Laser Energetics, which is supported by New York State Energy Research and Development Authority, the University of Rochester, the U.S. Department of Energy Office of Inertial Confinement Fusion under Cooperative Agreement No. DE-FC52-92SF19460, and other agencies.

Printed in the United States of America
Available from
National Technical Information Services
U.S. Department of Commerce
5285 Port Royal Road
Springfield, VA 22161
Price codes: Printed Copy A05
Microfiche A01

For questions or comments, contact Tanya Kosc, Editor, Laboratory for Laser Energetics, 250 East River Road, Rochester, NY 14623-1299, (585) 273-3185.

Worldwide-Web Home Page: http://www.lle.rochester.edu/

UNIVERSITY OF ROCHESTER
LABORATORY FOR LASER ENERGETICS

Volume 112
July–September 2007
DOE/SF/19460-790

LLE Review

Quarterly Report

UR LLE

Contents

In Brief iii

Aperture Tolerances for Neutron-Imaging Systems in Inertial Confinement Fusion 203

Hohlraum Energetics and Implosion Symmetry with Elliptical Phase Plates Using a Multicone Beam Geometry on OMEGA 212

Improved Measurement of Preheat in Cryogenic Targets 216

Laser Channeling in Millimeter-Scale Underdense Plasmas of Fast-Ignition Targets 222

Optimizing a Cleaning Process for Multilayer Dielectric (MLD) Diffraction Gratings 228

Shock Ignition of Thermonuclear Fuel with High Areal Densities 234

LLE's Summer High School Research Program 238

FY07 Laser Facility Report 240

National Laser Users' Facility and External Users' Programs 242

Publications and Conference Presentations

In Brief

This volume of the LLE Review, covering July–September 2007, features "Aperture Tolerances for Neutron-Imaging Systems in Inertial Confinement Fusion," by M. C. Ghilea, T. C. Sangster, and D. D. Meyerhofer, along with R. A. Lerche (Lawrence Livermore National Laboratory) and L. Disdier (Commissariat à L'Énergie Atomique). Neutron-imaging systems are being considered as an ignition diagnostic, which is vital to the inertial confinement fusion effort (p. 203). Given the importance of these systems, a neutron-imaging design tool is being used to quantify the effects of aperture fabrication and alignment tolerances on reconstructed neutron images for inertial confinement fusion. The simulations indicate that alignment tolerances of more than 1 mrad would introduce measurable features in a reconstructed image for both pinholes and penumbral aperture systems. Simulated fabrication errors suggest that penumbral apertures are several times less sensitive to these errors than pinhole apertures.

Additional highlights of recent research presented in this issue include the following:

- S. P. Regan, T. C. Sangster, D. D. Meyerhofer, W. Seka, R. Epstein, S. J. Loucks, R. L. McCrory, C. Stoeckl, and V. Yu. Glebov, along with O. S. Jones, D. A. Callahan, P. A. Amendt, N. B. Meezan, L. J. Suter, M. D. Rosen, O. L. Landen, E. L. Dewald, S. H. Glenzer, C. Sorce, S. Dixit, R. E. Turner, and B. J. MacGowan (LLNL) discuss hohlraum energetics and implosion-symmetry experiments conducted using laser beams arranged in three cones and smoothed with elliptical phase plates (p. 212). A shift in symmetry was observed between vacuum and gas-filled hohlraums having identical beam pointing. The ratio of x-ray drive at the poles of the capsule relative to the waist increased for the gas-filled hohlraum.

- B. Yaakobi presents an improved measurement of preheat in cryogenic targets (p. 216). A reformulated and more consistent analysis of preheat measurements is performed, and the sensitivity of the results to the assumptions made in the analysis is discussed. The results are applied to both cryogenic as well as to CH targets.

- G. Li, R. Yan, and C. Ren, along with T.-L. Wang, J. Tonge, and W. B. Mori (University of California, Los Angeles) used two-dimensional particle-in-cell simulations to show that laser channeling in millimeter-scale underdense plasmas is a highly nonlinear and dynamic process (p. 222). This process involves laser self-focusing and filamentation on the electron time scale, ponderomotive plasma blowout in the filaments, eventual whole beam blowout that transversely launches high-mach-number shocks, longitudinal plasma snowplowing, laser hosing, and channel bifurcation and self-correction.

- B. Ashe, C. Giacofei, G. Myhre, and A. W. Schmid describe the development and the optimization of the cleaning process that removes a wide variety of organic (photoresist) materials, metals, and metal oxides, which commonly remain on the surface of multilayer dielectric (MLD) diffraction gratings (p. 228). The removal of such contaminants, a number of which have a significant optical absorbance and can lead to laser-induced damage, is critical to the performance of the OMEGA EP Laser System.

- R. Betti, W. Theobald, C. D. Zhou, K. S. Anderson, P. W. McKenty, S. Skupsky, D. Shvarts, V. N. Goncharov, J. A. Delettrez, P. B. Radha, T. C. Sangster, C. Stoeckl, and D. D. Meyerhofer (LLE and the Fusion Science Center for Extreme States of Matter and Fast Ignition Physics) researched the shock ignition of thermonuclear fuel with high areal densities (p. 234). In direct-drive inertial confinement fusion (ICF), the "ignitor" shock can be launched by a power spike at the end of the laser pulse. For targets with the same adiabat and implosion velocities, the laser energy required for ignition is significantly lower for shock-ignition ICF than for standard ICF.

- This volume concludes with a summary of LLE's Summer High School Research Program (p. 238), the FY07 Laser Facility Report (p. 240), and the National Laser Users' Facility and External Users' Programs (p. 242).

Tanya Z. Kosc
Editor

Aperture Tolerances for Neutron-Imaging Systems in Inertial Confinement Fusion

Introduction

The inertial confinement fusion (ICF) approach to fusion ignition relies on inertia to compress the fuel to ignition conditions. A major goal of ICF research is the generation of net energy by imploding targets containing deuterium–tritium (DT) fuel, using lasers, x rays generated by lasers, pulsed power, or ion beams.[1] To achieve ignition, it is necessary for the target irradiation to be as symmetric as possible, minimizing hydrodynamic instabilities that reduce the implosion efficiency. To validate simulations of the implosions, one must measure or infer the density and temperature distribution of the fuel at peak compression.[2] This requires a number of target diagnostics that typically utilize x rays and fusion-reaction products emitted from the core.[3–5]

For example, an x-ray image of an ICF core provides information about the spatial structure of several complex processes within the target that are directly related to the fusion reactions. The x-ray image depends on the spatial and temporal profiles of plasma density and electron temperature. Diagnostics based on neutron emission provide a direct measure of the fusion burn region. These diagnostics are used to infer the fuel areal density, neutron yield, fuel ion temperature, and bang time.[2] The spatial distribution of the burning fuel can be directly determined by imaging the primary and scattered neutron emission from the core[6] (in this context, primary neutron images are based on the thermally broadened 14-MeV neutron emission from D-T fusion reactions in the core, while scattered neutron images are based on primary neutrons that scatter from the dense fuel to energies well below the 14-MeV line emission; these neutrons provide an image of the cold-fuel distribution in a non-igniting implosion). A neutron image is obtained by placing an appropriate aperture in front of a spatially sensitive neutron detector. These apertures typically code the spatial distribution from the source by differentially attenuating the neutron flux. The reconstruction of the core image requires precise knowledge of the aperture geometry.[7] Neutron imaging would be used to identify ignition-failure mechanisms such as poor implosion symmetry or inadequate convergence/areal density. Neutron imaging is used on the OMEGA[7] laser to measure the core symmetry of gas-filled plastic shells and energy-scaled, ignition-relevant cryogenic target implosions.[8]

A spatially sensitive neutron detector can be based on an array of scintillators or on a bubble chamber.[9] For a required image resolution, the system design considerations include magnification, the signal-to-noise (S/N) ratio, aperture-alignment accuracy, aperture-fabrication tolerances, neutron energy, neutron yield, field of view, and the detector spatial resolution. Here the S/N ratio refers to unwanted neutron signals from scattering sites near the imaging line of sight. This noise typically scales with the signal (primary yield) and can be reduced by shielding the detector. The impact of this noise can be further reduced by acquiring a flat-field (i.e., no aperture) image in a high-field implosion. For the work presented here, no attempt was made to include a neutron noise component in the simulations. For ICF experiments on laser facilities such as OMEGA[7] and the National Ignition Facility (NIF),[10] optimization of the system design is a complex process and understanding the effects and trade-offs of component tolerances requires simulations and image analysis. This article will discuss system design considerations and will focus on the resolution limitations introduced by the aperture alignment and fabrication tolerances.

Design Considerations for Neutron Imaging for ICF

Neutron-imaging (NI) systems use extended pinholes or penumbral apertures (with annular apertures as a particular case of the second) to generate images on the detector plane.[6] A full system consists of a neutron source, an aperture, an alignment system, and a neutron-sensitive detector (Fig. 112.1). When the neutrons pass from the source through the aperture, their spatial intensity at the detector plane is modulated according to the shape of the aperture. The alignment and type of aperture define the image size, shape, and resolution on the detector plane. The aperture's three-dimensional shape is described by a two-variable point-spread function (PSF). The magnification M of the system is the ratio of source–detector distance L divided by the source-aperture distance ℓ.

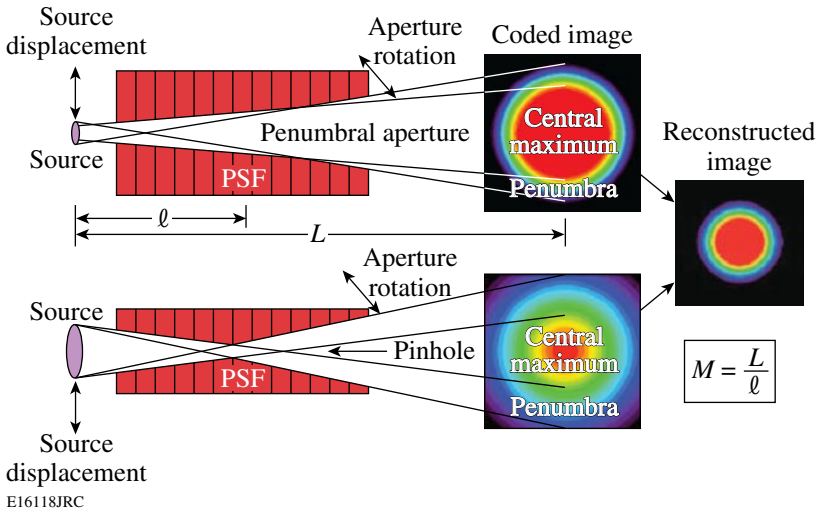

Figure 112.1
Schematic diagrams of penumbral and pinhole-imaging devices. The functional information for source-image reconstruction comes from the penumbral area of the image on the detector plane (except for the case when the pinhole is much smaller than the source). The magnification of the system M is the ratio of the source–detector distance L divided by the source-aperture distance ℓ.

1. Pinhole Imaging

Neutron-based pinhole imaging works on the same principle as an optical pinhole camera, with the source image directly displayed on the detector. Additional processing is required for a pinhole diameter comparable to or larger than the desired resolution. Due to the finite neutron range inside the materials, the pinhole is extended radially and not limited to a single plane along the observation axis. The image on the detector plane consists of a central maximum surrounded by a large penumbra. The small diameter (typically of the order of 10 μm) of the aperture makes it difficult to fabricate the aperture with the required precision and constitutes one of the main sources of error in the measured/reconstructed image. Relative to a thin aperture (e.g., an optical pinhole), it is more difficult to obtain a clear image due to the finite depth of focus of a neutron aperture (a neutron aperture simply attenuates the neutron flux rather than blocking it from reaching the detector). The image may directly represent the source, as it does for an optical pinhole camera, but it is formed from only those neutrons passing through a small aperture, limiting the resolution and S/N ratio for low-yield (for example, $\leq 10^{14}$) implosions.[11]

2. Penumbral Imaging

Penumbral imaging with an aperture larger than the source size is a coded-aperture-imaging technique (i.e., the image seen on the detector's plane is not the exact representation of the source but is defined by the PSF of the aperture).[5] With a penumbral aperture, the image consists of a uniform, bright central region surrounded by a partially illuminated penumbra. The source image is encoded in the penumbra of the detected image (the bright central region receives signals from the entire source area and does not provide spatial information). The diameter of a penumbral aperture is typically larger than the source and, therefore, for a comparable resolution, should be easier to fabricate, characterize, and align than a pinhole. Due to the larger solid angle, the image is formed from many more neutrons than for a pinhole; therefore, for a given yield, it typically has an intrinsically higher S/N ratio.[12]

The coded image must be deconvolved to produce an image of the neutron source. This process requires precise knowledge of the aperture point-spread function and the flat-field response of the imaging detector.[6] Therefore, a penumbral aperture is designed to be as isoplanatic as possible. This means that the aperture PSF is independent of the source point in the field of view. In practice, this is difficult to do and is the primary reason for the study of alignment sensitivity.

For both types of apertures, uncertainties in the exact shape (due to finite fabrication tolerances) lead to errors in the reconstructed image due to uncertainties in the calculated PSF. For brighter neutron sources (neutrons per source element), the S/N ratio improves faster for pinholes than for penumbral apertures, making pinholes the preferred aperture type of very high yield (for example, $\geq 10^{16}$) ICF imaging.[10]

Reconstruction of the Detector-Plane Image

Nyquist's theorem states that in order to accurately reconstruct a signal based on periodic sampling, the sampling frequency must be at least twice the maximum frequency of the signal. This limits the maximum resolution of a pixelated imaging system to $2\delta(\text{pixel})/M$, where M is the magnification of the system and $\delta(\text{pixel})$ represents the pixel resolution on the image plane.[13] To diminish the effect of image aliasing (i.e., pixelation of image), various anti-aliasing techniques can be

applied. The numerical noise in the signal (in this case the noise is associated with the image reconstruction) is typically given by Poisson statistics, and its reduction requires low-bandpass filtration; i.e., the signal has a frequency higher than a conveniently chosen cutoff value.[14]

In the neutron-detection measurements associated with imaging, random errors arise from various sources, such as misalignment, detector noise, etc. In most of the cases, a Gaussian distribution, or other similar type, can be used to characterize the random errors encountered. The standard deviation of the distribution is used as a measure of the uncertainty. For a neutron image, the relevant sources of error are due to the detector noise (typically associated with flat-field statistics), aperture alignment, pixel resolution of the detector, and the recoil distances of the nuclei in the detector. Therefore, the overall measurement uncertainty is given by[14]

$$\sigma_s = \sqrt{\sigma_{\text{noise}}^2 + \sigma_{\text{align}}^2 + \sigma_{\text{pixel}}^2 + \sigma_{\text{rec}}^2}\,, \tag{1}$$

where the indices *noise*, *align*, *pixel*, and *rec* represent the errors induced by noise, alignment, pixel, and recoil distance. The resolution of the system (i.e., the scale of the smallest resolvable point in the source under ideal conditions) can be written based on similar assumptions. Because the error given by Poisson statistics is inversely proportional to the cutoff frequency k_c (at which point the noise starts to dominate), the resolution of the imaging system can be written as[14]

$$\delta_s = \sqrt{\frac{1}{k_c^2} + \delta_{\text{align}}^2 + \left(\frac{2\delta_{\text{pixel}}}{M}\right)^2 + \left(\frac{\delta_{\text{rec}}}{M}\right)}\,, \tag{2}$$

where M is the magnification of the system and δ_{align}, δ_{pixel}, and δ_{rec} are the resolution components given by alignment error, the finite pixelation of the detector, and the particle recoil distance from the interaction of the neutrons with the detector medium. A neutron-imaging system could, in principle, achieve an improved resolution by using a high magnification, but a higher value for M increases the sensitivity to alignment errors. Keeping the other parameters fixed, a large target–aperture distance provides a better resolution as M increases in Eq. (2). Higher neutron yields increase the value of k_c in Eq. (2) and decrease the resolution limit of the instrument.

A coded penumbral image and, in most cases, a coded pinhole image on the detector plane can be deconvolved using an inverse Fourier transform.[5] By considering the magnified image of the source without any penumbral blurring as a function of coordinates $f(x,y)$ and the image created by a point source (or the PSF) as $g(x,y)$, an image on the detector plane $h(x,y)$ is created through the convolution of the first two functions:

$$\begin{aligned} h(x,y) &= f(x,y) \circ g(x,y) \\ &= \iint f(x',y')\,g(x-x',y-y')\,dx'\,dy'. \end{aligned} \tag{3}$$

A deconvolution of the source image can be obtained by using the convolution theorem of the Fourier transform. Since $H(k,l) = \mathrm{F}(k,l)\,G(k,l)$, with H, F, G the Fourier transforms of h, f, g,

$$\mathrm{F}(k,l) = \frac{H(k,l)}{G(k,l)}\,, \tag{4}$$

and the source image becomes

$$f(x,y) = \mathrm{F}^{-1}\left[\frac{H(k,l)}{G(k,l)}\right] = \mathrm{F}^{-1}\left\{\frac{\mathrm{F}\left[h(x,y)\right]}{\mathrm{F}\left[g(x,y)\right]}\right\}, \tag{5}$$

where F and F^{-1} are the Fourier and inverse Fourier transforms. A Wiener filter[12] can be used to reduce the noise levels by replacing

$$G(k,l) = \mathrm{F}\left[g(x,y)\right] = \frac{\left|H(k,l)\right|}{\left|H(k,l)\right|^2 + \gamma}\,, \tag{6}$$

where γ is an arbitrary correction factor (always positive) chosen to minimize the noise on the reconstructed image.

Neutron-Imaging Design Tool

To investigate the influences of various parameters of a NI system on the quality of the reconstructed image, a design tool has been developed. The code was written in PV Wave [http://www.vni.com], and Eqs. (5) and (6) have been used to reconstruct the encoded image. The source and detector plane are described by arrays that define the maximum theoretical system resolution. Various source distributions and intensity profiles can be generated. Noise can be added to simulate neutron background, but for the work presented here no neutron-related noise was added (any such noise can be subtracted from the image recorded on the detector plane). The aperture is described as a succession of thin layers with fixed openings along the particle-flux direction, and the resulting image on the detector plane is created by summing the neutron attenuations of the individual layers. A PSF for the aperture is generated by

ray tracing between the array elements of source and detector. The rays are treated as optical, to precisely define the thin-layered edges of each aperture. In this way, a variety of apertures can be simulated (pinholes and penumbral, cylindrical, biconic, or annular). The only limitation for the simulations is the available computational power. Fabrication and alignment tolerances can be determined by direct simulation using realistic source distributions and detector responses.

The simulations consist of defining a source distribution (shape and brightness) using an array of small source elements (the pixel size in the source is smaller than the system resolution) and calculating the PSF using ray tracing between the source elements and the detector elements (pixels). The pixelation of the detector is typical for existing neutron-imaging systems. The shapes of the reconstructed images can then be compared with the original source to determine if features associated with the aperture shape and alignment would be measurable in an actual imaging system.

For any NI system, several factors determine the characteristics of the image on the detector plane and those of the reconstructed image: The magnification determines the size of the image on the detector plane. If a large magnification is achieved by increasing the source-to-detector distance, a larger detector for a given source size or field of view is required. The aperture regulates the neutron flux on the detector. Its size determines, as much as the magnification, the dimension of the image on the detector plane for penumbral imaging systems. The aperture thickness and material determine its leakage to neutrons, and its shape controls the characteristics of the coded image and, therefore, the accuracy of the deconvolution process. The aperture is also sensitive to misalignment and can also be simulated. Another factor is the sensitivity of the recording medium. Apart from any intrinsic pixel resolution imposed by the detector dimensions, the detector resolution is ultimately limited by the recoil length of the elastically scattered nuclei at the detector material (e.g., protons in a CH-based scintillator). The last two factors to be taken into consideration are the neutron-scattering sources near the imaging line of sight and the field of view (limits resolution via the PSF).

Specific Examples

This design tool has been tested against simple cases having analytical solutions. Good agreement between the analytic calculations and numerical simulations suggests that the technique can be applied to complex aperture assemblies. For a point source, a perfect fit was obtained between the reconstructed and the analytically calculated images. For a circular flat source (constant brightness), the relative difference between the reconstructed and the analytically calculated images was in the range of 1% (due to the fact that the circular source was approximated by an array and its element centers were either outside or inside the source radius, changing the calculated values of the inverse Fourier transform), as shown in Fig. 112.2.

Data images from implosions generated by OMEGA shots were reconstructed using the technique described above [Fig. 112.3(a)] and compared with the results obtained by using the method described in Ref. 14 (filtered autocorrelation) and shown in Fig. 112.3(b). The biconic aperture used had a 200-μm field of view (FOV), a thickness of 100 mm, and a central diameter of 2 mm. The measured diameter of the neutron source size was ~50 μm, the source–aperture distance was 26 cm, and the source–detector distance was 800 cm, yielding a magnification of 30.8. The DT neutron yield was 8.5×10^{12}.

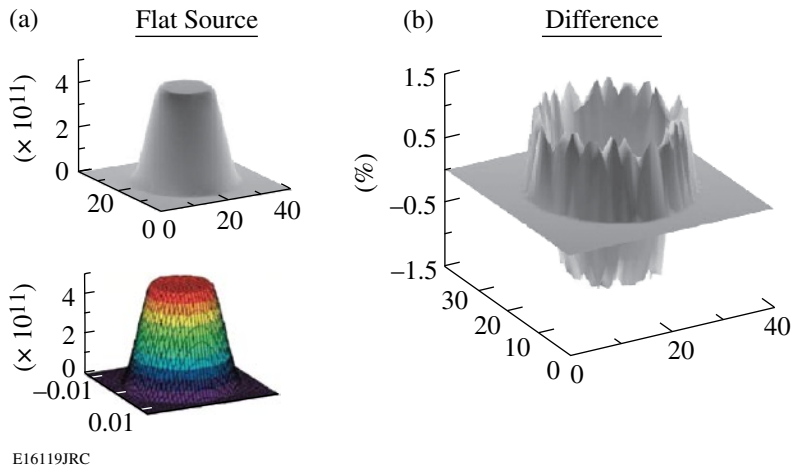

Figure 112.2
Comparison between the analytical solution and numerical simulations for a circular flat source. Graph (b) shows the relative difference between these two cases.

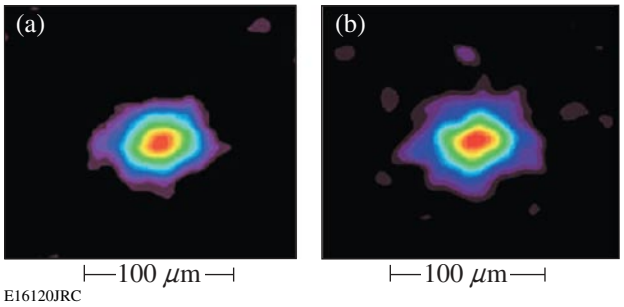

Figure 112.3
Image data (shot 35988, DT[10] CH[20], $Y_n = 8.5 \times 10^{12}$) deconvolved (a) with our code and (b) using filtered autocorrelation.[15]

Aperture Simulations

To test the sensitivity of the reconstructed images to aperture misalignment and fabrication errors, cases similar to the experimental setup described in Ref. 6 (and above) were simulated with the design code for a flat, circular source (Fig. 112.4). A biconic penumbral aperture with a central diameter of 2 mm and a pinhole with a central diameter of 10 μm were used to simulate a flat source 50 μm in diameter. In both cases, the FOV was 200 μm, the source–aperture distance was 26 cm, and the source–detector distance was 800 cm, with a magnification of 30.8. The aperture thickness was 10 cm. The maximum theoretical resolution of the simulated system for the deconvolved images was 4 μm [obtained from Eq. (2) with the assumption of a perfect alignment, and where k_c and δ_{rec} had a cumulative contribution of less than 0.1 μm]. Based on the discussion in **Reconstruction of the Detector-Plane Image** (p. 204), the tolerances for aperture fabrication and alignment can be set by the need to identify certain scale features in the reconstructed image. For this study, based on 50-μm cores on OMEGA, features of 10 μm were considered important. By incrementally moving the source relative to the system axis, an aperture misalignment was simulated. In a second phase, the aperture shape was elliptically distorted (with the eccentricity e defined in Fig. 112.4). In both cases, the error introduced in the deconvolved image was precisely defined.

1. Penumbral Apertures

The penumbral aperture's sensitivity to misalignment has been examined based on a set of simulations for apertures misaligned up to 2.36 mrad (corresponding to an offset of 250 μm relative to the primary axis). As the source is displaced, the reconstructed image appears more and more distorted (Fig. 112.5), i.e., the ratio between the horizontal and vertical dimensions increases. Image distortions within the range of the 10-μm feature limit were detectable for a misalignment angle as small as 0.4 mrad.

Aperture-fabrication defects were also analyzed for the penumbral aperture. Deviations from the circular conical shape were induced, and the coded image was transformed into an

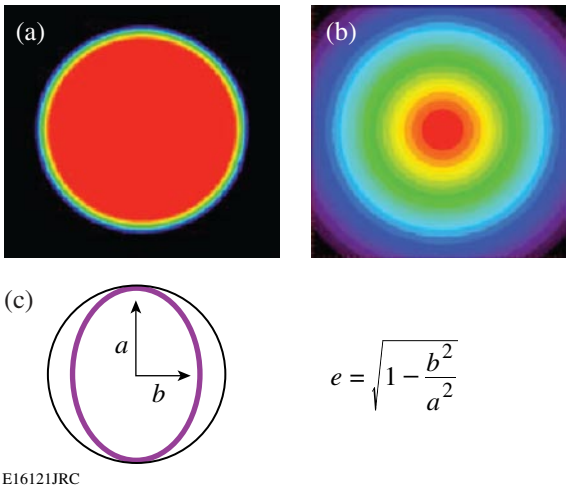

Figure 112.4
Examples of simulated raw images for a penumbral aperture (a) and a pinhole (b) seen at the detector plane level. (c) The aperture cross section and the distortion direction.

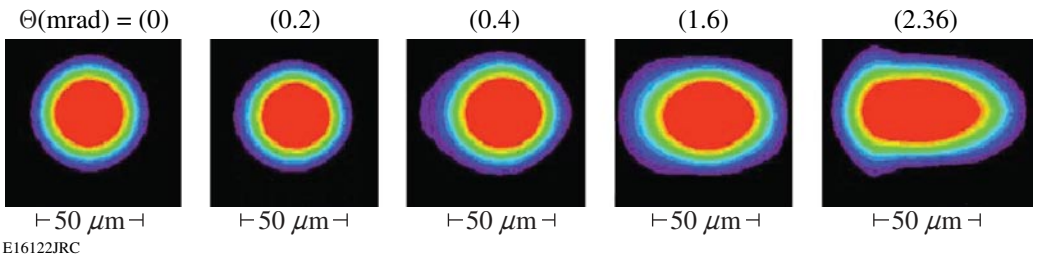

Figure 112.5
Reconstructed images of a penumbral aperture for various angles of misalignment (mrad) simulated by a source displacement.

ellipse. As the ellipse eccentricity (e) increased, the images became more and more distorted, as shown in Fig. 112.6. The subsequent modifications suggested that the aperture defects are as important as alignment for a penumbral imaging system (Fig. 112.6) and were detectable within the feature limit at an eccentricity of 0.15 or a 1.2% difference between the a and b axis parameters (this corresponds to a 24-μm out-of-round error for a 2-mm-diam aperture).

2. Pinhole Apertures

The pinhole sensitivity to misalignment has also been determined based on a set of simulations with progressively misaligned sources, in a geometry identical to the previous case. The same method has been used, first to verify the alignment tolerances (Fig. 112.7) and then to examine the influences of the fabrication defects (Fig. 112.8).

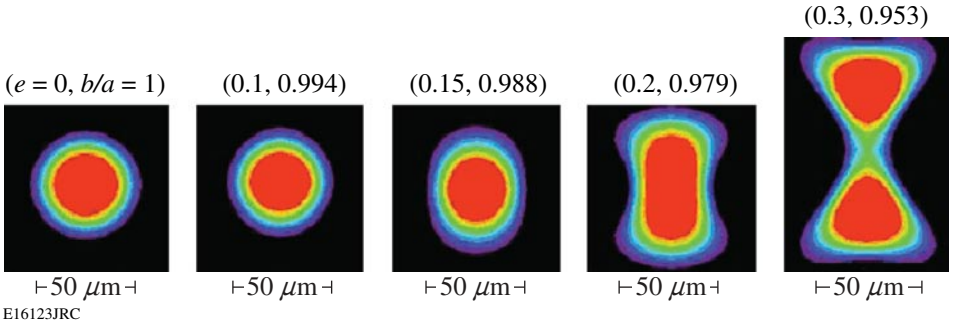

Figure 112.6
Reconstructed images of a penumbral aperture for various degrees of deformation.

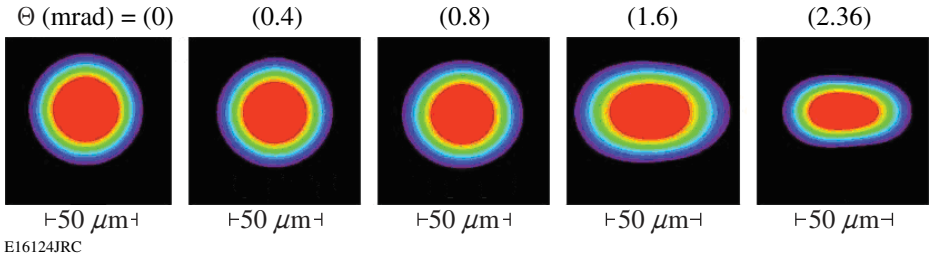

Figure 112.7
Reconstructed images of a pinhole for various angles of misalignment (mrad).

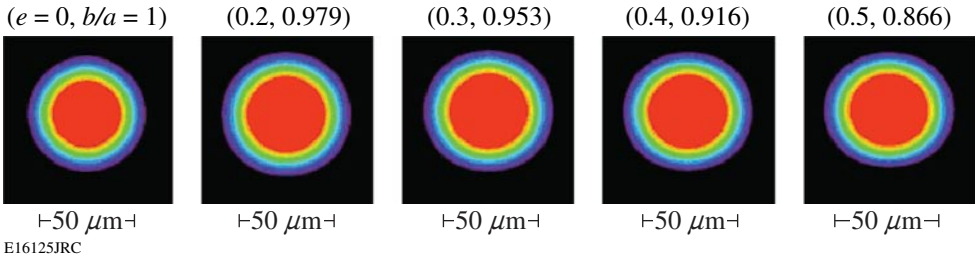

Figure 112.8
Reconstructed images of a pinhole for various degrees of deformation.

Aperture-fabrication defects were further analyzed for the pinhole. Deviations from the circular conical shape were induced and the coded image was transformed into an ellipse. As the ellipse eccentricity (e) increased, the images became more and more distorted, as shown in Fig. 112.8. Detectable distortions were observed at 0.8 mrad for the misalignment and for an eccentricity of 0.5 for the fabrication errors (a b/a ratio of 0.87 or an out-of-round tolerance of 1.4 μm for a 10-μm pinhole).

For both penumbral and pinhole apertures, the misalignment and fabrication errors can induce measurable false features in the deconvolution process. To minimize these features, alignment and fabrication tolerances can be determined from simulations such as those described above. For the imaging system previously described (and typical for a facility such as OMEGA), the requirements for a NI system designed to observe 10-μm features are summarized in Table 112.I. One can see that penumbral apertures are more sensitive to misalignment, while pinholes are more sensitive to fabrication errors.

Quantitative Analysis for the Errors Induced by Apertures

The distortions induced by the aperture-fabrication error or misalignment can be estimated by measuring the ratio between the reconstructed image axes for a flat disk neutron source. The values for angular misalignments and aperture deformations are detailed in Table 112.II.

The errors in the reconstructed image tend to increase approximately linearly with the alignment or deformation of the aperture (penumbral or pinhole).

Requirements for NI at the National Ignition Facility (NIF)

The NIF facility will use 192 laser beams for ICF with a total power of 1.8 MJ. A directly driven deuterium–tritium shell will have a diameter of 3 mm with a final compressed hot spot of about 80 μm. The geometric and energy constraints will not allow the NI imaging aperture to be placed closer than 50 cm from the source, implying, for a magnification similar to OMEGA, a much longer source–detector distance.

Simulations for penumbral and pinhole apertures similar to those used on OMEGA have been performed for the NIF case. The source–aperture distance was set to 52 cm and the source–detector distance was set to 16 m with a magnification value of M = 30.8, similar to the OMEGA simulation previously described. The FOV was maintained at the same value of 150 μm (with the apertures rescaled for the new geometry). The theoretical calculated resolution of the system was also 4 μm (calculated in the same way as for the OMEGA simulation from the previous section). The NIF requirements for a NI system can be summarized in Table 112.I.

Based on Table 112.I and the large source–aperture distance at the NIF, the limits obtained with the design tool suggest that penumbral apertures are slightly more sensitive to fabrication

Table 112.I: Tolerances for a NI system with a 10-μm resolution for the geometric configuration of OMEGA (upper) and the NIF (lower).

Penumbral Apertures (OMEGA)	Pinhole Apertures (OMEGA)
Misalignment of 0.4 mrad or source position off-center by 100 μm	Misalignment of 0.8 mrad or source position off-center by 200 μm
Fabrication eccentricity of 0.15 (i.e., 1.2% difference between the ellipse axes) or an absolute fabrication error of 24 μm	Fabrication eccentricity of 0.5 (i.e., ~14% difference between the ellipse axes) or an absolute fabrication error of 1.4 μm

Penumbral Apertures (NIF)	Pinhole Apertures (NIF)
Misalignment of 0.4 mrad	Misalignment of 0.4 mrad
Source position off-center by 200 μm	Source position off-center by 200 μm
Fabrication eccentricity of 0.15 (i.e., 1.1% difference between the ellipse axes) or an absolute fabrication error of 22 μm	Fabrication eccentricity of 0.4 (i.e., 8.3% difference between the ellipse axes) or an absolute fabrication error of 0.83 μm

Table 112.II: Angular misalignment versus axial deformation (upper). Deformation versus axial deformation (lower) of the reconstructed image for penumbral apertures and pinholes.

Angular Misalignment (mrad)	*b/a* (penumbral aperture)	Angular Misalignment (mrad)	*b/a* (pinhole)
0	1	0	1
0.2	1.007	0.2	1.045
0.4	1.195	0.4	1.13
1.6	1.375	1.6	1.53
2.36	1.785	2.36	1.79

Deformation (Eccentricity) for a Penumbral Aperture	*b/a* (penumbral)	Deformation (Eccentricity) for a Pinhole	*b/a* (pinhole)
1	1	1	1
1.006	1.025	1.021	1.055
1.012	1.2025	1.049	1.056
1.021	1.8875	1.092	1.098
1.049	5.428	1.154	1.16

errors (from 24 μm to 10 μm) with the angular sensitivity about the same, while pinholes become twice as sensitive to alignment (from 0.8 mrad to 0.4 mrad), with the same sensitivity to the relative fabrication error (1.4 μm).

Conclusions

A neutron-imaging (NI) design tool has been used to quantify the effects of aperture fabrication and alignment on reconstructed images. The simulations indicate that alignment tolerances of less than 1 mrad (current precision on OMEGA[8]) introduce measurable features in a reconstructed neutron image. Penumbral apertures are several times less sensitive to fabrication errors than pinhole apertures (as displayed in Tables 112.I and 112.II). A forthcoming publication will describe a NI bubble chamber that is being developed for high-resolution neutron imaging.

ACKNOWLEDGMENT

This work was supported by the U.S. Department of Energy Office of Inertial Confinement Fusion under Cooperative Agreement No. DE-FC52-92SF19460, the University of Rochester, and the New York State Energy Research and Development Authority. The support of DOE does not constitute an endorsement by DOE of the views expressed in this article.

REFERENCES

1. T. C. Sangster, R. L. McCrory, V. N. Goncharov, D. R. Harding, S. J. Loucks, P. W. McKenty, D. D. Meyerhofer, S. Skupsky, B. Yaakobi, B. J. MacGowan, L. J. Atherton, B. A. Hammel, J. D. Lindl, E. I. Moses, J. L. Porter, M. E. Cuneo, M. K. Matzen, C. W. Barnes, J. C. Fernandez, D. C. Wilson, J. D. Kilkenny, T. P. Bernat, A. Nikroo, B. G. Logan, S. Yu, R. D. Petrasso, J. D. Sethian and S. Obenschain, Nucl. Fusion **47** S686–S695 (2007).

2. J. D. Lindl, Phys. Plasmas **2**, 3933 (1995).

3. J. D. Kilkenny, M. D. Cable, C. A. Clower, B. A. Hammer, V. P. Karpenko, R. L. Kauffman, H. N. Kornblum, B. J. MacGowan, W. Olson, T. J. Orzechowski, D. W. Phillion, G. L. Tietbohl, J. E. Trebes, B. Chrien, B. Failor, A. Hauer, R. Hockaday, J. Oertel, R. Watt, C. Ruiz, G. Cooper, D. Hebron, L. Leeper, J. Porter, and J. Knauer, Rev. Sci. Instrum. **66**, 288 (1995).

4. R. J. Leeper, G. A. Chandler, G. W. Cooper, M. S. Derzon, D. L. Fehl, D. L. Hebron, A. R. Moats, D. D. Noack, J. L. Porter, L. E. Ruggles, J. A. Torres, M. D. Cable, P. M. Bell, C. A. Clower, B. A. Hammel, D. H. Kalantar, V. P. Karpenko, R. L. Kauffman, J. D. Kilkenny, F. D. Lee, R. A. Lerche, B. J. MacGowan, M. J. Moran, M. B. Nelson, W. Olson, T. J. Orzechowski, T. W. Phillips, D. Ress, G. L. Tietbohl, J. E. Trebes, R. J. Bartlett, R. Berggren, S. E. Caldwell, R. E. Chrien, B. H. Failor, J. C. Fernández, A. Hauer, G. Idzorek, R. G. Hockaday, T. J. Murphy, J. Oertel, R. Watt, M. Wilke, D. K. Bradley, J. Knauer, R. D. Petrasso, and C. K. Li, Rev. Sci. Instrum. **68**, 868 (1997).

5. T. J. Murphy, C. W. Barnes, R. R. Berggren, P. Bradley, S. E. Caldwell, R. E. Chrien, J. R. Faulkner, P. L. Gobby, N. M. Hoffman, J. L. Jimerson, K. A. Klare, C. L. Lee, J. M. Mack, G. L. Morgan, J. A. Oertel, F. J. Swenson, P. J. Walsh, R. B. Walton, R. G. Watt, M. D. Wilke, D. C. Wilson, C. S. Young, S. W. Haan, R. A. Lerche, M. J. Moran, T. W. Phillips, T. C. Sangster, R. J. Leeper, C. L. Ruiz, G. W. Cooper, L. Disdier, A. Rouyer, A. Fedotoff, V. Yu. Glebov, D. D. Meyerhofer, J. M. Soures, C. Stoeckl, J. A. Frenje, D. G. Hicks, C. K. Li, R. D. Petrasso, F. H. Séguin, K. Fletcher, S. Padalino, and R. K. Fisher, Rev. Sci. Instrum. **72**, 773 (2001).

6. D. Ress *et al*., Science **241**, 956 (1988).

7. T. R. Boehly, R. S. Craxton, T. H. Hinterman, J. H. Kelly, T. J. Kessler, S. A. Kumpan, S. A. Letzring, R. L. McCrory, S. F. B. Morse, W. Seka, S. Skupsky, J. M. Soures, and C. P. Verdon, Rev. Sci. Instrum. **66**, 508 (1995).

8. L. Disdier, A. Rouyer, I. Lantuéjoul, O. Landoas, J. L. Bourgade, T. C. Sangster, V. Yu. Glebov, and R. A. Lerche, Phys. Plasmas **13**, 056317 (2006).

9. R. K. Fisher, R. B. Stephens, L. Disdier, J. L. Bourgade, A. Rouyer, P. A. Jaanimagi, T. C. Sangster, R. A. Lerche, and N. Izumi, Phys. Plasmas **9**, 2182 (2002).

10. W. J. Hogan, E. I. Moses, B. E. Warner, M. S. Sorem, and J. M. Soures, Nucl. Fusion **41**, 567 (2001).

11. G. L. Morgan *et al*., Rev. Sci. Instrum. **72**, 865 (2001).

12. R. K. Fisher *et al*., Rev. Sci. Instrum. **72**, 796 (2001).

13. G. F. Knoll, *Radiation Detection and Measurement*, 3rd ed. (Wiley, New York, 2000).

14. L. Disdier, A. Rouyer, D. C. Wilson, A. Fedotoff, C. Stoeckl, J. L. Bourgade, V. Yu. Glebov, J.-P. Garçonnet, and W. Seka, Nucl. Instrum. Methods Phys. Res. A **489**, 496 (2002).

15. A. Rouyer, Rev. Sci. Instrum. **74**, 1234 (2003).

Hohlraum Energetics and Implosion Symmetry with Elliptical Phase Plates Using a Multicone Beam Geometry on OMEGA

Introduction

The overall coupling efficiency of laser energy to the implosion capsule is an important parameter for inertial confinement fusion (ICF). Indirect-drive-ignition designs planned for the National Ignition Facility (NIF) have predicted coupling efficiencies of about 10% (Ref. 1). The use of phase plates for indirect-drive implosions affects the laser-scattering losses and is a central focus of this article. Laser-beam smoothing with phase plates was shown to reduce stimulated Brillouin scattering (SBS) and stimulated Raman scattering (SRS) of gas-filled hohlraums and to increase the peak radiation temperature on Nova.[2] Phase plates reduce laser–plasma instabilities by controlling the on-target laser-intensity distribution and the speckle modal power spectrum. These experiments extend the previous work[2] to a multicone beam geometry using 40 beams compared with 10 beams configured in a single cone. An experimental platform on the OMEGA Laser System[3] for the National Ignition Campaign drives hohlraums with three cones of beams smoothed with elliptical phase plates. The 60 beams of OMEGA are symmetrically arranged around the spherical target chamber, so only 40 beams can be used to drive a hohlraum: The cones have angles of incidence 21.4° (cone 1 with 5 beams), 42.0° (cone 2 with 5 beams), and 58.8° (cone 3 with 10 beams) to the hohlraum axis. A multicone beam geometry improves the x-ray-drive symmetry of indirect-drive implosions and will be used on the NIF.[1] The new phase plates were designed to provide favorable coupling of laser energy to x-ray drive for a wide variety of indirect-drive experiments on OMEGA. The coupling of laser energy to x-ray drive for gas-filled hohlraums was significantly improved when phase plates were added. The improved coupling correlates with reduced, cone-dependent losses from SRS and SBS. A high-Z dopant in the gas-filled hohlraum[4] is shown to reduce hard x-ray production and SRS and increase the peak radiation temperature. Indirect-drive implosion symmetry[5] of vacuum and gas-filled hohlraums was investigated for the first time with a multicone laser drive smoothed with phase plates. A shift in symmetry was observed between vacuum and gas-filled hohlraums having identical beam pointing.

Elliptical Phase Plates

The elliptical phase plates can be used to drive hohlraums on OMEGA that have a laser entrance hole (LEH) diameter greater than 800 μm. Elliptical phase plates maximize the beam clearance, while minimizing the peak intensity at the LEH. This is illustrated in the upper row of Fig. 112.9, where the black circle represents the LEH having an 800-μm diameter and the gray spot indicates the size of the beam including the intensity contour, which is 1% of the peak intensity. Each column represents a beam incident on the LEH with the minor axis of the ellipse lying in the plane of incidence for each of the cones. The elliptical laser spot at normal incidence projects to a circular spot at the plane of the LEH when the angle of incidence is 42°. As seen in the upper row of Fig. 112.9, ideal clearance between the edge of the beam and the extent of the LEH is achieved for the cone-2 beam with the elliptical phase plate. The cone-1 and cone-3 beams are slightly elliptical in the plane of the LEH; however, they still have good beam clearance. A single ellipticity was chosen to streamline configuration operations on OMEGA. In contrast to the elliptical far-field laser spot, the lower row of Fig. 112.9 illustrates the limitation of the circular laser spot. To prevent the high-angle, cone-3 beams from clipping the LEH wall, the diameter of the circular laser spot must be reduced to the white circle in Fig. 112.9, which increases the peak intensity of the beam at the LEH. The phase plate is designed to produce an elliptical far field at normal incidence with a super-Gaussian power $n = 5$, a 1/e half-width minor radius $\delta_{\min} = 103$ μm, and 1/e half-width major radius $\delta_{\mathrm{maj}} = 146$ μm. The single-beam average (I_{50}) and peak (I_{95}) intensities generated with the phase plate and a 500-J, 1-ns square laser pulse are designed to be $I_{50} = 1.3 \times 10^{15}$ W/cm^2 and $I_{95} = 4.5 \times 10^{15}$ W/cm^2, respectively. The far-field intensity distribution produced with the phase plate was characterized on OMEGA using the ultraviolet equivalent-target-plane diagnostic.[6] The portion of the measured envelope having intensities greater than 10% of the peak intensity was modeled with a super-Gaussian profile having $n = 4.1$, $\delta_{\min} = 106$ μm, and $\delta_{\mathrm{maj}} = 145$ μm. Analysis of the single-beam intensity shows the E-IDI-300 phase plate generates an average intensity of $I_{50} =$

1.0×10^{15} and a peak intensity of $I_{95} = 3.8 \times 10^{15}$ W/cm^2 with a 500-J, 1-ns square laser pulse drive. Similar measurements performed for 9 of the 43 phase plates were found to be close to the design specifications with $I_{50} = 1.0 \pm 0.05 \times 10^{15}$ W/cm^2, $I_{95} = 3.7 \pm 0.2 \times 10^{15}$ W/cm^2, $n = 4.3 \pm 0.3$, $\delta_{\min} = 106 \pm 1.4$ μm, and $\delta_{\text{maj}} = 144 \pm 2.7$ μm.

Hohlraum Energetics and Indirect-Drive-Implosion Symmetry Experiments

Hohlraum energetics experiments were conducted using thin-walled (5 μm Au), scale-1, vacuum and gas-filled (0.9 atm C_5H_{12}) Au halfraums irradiated with the shaped laser pulse PS26. The halfraums have an equal length and diameter of 1.6 mm and an LEH diameter of 1.07 mm. The fully ionized n_e of the hohlraum plasma for the gas-filled targets is 9×10^{20} cm^{-3}. The gas fill is contained with a 0.6-μm-thick polyimide window over the LEH. Time-resolved, absolute levels of the x-ray flux were recorded with the Dante diagnostic.[7] Time-integrated levels of SRS and SBS that scattered back through the OMEGA focus lens were recorded with the full-aperture backscatter station (FABS), and light scattered just outside the lens was recorded with the near-backscatter imaging (NBI) diagnostic.[8] The coupling of laser energy to x-ray drive is significantly improved for gas-filled halfraums with phase plates, consistent with earlier work.[2] The targets were irradiated with an ~7-kJ PS26 laser pulse using 20 beams. As shown in Fig. 112.10(a), the peak radiation temperature T_r inferred from the measured levels of the x-ray flux increased by 17 eV when the laser beams were smoothed with phase plates, corresponding to a 44% increase in the peak x-ray flux. The improved coupling is correlated with reduced laser-scattering losses. A shot-by-shot scan was performed to measure the cone-dependent laser-scattering losses. It was assumed that the laser-scattering losses were caused by single-beam interactions; consequently, all of the heater beams had phase plates. Shots were taken with and without phase plates in the interaction beam to complete the shot matrix. As shown in Figs. 112.10(b) and 112.10(c), laser-beam smoothing with phase plates reduces the cone-dependent FABS SRS and FABS SBS signals. The most energetically significant reductions occur for FABS SRS in cone 1 (23% to 10%) and cone 2 (17% to 4%). The total FABS scattering levels are higher for SRS than SBS (11% versus 5% without phase plates and 4% versus 2% with phase plates). The NBI SBS signal was 2% without phase plates and was negligible with phase plates. NBI SRS signals are not available. The scattering losses measured with FABS SRS, FABS SBS, and NBI SBS were reduced by nearly a factor of 3 with phase plates (18% without phase plates and 6% with phase plates).

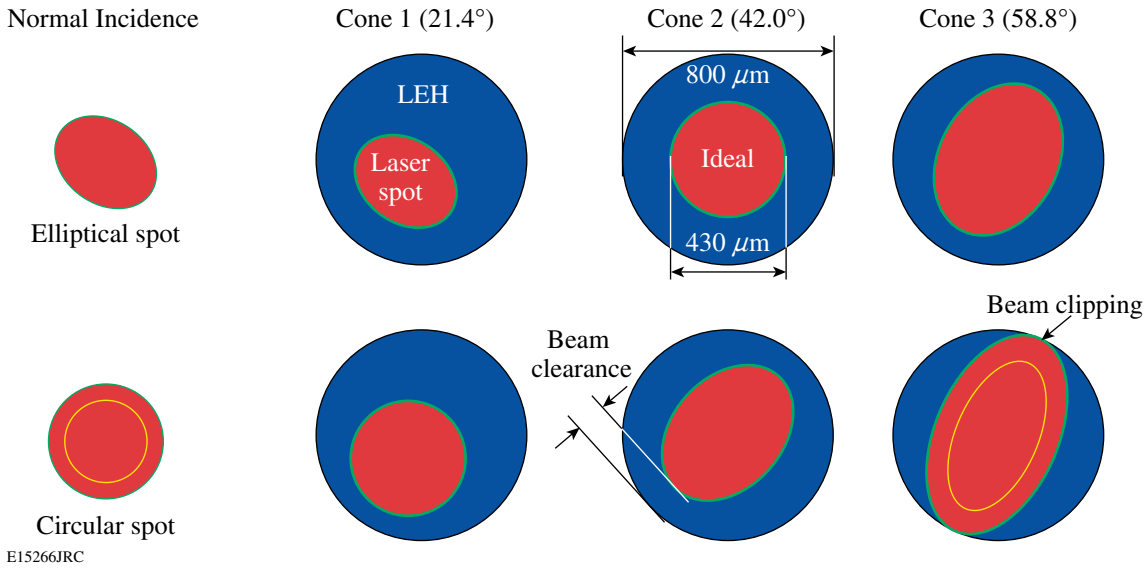

Figure 112.9
Beam clearance for each of the three cones for an elliptical beam (upper trace) and a circular beam (lower trace). The black circle represents the LEH having an 800-μm diameter; the gray spot indicates the size of the beam including the intensity contour, which is 1% of the peak intensity. The circular spot needs to be reduced to the white circle to prevent beam clipping on the LEH wall.

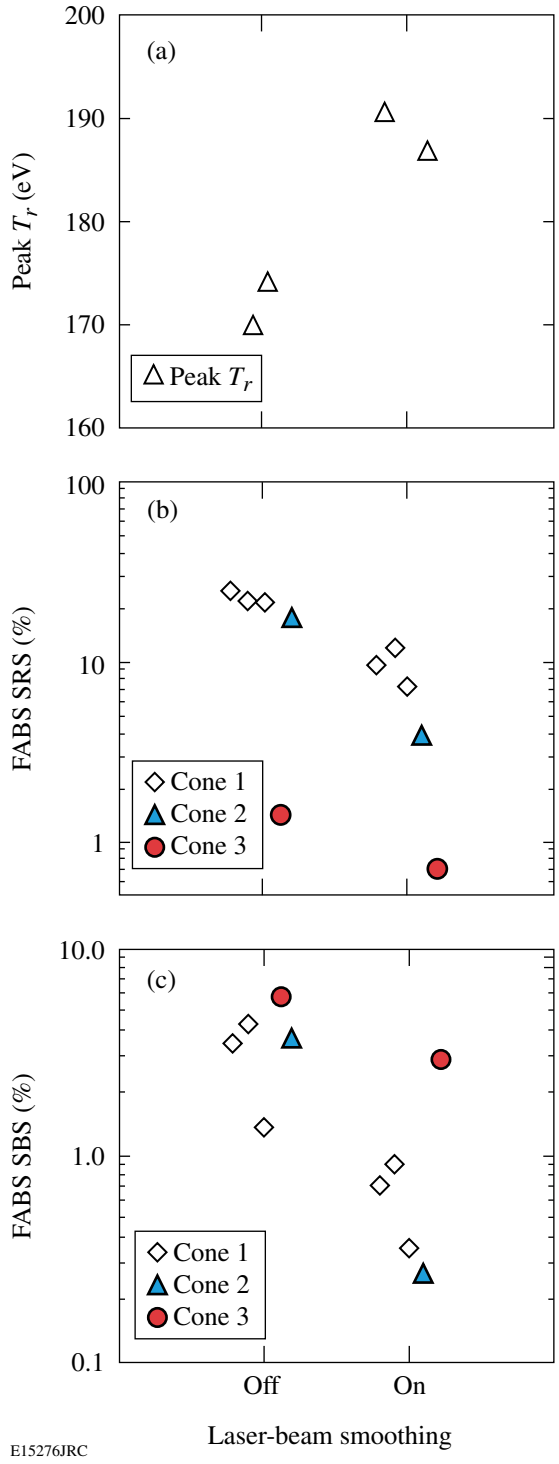

Figure 112.10
(a) The peak T_r with and without laser-beam smoothing with phase plates for gas-filled halfraums. Percent of incident beam energy detected by (b) FABS SRS and (c) FABS SBS for each beam cone.

The symmetry of imploding gas-filled (D_2 doped with Ar) plastic capsules driven with gas-filled, scale-1, Au hohlraums having lengths of 2.3 and 2.5 mm was measured on OMEGA using phase plates in the drive beams. Axial and radial gated-x-ray images of the implosion around the time of peak compression were recorded. Figure 112.11 shows that a shift of 150 μm in symmetry was observed between vacuum and gas-filled (0.9 atm CH_4) hohlraums having identical beam pointing. The fully ionized n_e of the hohlraum plasma for the gas-filled targets is 2.2×10^{20} cm^{-3}. The ratio of x-ray drive at the poles of the capsule relative to the waist increased for the gas-filled hohlraum. As shown in Fig. 112.10, the inner cone beams (cone 1) have the highest level of SRS. The differential laser-scattering levels between the cones, which is more pronounced for the gas-filled hohlraum, could affect the indirect-drive-implosion symmetry and is the most likely cause for the observed symmetry shift seen in Fig. 112.11.

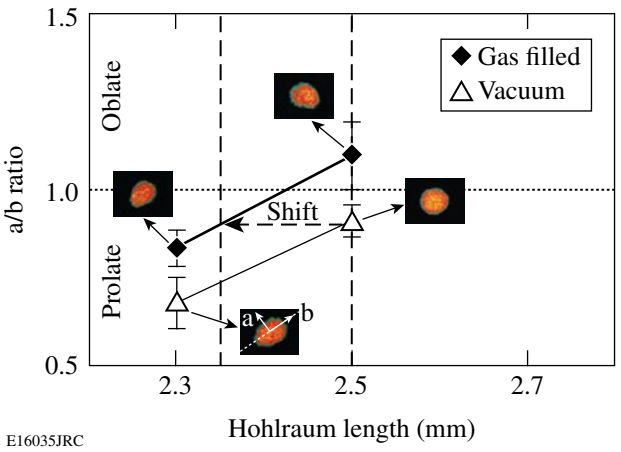

Figure 112.11
Symmetry of indirect-drive implosion quantified from gated-x-ray images ($h\nu > 3$ keV) of implosions taken along a radial view [hohlraum radial and axial directions are (a) and (b), respectively]. A 150-μm symmetry shift was observed between vacuum and gas-filled hohlraums having identical beam pointing.

In conclusion, elliptical phase plates are benefiting indirect-drive experiments on OMEGA.

ACKNOWLEDGMENT

This work was supported by the U.S. Department of Energy Office of Inertial Confinement Fusion under Cooperative Agreement No. DE-FC52-92SF19460, the University of Rochester, and the New York State Energy Research and Development Authority. The support of DOE does not constitute an endorsement by DOE of the views expressed in this article.

REFERENCES

1. J. D. Lindl *et al*., Phys. Plasmas **11**, 339 (2004).
2. S. H. Glenzer *et al*., Phys. Rev. Lett. **80**, 2845 (1998).
3. T. R. Boehly, D. L. Brown, R. S. Craxton, R. L. Keck, J. P. Knauer, J. H. Kelly, T. J. Kessler, S. A. Kumpan, S. J. Loucks, S. A. Letzring, F. J. Marshall, R. L. McCrory, S. F. B. Morse, W. Seka, J. M. Soures, and C. P. Verdon, Opt. Commun. **133**, 495 (1997).
4. R. M. Stevenson *et al*., Phys. Plasmas **11**, 2709 (2004).
5. N. D. Delamater *et al*., Phys. Plasmas **7**, 1609 (2000).
6. S. P. Regan, J. A. Marozas, J. H. Kelly, T. R. Boehly, W. R. Donaldson, P. A. Jaanimagi, R. L. Keck, T. J. Kessler, D. D. Meyerhofer, W. Seka, S. Skupsky, and V. A. Smalyuk, J. Opt. Soc. Am. B **17**, 1483 (2000).
7. C. Sorce *et al*., Rev. Sci. Instrum. **77**, 10E518 (2006).
8. S. P. Regan, D. K. Bradley, A. V. Chirokikh, R. S. Craxton, D. D. Meyerhofer, W. Seka, R. W. Short, A. Simon, R. P. J. Town, B. Yaakobi, J. J. Carroll III, and R. P. Drake, Phys. Plasmas **6**, 2072 (1999).

Improved Measurement of Preheat in Cryogenic Targets

Introduction

Preheat by fast electrons in cryogenic target implosions is thought to be a crucial parameter in determining target performance, primarily the achieved areal density. To quantitatively relate the achieved areal density to the fuel preheat, the preheat measurement has to be sufficiently reliable and precise. In addition, the validity of the assumptions used in the data analysis and the resulting uncertainty have to be determined. To that end this article presents a reformulated and more consistent analysis of preheat measurements and discusses the sensitivity of the results to the assumptions made in the analysis. The results are applied to both cryogenic and CH targets.

Details of the method of analysis are described in Ref. 1. The preheat is determined from the hard x-ray (HXR) bremsstrahlung radiation; the HXR detector is calibrated by using a CH-coated molybdenum (Mo) solid sphere where the preheat is determined using the Mo K_α line. The resulting calculated curves for both cryogenic and CH targets directly relate the HXR signal to the preheat. The curves are plotted as a function of fast-electron temperature, which is also measured by the HXR detectors.

The main improvement with respect to previous results[1] is the folding of the HXR sensitivity curve[2] into the calculation of emitted radiation. The total bremsstrahlung radiation for a given electron energy is taken from the NIST tables,[3] but the folding also requires the spectrum of the radiation. That spectrum is a function of the photon energy E_p and the electron energy E_e ($E_p < E_e$); the spectrum is usually plotted as a function of $R = E_p/E_e$ but still depends separately on E_e. The folding with detector sensitivity has to be done for each electron energy. Also, because the electron-energy distribution changes due to the transport through the target, the folding is done at each target location. The bremsstrahlung spectra were tabulated in papers by Seltzer *et al.*[4] and Pratt *et al.*,[5] on which the NIST tables are based. *Thus, the calibration of the HXR detector is not a stand-alone number but is intertwined with the radiation spectrum and thus with the electron-energy distribution*. The detector measures only the absorbed radiation, and the derivation of incident radiation is model dependent. The radiation spectrum is calculated from the electron-energy distribution but the latter has to be assumed.

A simplified, generic formulation of bremsstrahlung radiation given by Jackson[6] is often used. Figure 112.12 compares the total radiation emitted by an electron traveling in Mo, calculated using Eq. (15.30) in Ref. 6 and as given by the NIST tables. Jackson's formula is insufficient for precise calculations of preheat.

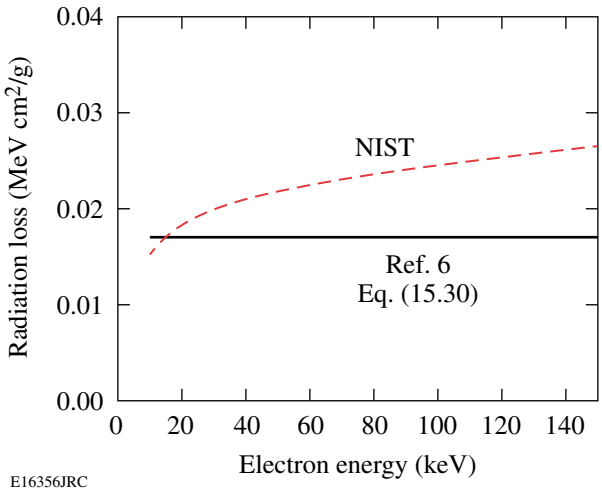

Figure 112.12
Comparison of the total radiation emitted by an electron traveling in Mo, as a function of its energy. The upper curve is given by the NIST tables;[3] the lower curve is calculated by Jackson [Eq. (15.30) in Ref. 6]. Jackson's formula is insufficient for precise calculations of preheat.

Effective Detector Sensitivity

The folding of detector sensitivity described here was done for the three cases of Mo, CH, and cryogenic D_2 (or DT) targets. The relative sensitivity of the HXR detector $S(E_p)$ as a function of photon energy is given in Ref. 2. $S(E_p)$ is the fraction of radiation absorbed in the detector. The fraction of the radiation energy emitted by an electron of energy E_e that is absorbed by the detector is given by

$$S_{\text{eff}}(E_e) = \frac{\int \text{bremss}(E_e, E_p) S(E_p) \mathrm{d}E_p}{\int \text{bremss}(E_e, E_p) \mathrm{d}E_p}, \quad (1)$$

where "bremss" is the bremsstrahlung spectrum (from Refs. 4 and 5). Figure 112.13 shows the calculated S_{eff} for a few materials. As seen, the effective sensitivity depends weakly on the material. The total energy radiated by an electron of energy E_e that is absorbed in the detector is given by

$$E_{\text{abs}}(E_e) = S_{\text{eff}}(E_e) \times \text{NIST}_{\text{bremss}}(E_e), \quad (2)$$

where $\text{NIST}_{\text{bremss}}$ is the total radiation emitted by an electron of energy E_e, per cm traveled, and is given by the NIST tables.[3] In the transport calculations described below, the results of Eq. (2), using curves like those in Fig. 112.13, are summed over the electron-energy distribution $D(E_e)$ at each target location. Summing over the target volume yields the total radiation energy absorbed in the detector for a given energy in the fast electrons. The calibration described below relates the energy absorbed in the detector to the detector reading (in pC). The initial distribution $D(E_e)$ is guessed and is then modified by the transport through the target. Three initial shapes for $D(E_e)$ were tested:

$$\begin{aligned} &\text{(a) exponential:} && D(E_e) = \exp(-E_e/T_e) \\ &\text{(b) Maxwellian:} && D(E_e) = E_e^{1/2} \exp(-E_e/T_e) \\ &\text{(c) truncated:} && D(E_e) = \begin{cases} \exp(-E_e/T_e) \\ 0 \text{ for } E_e > 3T_e \end{cases} \end{aligned} \quad (3)$$

Distributions (b) and (c) can be thought of as two extremes of (a): in (b) the low-energy part of $D(E_e)$ is reduced, whereas in (c) the high-energy part of $D(E_e)$ is reduced. Since low-energy electrons are more efficient in collisions whereas high-energy electrons are more efficient in radiation, the ratio of preheat to radiation, as expected, is found to increase in going from (b) to (a) to (c).

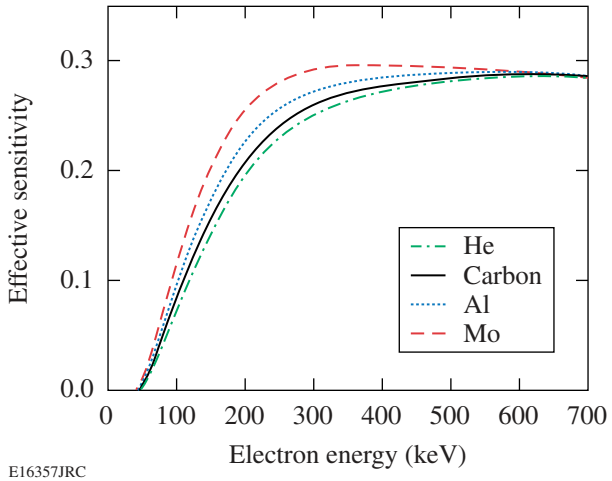

Figure 112.13
Effective sensitivity: the fraction of the radiation emitted by an electron of energy E_e that is absorbed in the detector (HXR2), using Eq. (1). These curves, summed over the assumed electron-energy distribution (for the known temperature), relate the radiation energy absorbed in the detector to the energy in fast electrons.

The Mo Target Calibration Experiment

The preheat energy in any target experiment is determined from the HXR signal. To calibrate the HXR detector in absolute units, we used an ~0.9-mm-diam molybdenum solid sphere, coated with a 20-μm-thick CH layer. The target was irradiated with the 60 OMEGA beams at an intensity of ~1×10^{15} W/cm^2 and a 1-ns square pulse.[1] The preheat was determined from the Mo K_α line and related to the HXR signal. The measured Mo K_α energy was 9.4 mJ (per total solid angle). The HXR2 channel (used to determine the total radiation) measured a signal of 1200 pC, and comparison of channels 2, 3, and 4 yielded a fast-electron temperature of T_e = 65 keV.

A 1-D multi-energy transport code was used to transport fast electrons of varying temperatures for each of the three chosen shapes [Eq. (3)]. The calculations using a stationary target are time integrated over the pulse, as are the measurements of K_α and HXR energies. In a 1-D calculation, only radial trajectories are considered. For the Mo target this is justified because *LILAC* simulations show that at the end of the pulse the quarter-critical density is ~100 μm away from the target surface, a distance much smaller than the target diameter. At the end of the pulse (when most of the fast electrons are generated) the thickness of the unablated CH layer is ~10 μm. Therefore, in the calculations we assumed a cold, 10-μm-thick CH layer. When the calculations were repeated for a 15-μm CH thickness, the resulting calibration was hardly changed. The transport code calculates the slowing down of electrons, the production and transport of K_α energy, and the production of HXR continuum. For the slowing down and the HXR production, the NIST tables are used; for the K_α production a semi-empirical cross section[7] is used. The transport code shows that more than 99% of the HXR comes from the Mo; however, some of the electron energy (~10%) is deposited in the CH and must be subtracted from the total deposited energy. Two ratios are computed: PH/K_α = (preheat energy)/(K_α energy) and

PH/HXR-abs = (preheat energy)/(energy absorbed in HXR2), both as a function of T_e. The K_α energy refers to the energy exiting the target after absorption within the molybdenum. Here, we need only the results for the case of the Mo experiment (T_e = 65 keV), which we quote in Table 112.III. The absorption of the K_α line within the target increases with electron temperature because higher-energy electrons penetrate deeper; for T_e = 65 keV that absorption is only ~30%.

Table 112.III shows the Mo target analysis results for the three electron distributions considered. Row 1 shows the ratio of preheat to emergent K_α energy. For the measured K_α energy of 9.4 mJ, row 2 shows the preheat energy within the molybdenum. Row 3 shows the ratio of preheat energy to HXR energy absorbed in the detector. Dividing row 2 by row 3 yields the total energy absorbed in the HXR2 detector. Finally, dividing the measured HXR2 signal of 1200 pC by row 4 yields detector absolute calibration, namely the signal in HXR2 (in pC) per radiation energy absorbed in HXR2 (in mJ).

As explained above, the ratio PH/HXR-abs increases in going from (b) to (a) to (c) because the relative number of low-energy electrons in the distribution increases. This is also true for the ratio PH/K_α, but here the change is very small (~6%). This can be shown to be due to the differences in the cross sections for producing K_α and bremsstrahlung radiation. The calibration factor is seen to change appreciably with the change in assumed distribution shape. However, as shown below, in calculating preheat in cryogenic or CH targets, the differences between the three distribution shapes become considerably smaller. This is because the ratio PH/HXR in CH or cryogenic targets is also dependent on the distribution shape, and when applying the corresponding calibration factor from Table 112.III, these differences partly cancel out.

Preheat in CH Targets

The ratio of preheat to the HXR2 signal for CH targets was calculated as a function of temperature of the fast electrons, for each of the three electron-distribution shapes of Eq. (3). As in the case of Mo, the NIST tables are used for both the slowing down (collisions) and the bremsstrahlung radiation. The corresponding calibration numbers of Table 112.III were used to convert radiation energy absorbed in the detector to the signal in pC. We assumed that the shape of the electron distribution is the same in the Mo experiment as in CH target experiments. This assumption is reasonable since in both cases (as well as in the cryogenic targets discussed below) the laser interacts with a CH layer. Thus, for each of the three distribution shapes, we used the corresponding calibration factor from Table 112.III. The results for a 10-μm-thick CH target are shown in Fig. 112.14. The variation around the average for all temperatures is ±25%. This represents the range of uncertainties in the preheat determination. To illustrate how the results depend on the target thickness, we show in Fig. 112.15 the ratio for a Maxwellian electron distribution, for three different thicknesses. The ratio of preheat to the HXR2 signal is almost independent of the target thickness. For electrons of a single

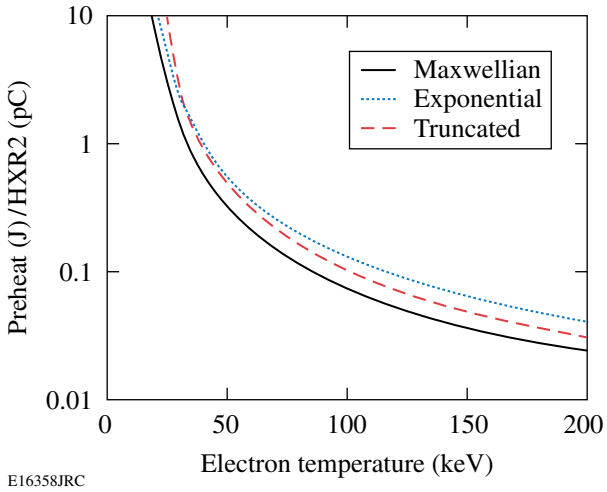

Figure 112.14
The ratio of preheat energy deposited by fast electrons in a 10-μm-thick CH target to the HXR2 reading (pC) for three assumed distributions of electron energies.

Table 112.III: Calculated quantities involved in determining the HXR detector calibration from the Mo experiment, for three electron-energy distribution shapes

	Quantity Calculated	(a) Exponential	(b) Maxwellian	(c) Truncated
1	Preheat/K_α	1058	996	1063
2	Mo preheat	9.945 J	9.36 J	10.0 J
3	Preheat/HXR-abs	1704	1355	2503
4	HXR-abs	5.83 mJ	6.9 mJ	4.0 mJ
5	Calibration (pC/mJ)	205	174	300

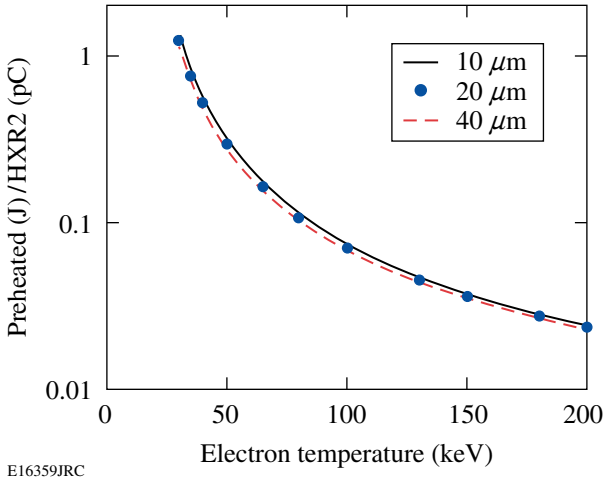

Figure 112.15
Ratio of preheat energy deposited by fast electrons in CH to HXR2 reading (pC) for three thicknesses of the CH target. A Maxwellian distribution of electron energies was assumed.

energy E_e, the ratio increases with thickness (until the thickness exceeds the range corresponding to E_e) because a thicker target yields slower electrons, for which the preheat increases (as ~1/E), whereas the radiation decreases (see Fig. 112.12). However, for the case of continuous distribution of energies, the shift of the distribution to lower energies is equivalent to lowering the distribution, which does not affect the ratio of the two plotted quantities.

Preheat in Cryogenic Targets

To calculate the preheat and x-ray emission from cryogenic targets we use again a 1-D, multi-energy transport code. However, unlike the case of the CH-coated Mo target, the fraction of radiation emitted by the CH shell is not negligible and its calculation requires a multidimensional treatment of the fast-electron transport. This is because when the fast electrons are generated, the quarter-critical surface is far enough from the target to enable many trajectories that miss the cold-fuel shell. Thus, before applying the preheat results derived here, that fraction has to be determined separately. Using the measured radiation that is emitted by the fuel leads to the determination of the preheat within the fuel alone. The deposition of electron energy within the CH shell is irrelevant to the determination of fuel preheat, but it affects the preheat results marginally since it changes the energy distribution of the electrons entering the fuel. As will be shown below, the results are weakly dependent on that distribution. For the calculation of radiation we again use the NIST tables. However, for the collisional transport (preheat) we must use the formula for slowing down in a plasma since the fuel is fully ionized even with no preheat. We use Eq. (1) of Ref. 1:

$$\left(-\mathrm{d}E/\mathrm{d}x\right) = \left(2\pi e^4 N_e/E\right) \ln\left(1.52\, E/\hbar\,\omega_p\right) \qquad (4)$$

in terms of the electron density and the plasma frequency. This equation is essentially identical to Eq. (13.88) given by Jackson in Ref. 6. We used the plasma density profile calculated by *LILAC* at the end of the laser pulse (when most of the $2\omega_p$ electrons were found to be generated); however, the results are shown to be insensitive to this choice.

For transport in un-ionized material, the dependence on electron density of the ratio preheat/radiation cancels out. However, because of the appearance of the plasma frequency in the Coulomb logarithm in Eq. (4), we must consider the density profile of a particular case. We used the plasma density profile calculated by *LILAC* for a typical D_2 cryogenic target shot at an irradiance of 5×10^{14} W/cm^2, at the end of the laser pulse. Figure 112.16 shows curves for the ratio of preheat to energy absorbed in the detector for the three distribution shapes; Fig. 112.17 shows the curves after applying the calibration from Table 112.III. The total relative span of the three curves around an average is ~20%. To test the sensitivity of the results to the density profile, Fig. 112.18 shows the effect of multiplying or dividing the density profile everywhere by a factor of 4. The preheat deduced from the HXR detector is seen to be weakly dependent on the density (or the areal density) of the fuel. Thus,

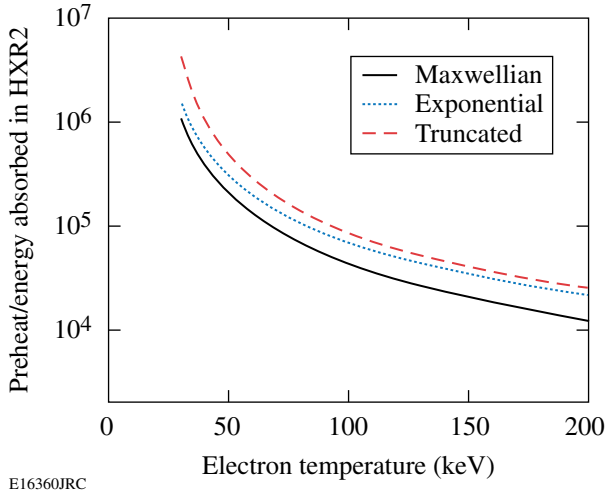

Figure 112.16
Ratio of energy deposited in D_2 by fast electrons to energy absorbed in HXR2 for three different distributions of fast-electron energies. Much of the variation between the three curves disappears when converting the absorbed x-ray energy to a detector signal (Fig. 112.17).

the validity of the preheat curves for CH (Fig. 112.14) and D_2 (Fig. 112.16) is quite general with a precision of ~25%. The uncertainty in the experimentally determined temperature adds an additional uncertainty. The curves for D_2 apply equally to a DT fuel since the loss rate dE/dx due to either collisions or radiation is independent of the atomic mass. The NIST tables are actually given in terms of $(1/\rho)$dE/dx; this is inconsequential for Mo or CH since only the ratio of the two losses is used. However, for the cryogenic targets, we use the NIST tables only for the collision rate; thus, the tables (which are for hydrogen) had to be restated in terms of dE/dx, for which case they are the same for either D_2 or DT.

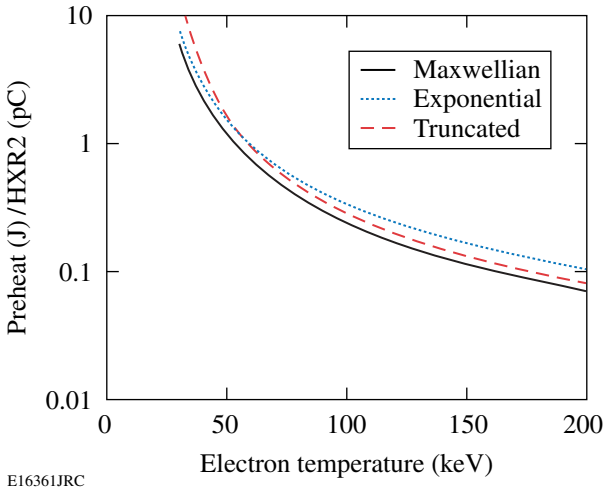

Figure 112.17
Ratio of energy deposited by fast electrons in D_2 to HXR2 reading (in pC) for three different distributions of fast-electron energies. The preheat deduced from the HXR detector is seen to be weakly dependent on the assumed electron distribution.

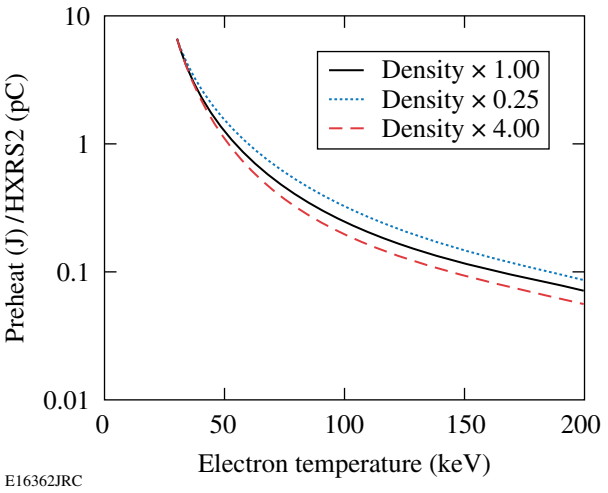

Figure 112.18
Ratio of energy deposited by fast electrons in D_2 to HXR2 reading (in pC) for a Maxwellian distribution of fast-electron energies and three different multipliers of the *LILAC*-simulated density profile. The preheat deduced from the HXR detector is seen to be weakly dependent on the density (or the areal density) of the fuel.

The *LILAC*-calculated density profile shows a sharp, well-defined cold shell of ~4-g/cm^3 density. Since the preheating of this cold shell is particularly relevant to target-performance degradation, we calculated the fraction of energy deposited within this shell, assuming the electrons move radially. For all temperatures above ~50 keV, this fraction is about constant at ~0.8 and drops at lower temperatures. This is an upper limit on the fraction of energy deposited in the cold shell, as 2-D effects will lower it. It should be noted that the HXR signal in the ordinates of Figs. 112.16 and 112.17 apply only to the x-ray emission from the fuel, not the CH. Thus, before applying these figures to a particular cryogenic experiment, the fraction of the measured x-ray signal emitted by the fuel has to be determined by a code allowing for the 2-D trajectories of the electrons. No such complication arises in the case of CH-only targets. For these targets, the measured HXR signal yields the total energy absorbed as preheat in the target (integrated over time and space), with no need for 2-D calculation of the electron trajectories. This is also shown in Fig. 112.15 by the independence of the ratio x ray/preheat on the target thickness.

An important result derived from these calculations relates to the determination of the temperature from the measured signals in three of the four HXR channels. The shape of the bremsstrahlung spectrum in these determinations[2] is customarily assumed to be exponential [~exp(–E/T)]. However, calculating the x-ray spectrum for a variety of assumed electron-energy distributions shows that the x-ray spectrum deviates from an exponential. Figure 112.19 shows the calculated bremsstrahlung spectrum for three different electron-distribution functions plotted versus photon energy normalized to the fast-electron temperature. They are obtained by averaging the spectrum from a single-electron energy[1] over the electron-energy distribution. We see that even for an assumed exponential distribution for the electrons, the distribution for the photons is not exponential, except for high E/T. The curve marked "slope" represents the exponential spectrum assumed in the derivation of the temperature from the HXR signals. Therefore, the HXR data have to be fitted with one of the curves shown in Fig. 112.19. The HXR channels are dominated by radiation in the range ~50 to 80 keV determined by the channel filters. Thus, for temperatures higher than ~80 keV, relevant values of E/T are smaller than 1 and the

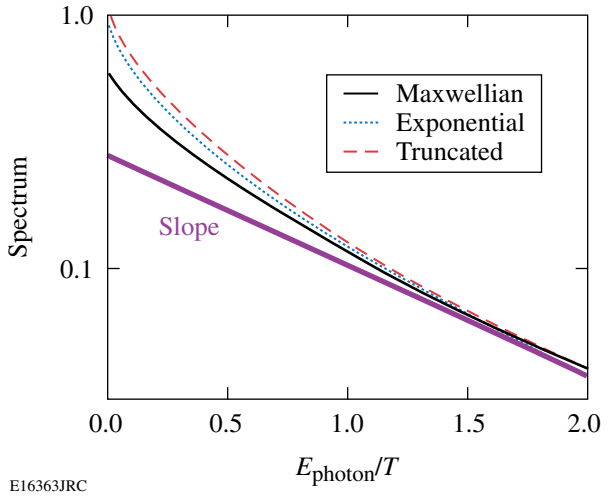

Figure 112.19
Bremsstrahlung spectrum calculated using tabulated values from Seltzer and Berger,[4] on which NIST slowing-down tables are based. The spectra for each electron energy were averaged over three different electron-distribution functions and plotted versus photon energy normalized to the fast-electron temperature.

derived temperature would be lower than the true temperature (given by the curve marked "slope"). The correction increases with temperature. For a measured value of T = 100 keV, the correct temperature is estimated to be ~130 keV. The corrected temperature would reduce the determined preheat for a given measured HXR signal. Using Fig. 112.17 we estimate that the derived preheat for fast-electron temperatures in the range of 100 to 200 keV would drop by ~50%. This indicates that even for high values of laser irradiance, the preheat by fast electrons may not be an important factor in explaining the degradation in compression.

In summary, an improved procedure for calculating preheat from the measured hard x-ray signal is described. The numerically calculated bremsstrahlung spectrum as a function of electron energy (E) is averaged over an assumed electron-energy distribution and folded with the HXR detector sensitivity. This is done for each value of E and each target location within a multi-group, 1-D electron-transport code. The results relate the measured HXR signal and fast-electron temperature to the preheat. A 2-D transport code has to be used to determine the fraction of the measured x-ray signal coming from the fuel for cryogenic experiments because of the two-material target composition. Additionally, the shape of the measured x-ray spectrum has been calculated; this shape has to be used in the fitting of the HXR channels data. This correct procedure will yield a higher fast-electron temperature than when assuming an exponential x-ray spectrum and, therefore, a lower preheat for a given HXR signal.

ACKNOWLEDGMENT

This work was supported by the U.S. Department of Energy Office of Inertial Confinement Fusion under Cooperative Agreement No. DE-FC52-92SF19460, the University of Rochester, and the New York State Energy Research and Development Authority. The support of DOE does not constitute an endorsement by DOE of the views expressed in this article.

REFERENCES

1. B. Yaakobi, C. Stoeckl, W. Seka, J. A. Delettrez, T. C. Sangster, and D. D. Meyerhofer, Phys. Plasmas **12**, 062703 (2005).

2. C. Stoeckl, V. Yu. Glebov, D. D. Meyerhofer, W. Seka, B. Yaakobi, R. P. J. Town, and J. D. Zuegel, Rev. Sci. Instrum. **72**, 1197 (2001).

3. M. J. Berger, J. S. Coursey, and M. A. Zucker, *ESTAR*, *PSTAR*, and *ASTAR*: Computer Programs for Calculating Stopping-Power and Range Tables for Electrons, Protons, and Helium Ions (version 1.2.2). [Online] Available: http://physics.nist.gov/Star [25 February 2005]. National Institute of Standards and Technology, Gaithersburg, MD.

4. S. M. Seltzer and M. J. Berger, Nucl. Instrum. Methods Phys. Res. B **12**, 95 (1985).

5. R. H. Pratt *et al*., At. Data Nucl. Data Tables **20**, 175 (1977).

6. J. D. Jackson, *Classical Electrodynamics*, 2nd ed. (Wiley, New York, 1975).

7. C. J. Powell, Rev. Mod. Phys. **48**, 33 (1976).

Laser Channeling in Millimeter-Scale Underdense Plasmas of Fast-Ignition Targets

Ignition in inertial confinement fusion (ICF) starts in a hot spot in the core of compressed fuel pellets. In conventional ICF schemes, the hot spot—a small region with a temperature of ~10 keV—is created through a highly symmetric compression driven by multiple laser beams that illuminate the target from all directions.[1] In fast ignition (FI) a separate ignition pulse is used to create the hot spot after the core has been compressed, thereby relaxing symmetry requirements and leading to higher gain.[2] There are several scenarios for getting the ignition pulse close to the compressed core. In the so-called "hole-boring" scenario of FI, the ignition pulse is to first propagate through a millimeter (mm)-scale underdense plasma to reach a critical surface with a critical density $n_c = \omega_0^2 m_e \big/ (4\pi e^2)$ (m_e and e are electron mass and charge, respectively, and ω_0 is the pulse frequency). There the ignition pulse may continue to push forward into the overdense plasma through its ponderomotive pressure (hole boring) and relativistic transparency. As the intense laser interacts with the overdense plasma, it generates energetic electrons that must eventually reach the dense core region where their energy is to be absorbed to create the hot spot. An alternative way to move the ignition pulse closer to the core region is to use fuel pellets with a hollow gold cone attached to one side. The compression beams illuminate the target from all directions except those within the opening of the cone. The asymmetric compression still leads to a dense core and has the potential to lead to a clear path for the ignition pulse to propagate up to a very overdense plasma. The first integrated FI experiments with the coned targets showed a 10^3 times fusion neutron increase.[3] However, the hole-boring scenario is still being actively pursued for its more symmetric compression and its absence of radiation loss associated with the gold cone.

Many factors affect the overall efficiency of converting the ignition pulse energy to the hot-spot energy, including the conversion efficiency to the energetic electrons at the critical surface,[4–6] the angular spread of these electrons,[7,8] and the slowing-down and scattering of the electrons as they propagate to the core.[9] Of particular concern to the hole-boring scenario is the loss of ignition pulse energy through laser–plasma interactions in the mm-scale underdense plasma.[10] While a small-amplitude electromagnetic wave can linearly propagate through densities less than n_c without much loss, the petawatt (PW) ignition pulse can interact with the plasma in a highly nonlinear manner, leading to processes such as laser self-focusing[11,12] and filamentation,[13,14] as well as scattering[15] and significant plasma heating and density modification.[14,16] Energy lost in this region will not be available for hole boring and energetic electron generation at the critical surface. A channeling pulse, which could be the prepulse of the ignition pulse or a separate pulse, has been proposed[2] to produce a low-density channel to reduce the nonlinear interactions of the ignition pulse in the underdense region. Plasma density channels were created using lasers with intensities of $I = 10^{17}$ to 10^{19} W/cm^2 in experiments of laser–solid target or laser–gas jet interactions.[17–20] Increased transmission of a trailing $I = 10^{20}$ W/cm^2 in the density channel was also observed.[19] Two dimensional (2-D) and three-dimensional (3-D) particle-in-cell (PIC) simulations of these experiments showed laser self-focusing in the plasma and channel generation through the ponderomotive force and resulting shock expansion.[18,21,22] Most of these previous experiments and simulations were done in 100-μm-scale plasmas.

The underdense region of an actual FI target, however, is about 1000 μm long. The residual plasma in the channel can continue to interact with the latter part of the channeling pulse and the ignition pulse. Later stages of the nonlinear evolution of the pulses and the channel need to be studied with full spatial scale simulations to obtain values of critical parameters such as the channeling time (T_c) and the required channeling pulse energy (E_c) and their scaling with the laser intensity I. These are needed to assess the viability of the hole-boring scheme and to plan for integrated experiments on next-generation FI facilities. This article presents results from 2-D PIC simulations with the code *OSIRIS*[23] showing that channeling in mm-scale plasmas is a highly nonlinear and dynamic process involving laser self-focusing and filamentation, channel generation via shock waves, longitudinal plasma snowplowing, laser hosing, and channel bifurcation and self-correction. As a result, the channeling speed oscillates and is much less than the laser

linear group velocity. We find that it eventually asymptotes to the expression obtained by conservation of momentum even for densities less than the critical density.

In our 2-D PIC simulations, a channeling pulse of wavelength λ_0 is launched from the left boundary of the simulation box with a peak intensity between $I = 10^{18}$ and 10^{20} $(1\ \mu\text{m}/\lambda_0)^2$ W/cm^2 and a rise time of 150 laser periods, after which the pulse amplitude is kept constant. The transverse profile is Gaussian with a full-width-at-half-maximum intensity spot size of $r_0 = 16$ to 47 λ_0 ($1/e$ spot size for the electric field, $w_0 = 90$ to 264 c/ω_0). It is focused onto a surface 600 λ_0 away from the left boundary. Both s- and p-polarizations are used to infer 3-D effects. The initial plasma density profile used is $n_0 = 0.1\ n_c \exp(x/L)$ with $L = 430\ \lambda_0$. (Length and time in these simulations are normalized to λ_0 and $1/\omega_0$, respectively, but $\lambda_0 = 1\ \mu$m is assumed so that the density scale length L is comparable to that of FI targets.) The ion-to-electron mass ratio is $m_i/m_e = 4590$, thereby approximating a DT plasma. The electron and ion temperatures are $T_e = T_i = 1$ keV. We simulate the region of $n_0 = 0.1$ to 1.02 n_c ($x = 0$ to 1000 λ_0) in two different setups. In the first setup we simulate the whole region in two separate simulations, one for $n_0 = 0.1$ to 0.3 n_c and the other for $n_0 = 0.3$ to 1 n_c. The simulation box size is $L_x = 477\ \lambda_0$ (longitudinal) and $L_y = 262\ \lambda_0$ (transverse) for the low-density portion and $L_x = 523\ \lambda_0$ and $L_y = 262\ \lambda_0$ for the high-density portion. The grid resolution in these simulations is $\Delta_x = 0.314\ c/\omega_0$ and $\Delta_y = 0.628\ c/\omega_0$. Ten particles per cell are used for each species in this setup. In the second setup we simulate the entire region in one simulation with a box size of $L_x = 987\ \lambda_0$ and $L_y = 401\ \lambda_0$ (totaling 19740×4010 cells). The grid resolution is kept the same but one particle per cell is used for each species.

We now describe general features of the channeling process using results from a simulation where $I = 10^{19}$ W/cm^2, $r_0 = 16\ \mu$m, and the laser was p-polarized. Other simulations with different intensities and/or with an s-polarized laser display similar features. The channeling pulse power P greatly exceeds the power threshold for relativistic self-focusing P_c (Ref. 4). For $n/n_c = 0.1$, $P/P_c = 300\ P/(10^{12}\ \text{W})$ $n/n_c \approx 780 \gg 1$ and r_0 is 32 c/ω_p. Therefore, relativistic whole-beam self-focusing and filamentation of the pulse[5] occur before significant plasma density perturbations arise. This initial phase is dominated by filamentation that is seeded by the Gaussian transverse profile since the initial r_0 is 32 c/ω_p [Fig. 112.20(a)]. As the laser self-focuses and filaments, the laser normalized vector potential a within each filament increases and the radius of each filament decreases. This causes the transverse ponderomotive force from each filament to increase so that significant electron density depletion occurs.[5] The space charge force ultimately causes the ions to follow, leading to the formation of several microdensity channels, with $n_{\max}/n_{\min} \approx 6$ [Fig. 112.20(b)].

Due to the fact that the microdensity channels form at different times along the laser propagation direction, the walls of the channels develop a longitudinal modulation. As new laser energy flows straight toward the filaments, the ponderomotive forces snowplow away the microchannels, eventually destroying them. This leads to the merging of neighboring mini-channels, eventually forming a single density channel centered along the axis of the laser [Fig. 112.20(c)]. At the end of this stage, a high-mach-number ion-acoustic shock is launched, causing the walls of the channel to move radially outward at a fairly constant speed of 0.03 c. The channel eventually becomes much wider than r_0.

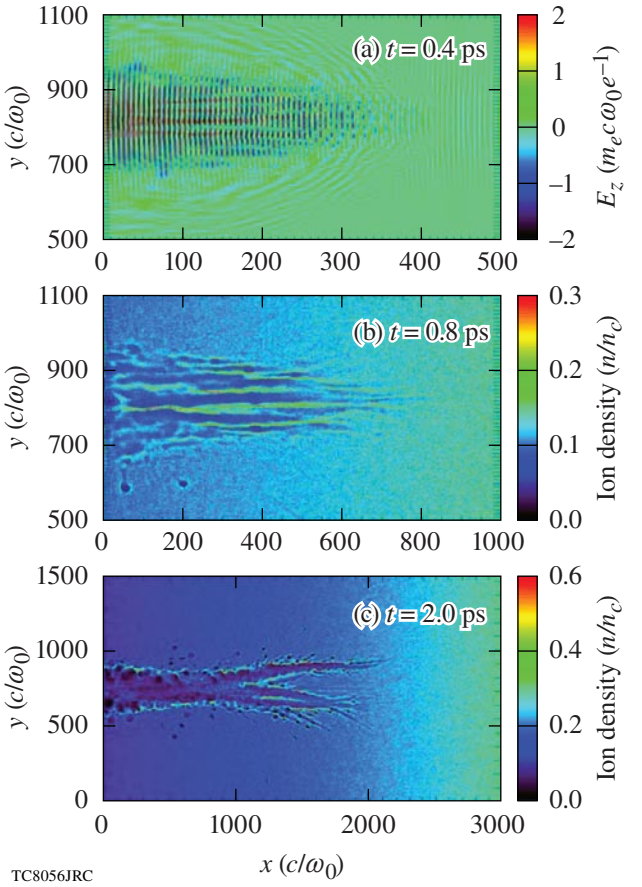

Figure 112.20
Results from a simulation with an $I = 10^{19}$ W/cm^2, p-polarized laser and $n_0 = 0.1$ to 0.3 n_c. (a) Laser E-field at $t = 0.4$ ps showing relativistic self-focusing and filamentation; (b) ion density at $t = 0.8$ ps showing the formation of microchannels; (c) ion density at $t = 2.0$ ps showing the formation of a single channel at the center for $x < 1000\ c/\omega_0$.

This entire process repeats as the laser and the head of the channel gradually advance toward the critical surface. Additionally, at the head of the channel, the density piles up to a value several times the local value of the initial density (Fig. 112.21). The density buildup grows as the channel digs into higher density. At regions of $n_0 > 0.55\ n_c$, the density compression exceeds n_c [Fig. 112.21(b)], thus making the subsequent pulse propagation similar to the hole-boring process, slower than the linear group velocity for the initial local density $v_g \equiv \sqrt{1 - n_0/n_c}$. While the transverse expansion is regular, the advance of the head of the channel is dynamic and intermittent. The channel can bend away from its center due to a long-wavelength hosing instability. This is seeded by hosing the head of the laser on the electron time scale as it propagates up the density gradient. For a finite-width pulse in a uniform plasma, the hosing instability[24] is caused by upward or downward tilting of local wavefronts due to a transverse phase velocity difference across the wavefronts. The phase velocity gradient is caused by the plasma density perturbation driven by the ponderomotive force of the hosing pulse.[25] The channel bends because of the hosing pulse, whose first occurrence is at $t \approx 3$ ps in the simulation with $n_0 = 0.1$ to $0.3\ n_c$ [Fig. 112.22(a)]. With the initial pulse parameters $a = 2.7$, $w = 90\ c/\omega_0$, and observed $k_h = (\pi/500)\ \omega_0/c$, the predicted growth rate in the long-wavelength regime,[25,26] $\gamma_{hu} = \left(a/\sqrt{8}\right)\left(c/\omega_0 w\right)k_h c \approx 0.13\ \text{ps}^{-1}$ may seem too slow for this observed time. However, self-focusing makes a larger and w smaller than their initial values and can increase γ_h. There is another channel-bending instability caused by the plasma pressure, but its growth rate $\gamma_{hp} \sim C_{sk_h} \sim 0.07\ \text{ps}^{-1}$ (Ref. 27) is too small even for $T_e = 1$ MeV.

As the channel hoses, the radius of curvature gradually increases. At some point the curvature becomes too severe to trap all of the incoming energy. As a consequence, some of

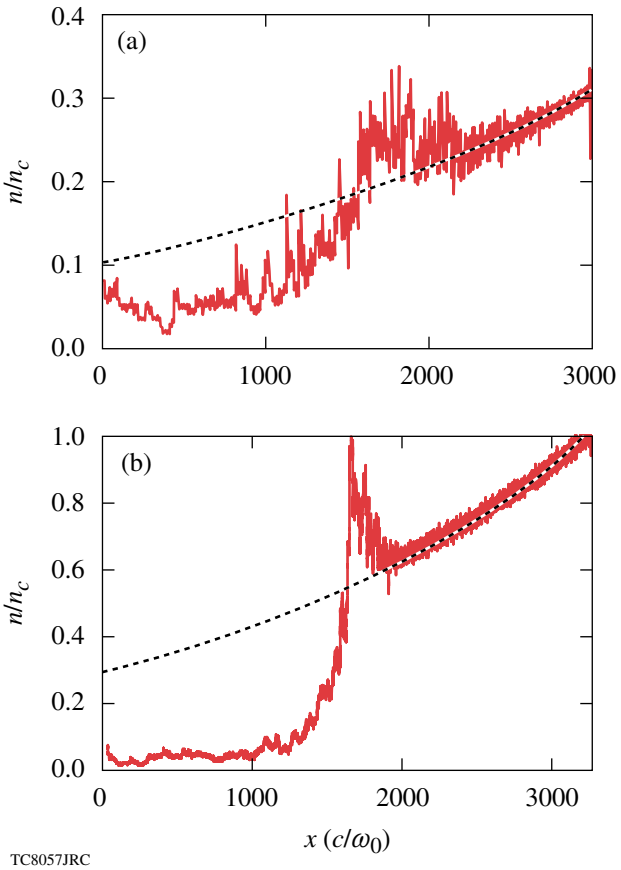

Figure 112.21
Average channel density plots for (a) $n_0 = 0.1$ to $0.3\ n_c$ at $t = 8.2$ ps and (b) $n_0 = 0.3$ to $1.0\ n_c$ at $t = 8$ ps showing the density pile-up. The dotted lines are the initial density profiles.

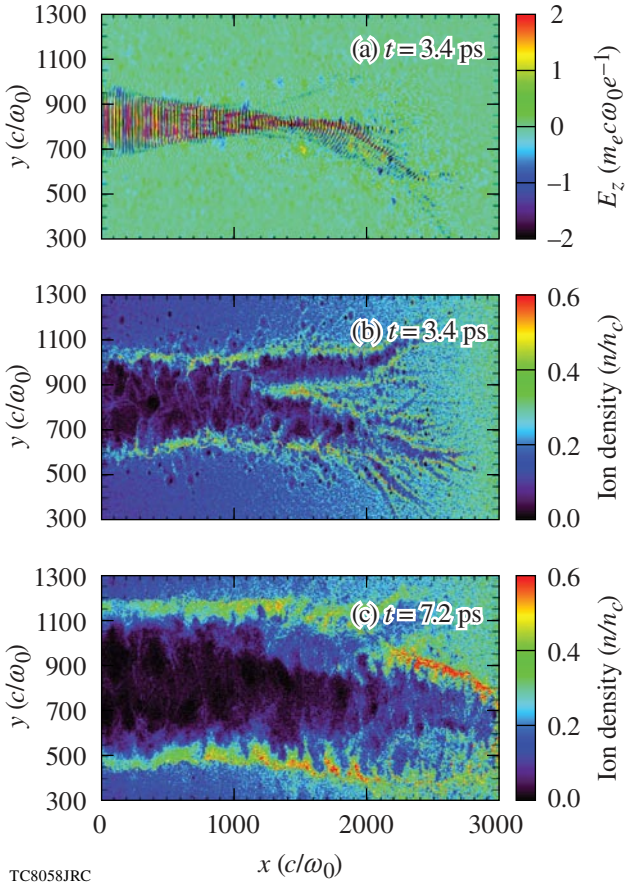

Figure 112.22
Results from a simulation with an $I = 10^{19}$ W/cm^2, p-polarized laser and $n_0 = 0.1$ to $0.3\ n_c$. (a) Laser E-field showing laser hosing; (b) ion density showing channel bifurcation at $t = 3.4$ ps; (c) ion density at $t = 7.2$ ps showing channel self-correction.

the laser energy breaks out of the channel to form a second branch of the channel that bends in the opposite direction. This process stalls the channel formation process. Both branches then advance deeper into the plasma, leaving a narrow plasma "island" in the middle of the entire channel [Fig. 112.22(b)]. Eventually, the island is pushed away by the ponderomotive force of the incoming laser energy and the two branches merge to form again a single channel [Fig. 112.22(c)]. This process of bifurcation and self-correction can repeat in a simulation lasting ~10 ps and provides a mechanism for the head of the channel to advance in propagation caused by the hosing-bending instability. Over time, the channel direction remains along the pulse propagation direction in our simulations.

Residual densities in the channel vary for different pulse intensities, from 0.1 n_c for $I = 10^{18}$ W/cm^2 to 0.04 n_c for $I = 10^{20}$ W/cm^2. To determine T_c, the time needed for the channel to reach the critical surface, under different pulse intensities, we define the channel as any location where the average plasma density is less than $n_r = 0.1\ n_c$. The average density, rather than the lowest density, in the channel is more relevant for the transmission of the ignition pulse. Specifically, the density is averaged transversely around the pulse center y_c, $y_c - w/2 < y < y_c + w/2$. The channel front X_c is defined as the location when the average density decreases to n_r and the channel advance speed is defined as $v_c = \mathrm{d}X_c/\mathrm{d}t$. Figure 112.23 plots the time for the channel to reach different density surfaces for three pulse intensities, measured from the one-particle-per-cell and p-polarization runs, and the resulting v_c for the $I = 10^{19}$ W/cm^2 case. It shows that v_c generally decreases as n_0 increases; however, v_c also oscillates as the channel advances, reflecting the underlying bifurcation and self-correction process seen in Figs. 112.22(b) and 112.22(c). We emphasize that v_c describes the speed of the density modification rather than the speed at which the laser energy advances. Figure 112.23(b) shows that v_c is much less than v_g and asymptotes to the ponderomotive hole-boring velocity [Eq. (1)]

$$v_{\mathrm{hb}} = 0.6\, c \sqrt{\frac{n_c}{n_0}\frac{m_e}{m_i}\frac{I\lambda_0^2}{10^{18}\ \mathrm{W}\mu\mathrm{m}^2/\mathrm{cm}^2}}\,, \tag{1}$$

as the front density buildup exceeds n_c. At the end of these simulations, the channel did not reach the critical surface. We estimate T_c by fitting and extrapolating the data in Fig. 112.23(a) and find T_c = 283, 72, and 15 ps for $I = 10^{18}$, 10^{19}, and 10^{20} W/cm^2, respectively. An intensity scaling can be found from this limited data set,

$$T_c \approx 2.9 \times 10^2 \left(I/10^{18}\ \mathrm{W/cm}^2\right)^{-0.64}\ \mathrm{ps}\,, \tag{2}$$

which enables us to obtain an intensity scaling for the total energy needed to reach the critical surface,

$$E_c \approx 1.7\left(I/10^{18}\ \mathrm{W/cm}^2\right)^{0.36}\ \mathrm{kJ}. \tag{3}$$

From this scaling we can see that the channeling pulse intensity should be kept as low as possible to minimize the total energy used in the channeling process. However, the ignition process needs to be completed within ~100 ps, which sets a lower bound for the channeling intensity to $I \approx 5 \times 10^{18}$ W/cm^2. If the self-focusing and other nonlinear interactions were neglected and channeling were taken to be the hole-boring process described

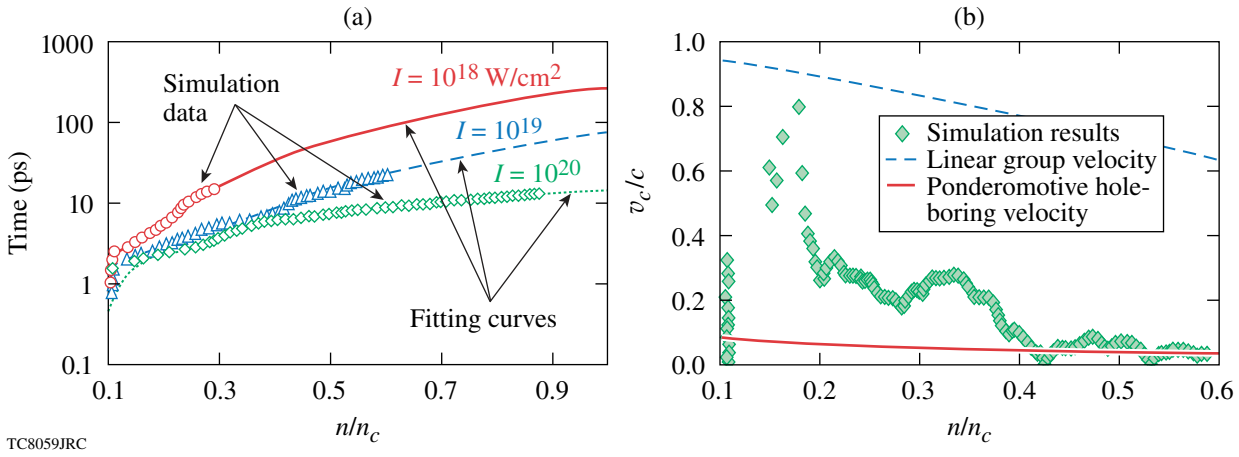

Figure 112.23
(a) Time for the channel to reach different initial densities under different pulse intensities and the corresponding fitting curves. Data were taken from the one-particle-per-cell and $n_0 = 0.1$ to 1.0 n_c runs. (b) The channeling speed v_c in the $I = 10^{19}$ W/cm^2 case.

by Eq. (1) from the beginning, analytical expressions for T_c and E_c can be obtained for density profiles dn/dx,

$$T_c^{(\mathrm{hb})} = \int \mathrm{d}n\left(\mathrm{d}n/\mathrm{d}x\right)^{-1}\Big/ v_{\mathrm{hb}} = 2.2 \times 10^2 \left(I\Big/10^{18}\ \mathrm{W}\Big/\mathrm{cm}^2\right)^{-0.5}\ \mathrm{ps},$$

and $E_c^{(\mathrm{hb})} \approx 1.3\left(I/10^{18}\ \mathrm{W/cm}^2\right)^{0.5}$ kJ for these simulations. That $T_c^{(\mathrm{hb})}$ and $E_c^{(\mathrm{hb})}$ are close to those from Eqs. (2) and (3) shows that despite the complexity of the channel formation, the channeling in these parameter regimes eventually becomes largely a ponderomotive process.

The scalings of Eqs. (2) and (3) are based on the available data set with p-polarization. The s-polarization data show a slightly larger v_c but similar scalings with intensities. The difference in v_c is due to less laser absorption in the channel walls in the s-polarization case than in the p-polarization case. In reality, the difference in the laser absorption at the channel walls in the directions perpendicular and parallel to the polarization may cause different expansion rates in the two directions, resulting in a noncircular channel cross section. In addition, self-focusing is stronger in 3-D than in 2-D, which may lead to a larger channeling speed in 3-D. These effects will be studied in future 3-D simulations with reduced scales; however, currently, full-scale 3-D simulations are not feasible even on the largest computers available.

In summary, channeling in the mm-scale underdense plasma of fast-ignition targets is a highly nonlinear and dynamic process. The channel expands transversely from density perturbations created by the relativistic and ponderomotive pulse self-focusing and filamentation. The density buildup near the channel front can eventually reach above the critical density, making the channeling speed much less than the linear group velocity of an electromagnetic wave. The channeling speed approaches estimates based on momentum conservation and 100% reflection of the laser at the density pile-up at the channel front[10] (although the second of these assumptions is not met). The scaling of the channeling time obtained from the PIC simulations indicates that a low-intensity channeling pulse is preferred to minimize the total channeling energy, but the intensity cannot be much lower than $I \approx 5 \times 10^{18}$ W/cm^2 if the channeling is to be completed within 100 ps. It is worth pointing out that for a typical fast-ignition target, the critical surface for 1-μm light will be roughly 600 μm in front of the target center. One way to move the channel closer to the core would be to use blue light ($\lambda = 0.35$ μm) for both the channeling and ignition pulses.

ACKNOWLEDGMENT

This work was supported by U.S. Department of Energy under Grants Nos. DE-FG02-06ER54879, DE-FC02-04ER54789, DE-FG52-06NA26195, and DE-FG02-03ER54721. Simulations were carried out at the National Energy Research Scientific Computing Center through an INCITE award and on the UCLA DAWSON Cluster under grant no. NSF-Phy-0321345. We wish to acknowledge useful discussions with Dr. R. Betti and Dr. W. Seka.

REFERENCES

1. J. D. Lindl, Phys. Plasmas **2**, 3933 (1995).
2. M. Tabak *et al*., Phys. Plasmas **1**, 1626 (1994).
3. R. Kodama *et al*., Nature **412**, 798 (2001); *ibid*. **418**, 933 (2002).
4. S. C. Wilks *et al*., Phys. Rev. Lett. **69**, 1383 (1992).
5. A. Pukhov and J. Meyer-ter-Vehn, Phys. Rev. Lett. **79**, 2686 (1997).
6. C. Ren *et al*., Phys. Rev. Lett. **93**, 185004 (2004).
7. C. Ren *et al*., Phys. Plasmas **13**, 056308 (2006).
8. J. C. Adam, A. Héron, and G. Laval, Phys. Rev. Lett. **97**, 205006 (2006).
9. C. K. Li and R. D. Petrasso, Phys. Rev. E **70**, 067401 (2004).
10. K-C. Tzeng, W. B. Mori, and C. D. Decker, Phys. Rev. Lett. **76**, 3332 (1996).
11. C. Max, J. Arons, and A. B. Langdon, Phys. Rev. Lett. **33**, 209 (1974).
12. G.-Z. Sun *et al*., Phys. Fluids **30**, 526 (1987).
13. P. Kaw, G. Schmidt, and T. Wilcox, Phys. Fluids **16**, 1522 (1973).
14. A. B. Langdon and B. F. Lasinski, Phys. Rev. Lett. **34**, 934 (1975).
15. D. W. Forslund, J. M. Kindel, and E. L. Lindman, Phys. Fluids **18**, 1002 (1975).
16. W. B. Mori *et al*., Phys. Rev. Lett. **60**, 1298 (1988).
17. M. Borghesi *et al*., Phys. Rev. Lett. **78**, 879 (1997).
18. J. Fuchs *et al*., Phys. Rev. Lett. **80**, 1658 (1998).
19. A. J. Mackinnon *et al*., Phys. Plasmas **6**, 2185 (1999).
20. K. A. Tanaka *et al*., Phys. Rev. E **60**, 3283 (1999).
21. A. Pukhov and J. Meyer-ter-Vehn, Phys. Rev. Lett. **76**, 3975 (1996).
22. Y. Sentoku *et al*., Fusion Sci. Technol. **49**, 278 (2006).
23. R. G. Hemker, "Particle-in-Cell Modeling of Plasma-Based Accelerators in Two and Three Dimensions," Ph.D. thesis, University of California, 2000; R. A. Fonseca, L. O. Silva, F. S. Tsung, V. K. Decyk, W. Lu, C. Ren, W. B. Mori, S. Deng, S. Lee, T. Katsouleas, and J. C. Adam, in *Computational Science—ICCS 2002*, edited by P. M. A. Sloot *et al*., Lecture Notes in Computer Science (Springer, Berlin, 2002), pp. 343–351.

24. G. Shvets and J. S. Wurtele, Phys. Rev. Lett. **73**, 3540 (1994); P. Sprangle, J. Krall, and E. Esarey, Phys. Rev. Lett. **73**, 3544 (1994).

25. C. Ren and W. B. Mori, Phys. Plasmas **8**, 3118 (2001).

26. B. J. Duda and W. B. Mori, Phys. Rev. B **61**, 1925 (2000); B. J. Duda *et al*., Phys. Rev. Lett. **83**, 1978 (1999).

27. E. Valeo, Phys. Fluids **17**, 1391 (1974).

Optimizing a Cleaning Process for Multilayer Dielectric (MLD) Diffraction Gratings

Introduction

The OMEGA EP Laser System consists of four beamlines, two of which will provide 1054-nm pulses having multikilojoule energies, picosecond pulse widths, petawatt powers, and ultrahigh intensities exceeding 10^{20} W/cm^2 (Ref. 1). These two beams can be directed into the existing OMEGA laser's target chamber for (1) fast-ignition experiments, which use a pulse of energetic electrons to heat the compressed fuel, thus igniting the fusion reaction,[2] and for (2) production of short pulses of x rays to "backlight" imploding fusion targets for diagnostic purposes.

The picosecond pulses are created by chirped-pulse amplification (CPA),[3] as shown in Fig. 112.24. To amplify the laser pulse without damaging the amplifier, a short pulse from the source is first chirped, or stretched into a longer, lower-power pulse in which the longer wavelengths travel at the front. The pulse is expanded in diameter, amplified, and then compressed by a series of four diffraction gratings. The compression occurs as the longer (red) wavelengths at the front of the amplified pulse are diffracted more and, therefore, forced to travel longer paths than the shorter (blue) ones. As a result, all wavelengths in the pulse arrive at the fourth grating at the same time. The fourth grating in the series experiences the shortest pulse length and is subjected to the highest fluence. The damage resistance of this last grating is the limiting element on the amount of energy that can be obtained in the compressed laser pulse. The last grating must be of a very high optical quality and have a high laser-damage threshold. The primary requirements for these large-aperture (43 cm × 47 cm) gratings are a high diffraction efficiency greater than 95%, peak-to-valley wavefront quality of less than $\lambda/10$ waves, and a high laser-induced-damage threshold greater than 2.7 J/cm^2 at 10-ps measured beam normal.

The multilayer dielectric (MLD) grating consists of a film of SiO_2, etched to form a grating structure with 1740 lines per millimeter. This structure resides on top of a multilayer dielectric high-reflector stack composed of alternating layers of SiO_2 and HfO_2. It is the cleanliness of this structure that is of paramount importance to survivability. Previous work at LLE has evaluated several candidate MLD cleaning protocols.[4] This article describes the results of an investigation to further optimize a final MLD-diffraction-grating cleaning process called "piranha clean" to increase laser-damage resistance.

Piranha Clean

Piranha solution is a mixture of sulfuric acid and hydrogen peroxide. This chemically aggressive agent has been used in the semiconductor industry for many years as the primary means of removing heavy organics like photoresist from wafers and photomasks. Typically, mixtures of H_2SO_4 (>95 wt%) and H_2O_2 (30 wt%) in volume ratios of 2 to 4:1 are used at temperatures of 80°C and higher. When hydrogen peroxide and sulfuric acid are mixed, "Caro's acid" [i.e., monopersulfuric acid (H_2SO_5)] is formed [Eq. (1)]. Caro's acid is the active etchant in a piranha bath.[5]

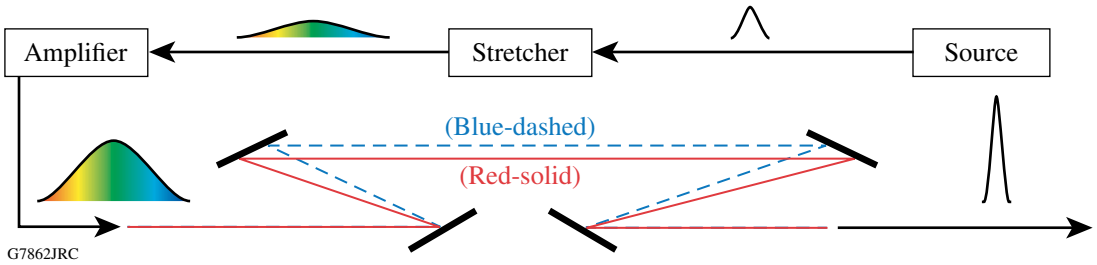

Figure 112.24
Diagram of chirped-pulse amplification. The pulse is amplified and then compressed by a series of four tiled-grating assemblies.

$$H_2O_2 + [HO-(SO_2)-OH] \rightleftarrows [HO-(SO_2)-O-OH] + H_2O. \quad (1)$$

As shown in Eq. (1), water is produced in the reaction between hydrogen peroxide and sulfuric acid. The presence of excess water in the mixture shifts the equilibrium toward the reactants, minimizing the production of Caro's acid. Therefore, using highly concentrated hydrogen peroxide (85 to 90 wt%) optimizes the production of Caro's acid; however, the use of highly concentrated hydrogen peroxide is extremely dangerous. For safety reasons, a lower concentration (30 wt%) is used. The excess water in 30-wt% H_2O_2 shifts the reaction away from the formation of H_2SO_5. The use of H_2O_2 in a low concentration also leads to significant heating of the piranha solution when the reactants are mixed. Caro's acid, which is heat sensitive, subsequently breaks down, resulting in a low-equilibrium concentration of this oxidizing acid. So, the mixture of H_2SO_4 and H_2O_2 requires higher temperatures to be effective in removing heavy organic materials like photoresist.

Experimental

Small (100-mm-diam) MLD diffraction gratings were fabricated at Plymouth Grating Laboratories (Fig. 112.25) by the following process steps:

1. *E*-beam deposit a 1053-nm, high-reflectivity multilayer coating of hafnium dioxide (HfO_2) and silicon dioxide (SiO_2) on a BK7 substrate.

2. Meniscus-coat a bottom organic antireflective coating (BARC) to the multilayer stack to eliminate standing wave effects; then meniscus-coat a PFI 88 (Sumitomo) positive photoresist layer.

3. Expose (pattern) the photoresist layer using a scanning-beam interference-lithography (Nanoruler) method. (The Nanoruler was developed by Dr. Mark Schattenburg at MIT. This exposure system moves a small UV laser beam over the substrate in overlapping scans to create a pattern of parallel lines in the photoresist. The gratings were patterned for 1740 lines/mm.)

4. Develop the patterned photoresist layer using an OPD262 developer.

5. Selectively remove the BARC layer with an O_2 reactive ion-beam-etch (RIBE) process.

6. Etch the SiO_2 grating layer using an $Ar/O_2/CHF_3$ RIBE process.

After step 6 above, gratings were shipped to LLE to evaluate the piranha clean process for removing (e.g., stripping) all photoresist and cleaning the grating surface. Two variables were examined: the ratio of H_2SO_4 to H_2O_2 and the treatment temperature.

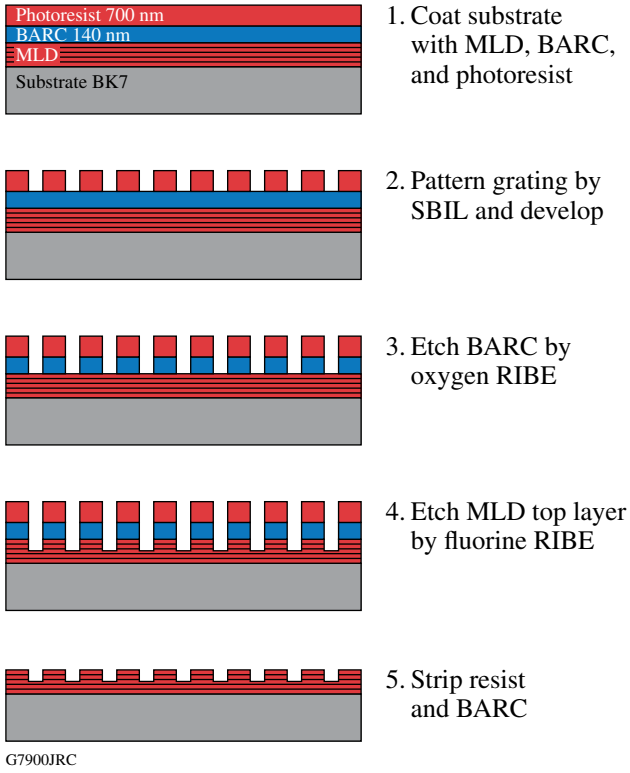

Figure 112.25
MLD grating fabrication process (figure not drawn to scale).

A sufficient number of gratings were cut into quarters to generate nine parts. A design-of-experiments (DOE) test was conducted with these parts to evaluate the influence of piranha solution composition and temperature on laser-damage threshold. The piranha clean process is shown schematically in Fig. 112.26. At a given treatment temperature, a part was immersed in a piranha bath of a given concentration and stirred for 20 min to strip the resist (step 1), subjected to a piranha rinse for less than 1 min (step 2), cleaned again for 10 min (step 3), rinsed in de-ionized water for approximately 3 min (step 4), then cooled to ~22°C and blown dry with filtered N_2 gas (step 5). Dried parts were evaluated for cleanliness by determining their laser-damage thresholds.

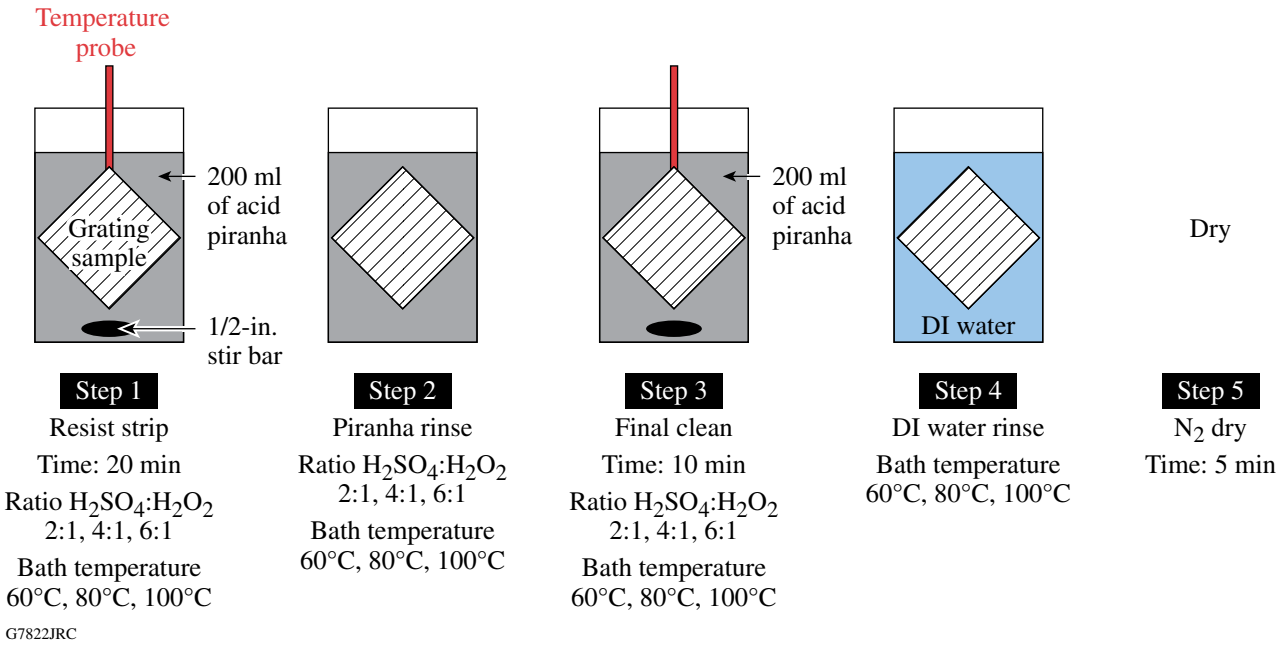

Figure 112.26
Piranha process. The variables within the experiment were the ratio of H_2SO_4 to H_2O_2 and the temperature of the piranha mixture.

Results

1. Laser-Damage Threshold

Laser-damage testing was conducted using a 10-ps-pulse, *s*-polarized laser operating at 1053 nm with an incident beam angle of 61° (diffracted beam of 72°). Both 1-on-1 and *N*-on-1 laser-induced-damage tests were performed. For 1-on-1 testing, individual sites on the grating are irradiated once with increasing energies until visible damage is observed. For *N*-on-1 testing, a single site is irradiated at increasing energies until damage is observed. The LLE specification for the damage threshold of our MLD gratings is >2.7 J/cm^2 at a 10-ps pulse length (for both 1-on-1 and *N*-on-1).

Figures 112.27 and 112.28 show the results of the damage-threshold tests that were measured for the different piranha clean processes. These results indicate that the temperature of the piranha mixture was the main variable, while the ratio of H_2SO_4 to H_2O_2 had a lesser effect. For both 1-on-1 and *N*-on-1

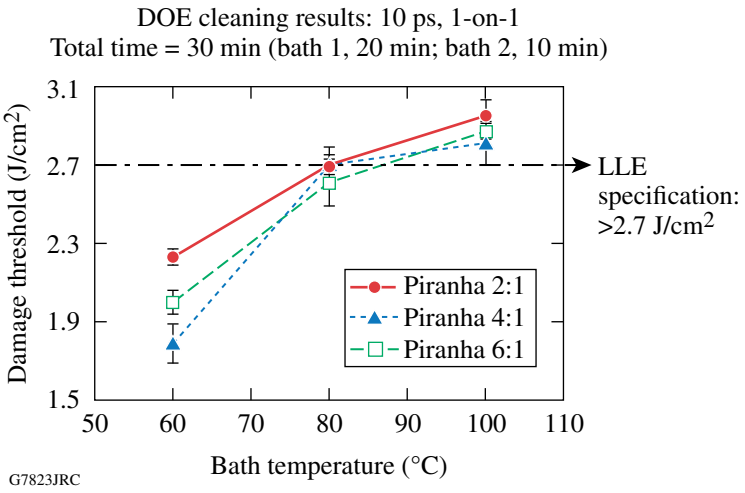

Figure 112.27
10-ps, 1-on-1 damage threshold at 1053 nm.

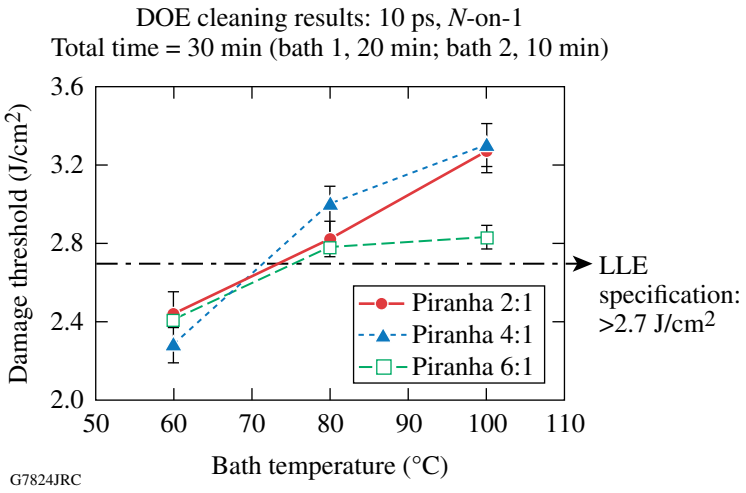

Figure 112.28
10-ps, *N*-on-1 damage threshold at 1053 nm.

tests, increasing the piranha temperature caused the grating laser-damage threshold to increase. This observation supports the discussion earlier in this article regarding the need to generate sufficient Caro's acid for efficient etch-cleaning. One could expect that further increases in bath temperatures would lead to even more enhanced laser-damage thresholds. Other work (not described here) has shown that higher process temperatures create thermal shock issues for small test gratings. The full-size grating elements used in OMEGA EP, consisting of 10-cm-thick plates of BK-7 glass, will not be subjected to cleaning process temperatures greater than 100°C. (Preliminary work to model this issue is reported elsewhere.[6])

2. SEM Analysis

Scanning electron microscopy (SEM) images were collected and analyzed for the highest (2:1, 100°C) and lowest (4:1, 60°C) damage-threshold MLD gratings that were cleaned in this study. The SEM images of the piranha 2:1, 100°C and piranha 4:1, 60°C processes indicate there is no visual residual contamination within either of the grating trenches. The SEM images, along with the associated laser-damage-threshold data for these gratings, are shown in Fig. 112.29. Since neither sample had visual contamination, SEM analysis is not useful in determining the root cause for the differences in damage-threshold values.

3. ToF-SIMS Analysis

The ToF-SIMS analysis was performed at Surface Science Western, University of Western Ontario. The instrument used was an ION-TOF (GmbH), TOF-SIMS IV, with a mass range of 1 to 1000 amu. To acquire positive and negative "shallow" depth profiles (i.e., meaning probing a few tens of nanometers into the surface), a 3-keV Cs^+ sputter ion beam was used for the negative secondary-ion profiles, while a 3-keV O_2^+ sputter ion beam was used for the positive secondary-ion profiles. The sputter-beam raster area was $500 \times 500\ \mu m^2$. Each sputter beam

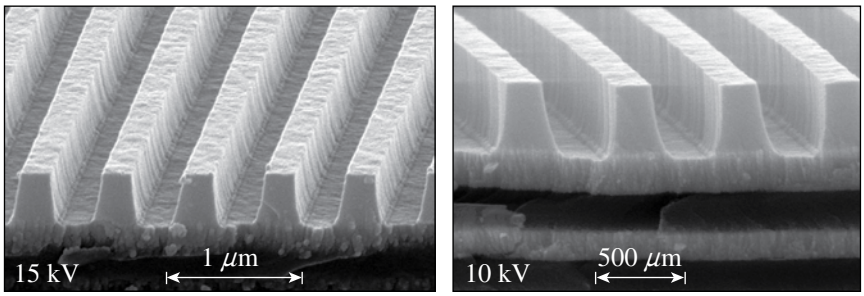

Piranha 2:1, 100°C, 30 min
Damage threshold:
10 ps, *N*-on-1: 3.27 J/cm^2
10 ps, 1-on-1: 2.95 J/cm^2

Piranha 4:1, 60°C, 30 min
Damage threshold:
10 ps, *N*-on-1: 2.29 J/cm^2
10 ps, 1-on-1: 1.79 J/cm^2

G7827JR

Figure 112.29
SEM images of the highest- and lowest-damage-threshold samples (piranha 2:1, 100°C; piranha 4:1, 60°C process). Laser-damage-threshold standard deviation for these samples is ±5%.

enhanced the secondary-ion yield through a reactive-ion effect for the given secondary-ion polarity. The Bi_3^+ analysis area was centered within this sputter crater, with a raster size of 200 × 200 μm^2. (Using a smaller raster size for analysis rather than the sputter crater size allows one to avoid edge effects during depth profiling.) By alternating the Bi_3^+ analysis and Cs^+/O_2^+ sputter beams, and inserting an electron flood-gun pulse in between for charge neutralization, a depth profile into the surface was acquired.[7]

A ToF-SIMS "shallow"-depth-profile analysis was conducted on the highest (piranha 2:1, 100°C) and lowest (piranha 4:1, 60°C) damage-threshold samples to determine if there was a correlation between higher contaminant ions and lower damage-threshold values. The relative intensities of the positive and negative ions detected versus the sputter time for the two samples were plotted to examine the differences between the two samples.

The data (see Fig. 112.30) indicate that there were significant levels of salt ions remaining within the lowest-damage-threshold samples (piranha 4:1, 60°C). The potassium (K^+) and sodium (Na^+) ions were the most abundant at the surface and into the grating. These salt ions are thought to have come from multiple contamination sources, including, possibly, the rinse water, developer, materials used during cleaning (beakers), and general handling.

Piranha process	10-ps, 1-on-1 (J/cm^2)	10-ps, *N*-on-1 (J/cm^2)
— 2:1 at 100°C	2.95	3.27
···· 4:1 at 60°C	1.79	2.29

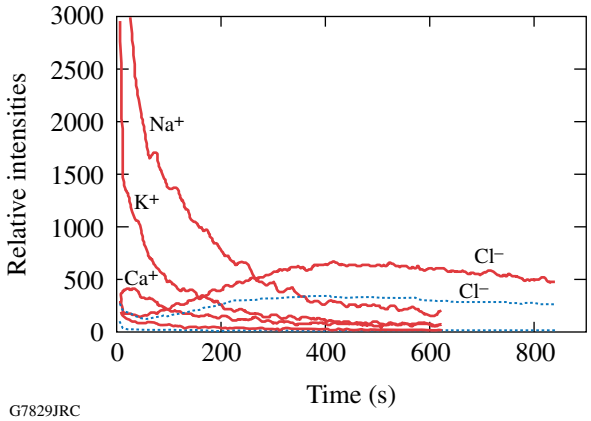

Figure 112.30
Salt-containing species. Piranha 4:1, 100°C has significant levels of salt remaining after clean. Laser-damage-threshold standard deviation for these samples is ±5%.

The carbon-ion species are shown in Fig. 112.31. The carbon ions are associated with the photoresist that was used in the fabrication process. This graph indicates that there were carbon (i.e., photoresist) species remaining at the surface and within the grating. The 4:1, 60°C sample had a much higher level of carbon ions than the 2:1, 100°C sample. There was also a high level of carbon implanted within the gratings. Since the top SiO_2 grating layer is amorphous, the resist was being driven into this surface. This correlates well with the damage-threshold values measured on these samples. Low-temperature piranha (with lower ratio) creates less Caro's acid and is ultimately less effective in removing organic contamination. This temperature effect can be seen clearly within our ToF-SIMS results.

Piranha process	10-ps, 1-on-1 (J/cm^2)	10-ps, *N*-on-1 (J/cm^2)
— 2:1 at 100°C	2.95	3.27
···· 4:1 at 60°C	1.79	2.29

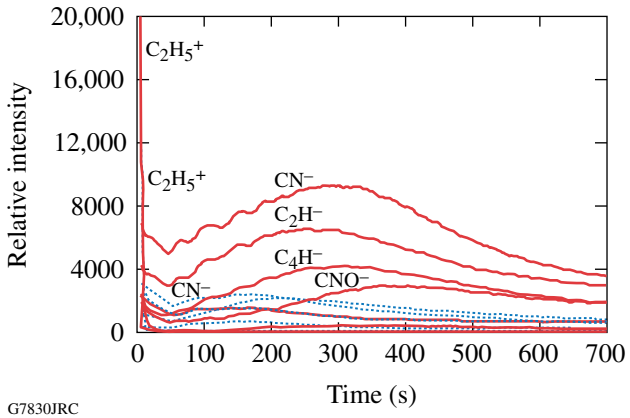

Figure 112.31
Carbon-containing species. Piranha 4:1, 100°C has significant levels of carbon (photoresist species) remaining after clean. Laser-damage-threshold standard deviation for these samples is ±5%.

Poor rinsing and neutralization of the piranha chemistry can over time cause problems at the grating surface. Residual sulfur-containing ions on or within the surface can cause surface haze (a common soft defect in the photomask industry). Figure 112.32 indicates that we did not completely rinse the piranha chemistry from the surface of the grating. The 4:1, 60°C sample had a much higher level of remaining sulfur ions than the 2:1, 100°C sample. This may be due to the lower-temperature piranha mixture not reacting completely with the carbon-resist species on the surface. The final rinse step to remove all of the piranha mixture will be very important in our final clean process to prevent the growth of sulfur-type haze.

Piranha process	10-ps, 1-on-1 (J/cm^2)	10-ps, *N*-on-1 (J/cm^2)
— 2:1 at 100°C	2.95	3.27
····· 4:1 at 60°C	1.79	2.29

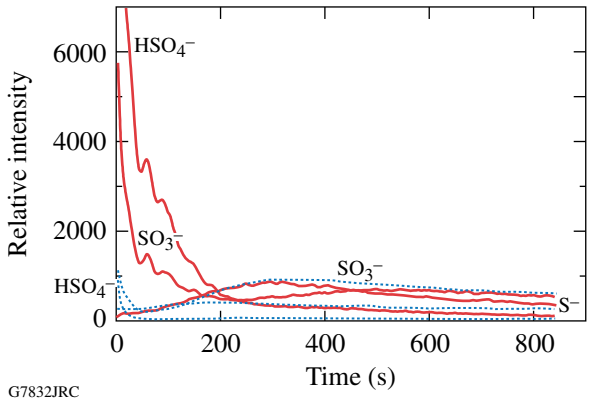

Figure 112.32
Sulfuric-containing species from incomplete rinse of the piranha mixture. Laser-damage-threshold standard deviation for these samples is ±5%.

Conclusions

The final clean removes any resist or particle contaminants that remain on the MLD diffraction grating after patterning and etch. Contaminant-removal efficiency in this step is critical to the performance of the grating within the laser system. The final clean employs a piranha mixture and DI water rinse to remove residual organic and other particulate and molecular contaminants. This final clean process must leave the surface free of unwanted contaminants and be able to produce high-damage-threshold gratings.

Using the 100-mm-diam MLD gratings fabricated at Plymouth Grating Laboratories, the final piranha cleaning process was optimized to achieve the OMEGA EP specification of >95% optical-diffraction efficiency and >2.7-J/cm^2 laser-damage threshold. The two main variables in the piranha process were the ratio of H_2SO_4 and H_2O_2 and the temperature of the mixture. Post-clean laser-damage threshold was measured for each cleaned sample. Additionally, scanning electron microscopy (SEM) and time-of-flight secondary ion-mass spectrometry (ToF-SIMS) "shallow"-depth-profile analysis was used to evaluate what type of contamination remained after the final clean process.

The laser-damage-threshold results indicate that as the ratio of H_2SO_4 to H_2O_2 increases within the piranha mixture, the damage threshold increases. Additionally, as the temperature is increased, the laser-damage threshold increases. From our data, there is a stronger correlation with the temperature of the piranha mixture.

ToF-SIMS shallow-depth-profile analysis provides an understanding of the contaminants on the surface as well as how far these contaminants are implanted into the grating surface. The analysis determined that the lowest-damage-threshold sample (4:1, 60°C) had considerably more contaminants on the surface and implanted into the grating. The low ratio and temperature piranha mixture was also unable to effectively rid the surface of the organic (i.e., photoresist) material and left considerable amounts of salts on the surface. Incomplete rinse and removal of the piranha mixture will leave sulfur-containing groups on the grating that may cause haze defects. LLE will use the information obtained in this study to scale up the piranha clean process to full-size gratings (43 × 47 × 10 cm).

ACKNOWLEDGMENT

This work was supported by the U.S. Department of Energy Office of Inertial Confinement Fusion under Cooperative Agreement No. DE-FC52-92SF19460, the University of Rochester, and the New York State Energy Research and Development Authority. The support of DOE does not constitute an endorsement by DOE of the views expressed in this article.

REFERENCES

1. L. J. Waxer, D. N. Maywar, J. H. Kelly, T. J. Kessler, B. E. Kruschwitz, S. J. Loucks, R. L. McCrory, D. D. Meyerhofer, S. F. B. Morse, C. Stoeckl, and J. D. Zuegel, Opt. Photonics News **16**, 30 (2005).

2. M. Tabak *et al*., Phys. Plasmas **1**, 1626 (1994).

3. D. Strickland and G. Mourou, Opt. Commun. **56**, 219 (1985).

4. B. Ashe, K. L. Marshall, C. Giacofei, A. L. Rigatti, T. J. Kessler, A. W. Schmid, J. B. Oliver, J. Keck, and A. Kozlov, in *Laser-Induced Damage in Optical Materials: 2006*, edited by G. J. Exarhos *et al*. (SPIE, Bellingham, WA, 2007), Vol. 6403, p. 64030O.

5. S. Verhaverbeke and K. Christenson, in *Contamination-Free Manufacturing for Semiconductors and Other Precision Products*, edited by R. P. Donovan (Marcel Dekker, New York, 2001), pp. 317–332.

6. Y. Zhang, Y. Wu, H. Liu, and J. C. Lambropoulos, in *Optical Manufacturing and Testing VII*, edited by J. H. Burge, O. W. Faehnle, and R. Williamson (SPIE, Bellingham, WA, 2007), Vol. 6671, p. 66710H.

7. Dr. J. Francis, Surface Science Western, ToF-SIMS Report, email reports and private communication (9 August 2006).

Shock Ignition of Thermonuclear Fuel with High Areal Densities

The energy gain[1] G of a direct-drive implosion is defined as the ratio between the thermonuclear energy yield and the laser energy on target. The gain is directly related to the capsule implosion velocity $G = \left(1/V_I^2\right)\eta_h \theta E_f / m_i$, where V_I is the implosion velocity, $\eta_h = E_K / E_L$ is the hydrodynamic efficiency representing the ratio between the shell kinetic energy and the laser energy on target, E_f = 17.6 MeV is the energy of the fusion products for a DT fusion reaction, and $m_i = 2.5\, m_H$ is the average ion mass. The function θ represents the fraction of burned fuel depending on the fuel areal density $\rho R \equiv \int_0^R \rho dr$. The function $\theta = \theta(\rho R)$ is commonly approximated[1] by $\theta \approx (1 + 7/\rho R)^{-1}$, where ρR is given in g/cm^2. The hydrodynamic efficiency of direct-drive implosions scales[2] as $\eta_h \sim V_I^{0.75} / I_L^{0.25} \lambda_L^{0.5}$, where I_L is the laser intensity on target and λ_L is the laser wavelength. It follows that the target gain scales as $G \sim 1/V_I^{1.25}$, indicating that high gains require low-velocity implosions. This is because low velocities are achieved by imploding massive shells and compressing large amounts of thermonuclear fuel. Since the areal densities are approximately independent of the implosion velocities,[2] the burn-up fraction depends only on the laser energy and fuel adiabat. Thus, low-velocity implosions of massive shells lead to high gains, provided that the fuel is ignited. However, the energy required to trigger ignition grows rapidly as the implosion velocity decreases. As shown in Ref. 3, the shell kinetic energy required for ignition scales as $E_K^{\text{ign}} \sim 1/V_I^6$ and low-velocity implosions fail to ignite at moderate driver energies. Large lasers in the 1-MJ energy range, such as at the National Ignition Facility, are expected to ignite relatively thin shells (initial aspect ratio ~5) driven at high velocities, ~4×10^7 cm/s, to achieve moderate gains of ~40 (Ref. 4). The performance of such implosions is sensitive to the growth of the Rayleigh–Taylor (RT) instability on the ablation front. The RT modes that can cause shell breakup during the acceleration phase have an inverse wave number $1/k$ comparable to the in-flight shell thickness d ($kd \sim 1$). The number of e-foldings of growth for such modes is about $\sqrt{\text{IFAR}}$, where IFAR is the in-flight aspect ratio, which scales[1] as $\sim V^2 / \alpha^{0.6} I_L^{0.27}$.

The parameter α represents the shell's in-flight adiabat defined as the ratio of the pressure to the Fermi pressure of a degenerate electron gas. For a fully ionized DT plasma, the adiabat is given by $\alpha = P(\text{Mb})/2.3\rho(\text{g/cc})^{5/3}$. To maximize the burn-up fraction (and the areal density), the adiabat must be kept low. It follows that the shell stability can be improved by lowering the IFAR through reducing the implosion velocity. Low-velocity implosions with low IFAR's have good stability properties during the acceleration phase. However, despite their good stability properties and potential for high gains, slow targets would fail to ignite for moderate driver energies because the hot-spot temperature and pressures are too low. For example, ignition at implosion velocities of ~2×10^7 cm/s and adiabats of $\alpha \sim 1$ require large multimegajoule laser drivers.

Here we show that a spherically convergent shock wave propagating through the shell during the coasting phase of the implosion enhances the compression of the hot spot, thus significantly improving the ignition conditions.[5] The ignitor shock is launched at the end of the laser pulse and must collide with the return shock near the inner shell surface. The return shock is the shock wave driven by the hot-spot pressure propagating outward through the shell. After the ignitor and return shock collide, a third shock wave, resulting from the collision, propagates inward, leading to further compression of the hot spot. The final fuel assembly develops a peaked pressure profile with its maximum in the center. Such non-isobaric assemblies exhibit a lower ignition threshold than standard isobaric ones.[5] This mechanism is effective only in thick-shell implosions, where the ignitor shock wave significantly increases its strength as it propagates through the converging shell.

This effect can be observed in simulations of realistic ICF implosions of thick shells like the one in Fig. 112.33 showing a thick wetted-foam shell with an outer radius of 852 μm, a 106-μm-thick layer of wetted foam CH(DT)$_6$, and a 240-μm-thick layer of DT ice. The initial shell aspect ratio (average shell radius/thickness) is about 2. One-dimensional simulations of a direct-drive implosion of such shells are carried out for the two 350-kJ, λ_L = 0.35-μm laser pulses shown in Fig. 112.34. The dashed curve represents a standard laser pulse, while the solid curve represents a shock-ignition laser pulse with a power

spike at the end of the pulse used to drive the ignitor shock. Both laser pulses use an intensity picket at the beginning of the pulse to shape the adiabat profile and to improve the target stability. The in-flight adiabat of the shell is $\alpha \approx 1$, the implosion velocity is $V = 2.5 \times 10^7$ cm/s, and the IFAR ≈ 17. The ultralow IFAR indicates that the integrity of the shell is not significantly affected by the Rayleigh–Taylor instability. The simulation of the implosions for the two laser pulses is carried out using the hydrocode *LILAC*. Figure 112.35 compares the pressure and density profiles at the time of peak compression for the standard pulse shape (dashed) and the shock-ignition pulse shape (solid). Notice that the hot-spot pressure for the shock-ignition pulse shape is about twice as high as for the standard pulse shape. While the target driven by the standard pulse is far from ignition, the shock-ignited target is at marginal ignition. Marginal ignition for a shock-ignited target is estimated by the size of the shock-launching-time ignition window, i.e., the time interval during which the ignitor shock needs to be launched to trigger ignition. If the ignition window is very narrow (only tens of picoseconds), the shock-ignited target is close to marginal ignition. To exceed the marginal ignition conditions and to widen the ignition window, the total laser energy needs to be increased.

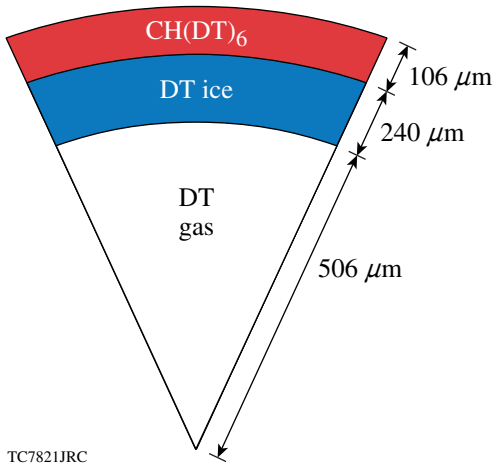

Figure 112.33
Thick wetted-foam target used in the shock-ignition simulations.

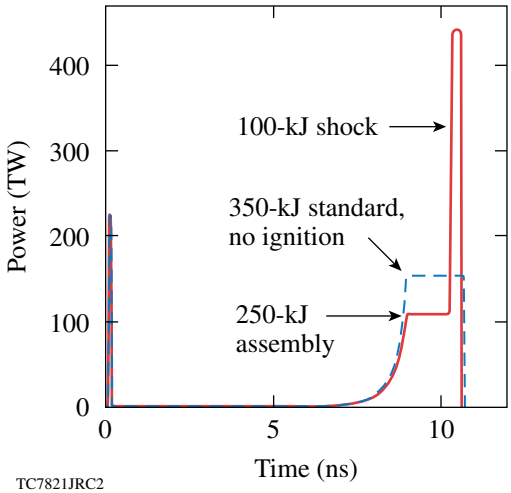

Figure 112.34
UV 350-kJ standard pulse shape (dashed) and shock-ignition pulse shape (solid).

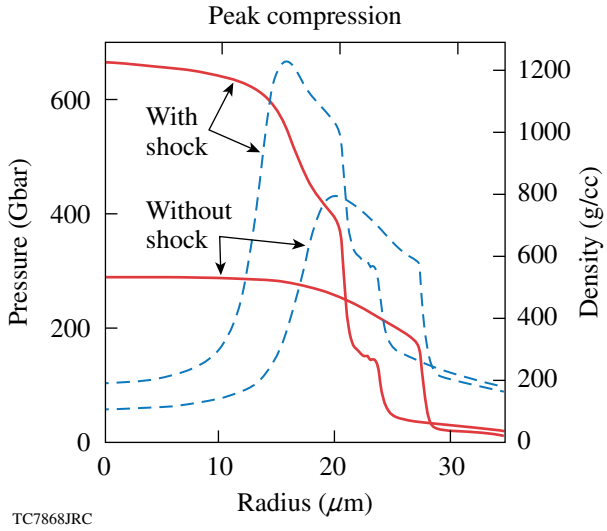

Figure 112.35
Density (dashed) and pressure (solid) profiles at peak compression for the standard and shock-ignition pulse shape.

Since the laser intensity during the power spike is considerably higher than during the assembly pulse, hot electrons can be generated in the corona by laser–plasma instabilities. In standard implosions, hot electrons can preheat the shell, thus raising the adiabat, reducing the final compression, and preventing the ignition of the hot spot. In shock ignition, hot electrons generated during the power spike may have a positive effect on the implosions. Since the areal density grows rapidly in time during the final stages of the implosion, the range of the hot electrons from the intensity spikes is less than the shell thickness. In this case, the hot electrons are stopped on the shell surface and help drive the ignitor shock. Figure 112.36 shows a plot of the laser intensity (solid curve) and the areal density evolution (dashed curve) during the power spike. Since the ρR range of 100-keV electrons in DT (about 17 mg/cm^2, dashed line in Fig. 112.36) is much smaller than the shell areal density (50 to 80 mg/cm^2) during the spike, the hot electrons

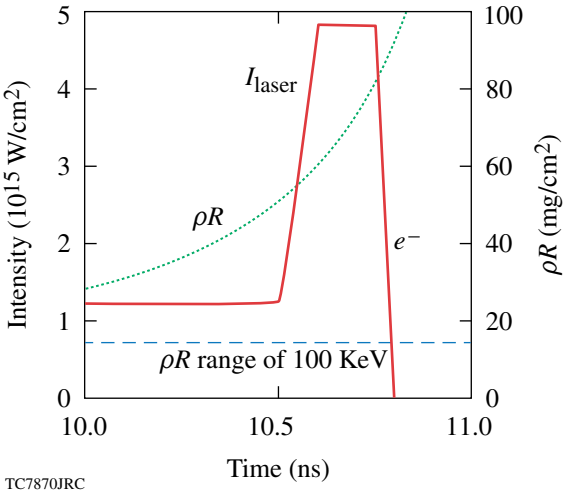

Figure 112.36
Evolution of the laser intensity (solid) and the areal density (dashed) during the power spike.

of moderate energy (~100 keV) are stopped before penetrating deep into the shell, thus augmenting the strength of the ignitor shock. The effects of hot electrons are included in the simulations through a multigroup diffusion model for the hot electrons as described in Ref. 6. In the simulations, the hot electrons are generated isotropically during the power spike in the corona with their birth temperature set at 150 keV and with a Maxwellian distribution function. The total energy into hot electrons is assumed to be 25% of the laser energy during the power spike. As shown in Fig. 112.37, the ignition window

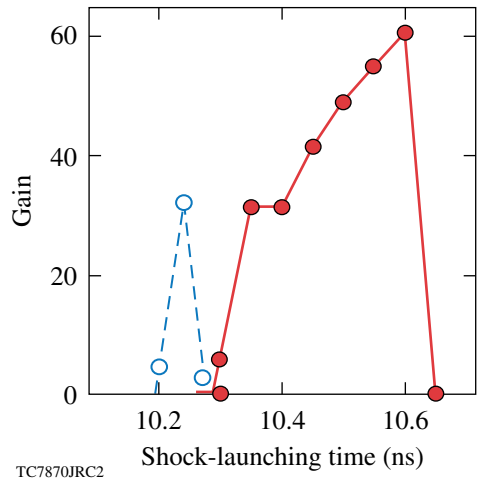

Figure 112.37
Shock-launching-time ignition window with (solid) and without (dashed) hot electrons.

is considerably wider when the effects of hot electrons are included in the simulation, thus showing that hot electrons can indeed benefit the shock-ignition scheme as long as their range does not exceed the shell thickness.

Another important effect to be included in shock-ignition targets is the long mean free path of the thermal coronal electrons heated to high temperatures during the power spike. The power spike raises the coronal electron temperatures to about 7 keV, causing the heat-carrying electrons to free-stream to the ablation front, thus enhancing heat conduction. A nonlocal heat-conduction model is, therefore, required to adequately model the electron heat transfer during the power spike. To estimate the effects of nonlocal heat transport, the model of Ref. 7 is included in the simulations of the ignitor-shock generation during the power spike. The new conditions for ignition and gain are computed in terms of the ignition window and shown in Fig. 112.38. As expected, the long-mean-free-path electrons augment the heat transfer during the power spike, thus driving a stronger ignitor shock. The ignition window is widened by nonlocal transport, and the gain is higher than without nonlocal effects.

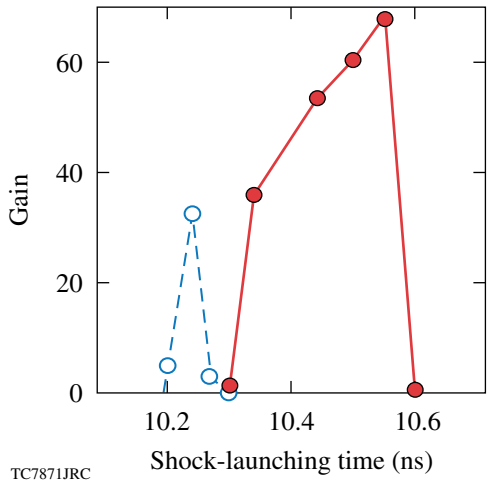

Figure 112.38
Ignition window with (solid) and without (dashed) nonlocal heat transport.

It is shown that a two-step ignition scheme can be configured by combining a fuel-assembly laser pulse and a shock-driving power spike. The ignitor shock enhances the compression of the hot spot, thus leading to a significant reduction of the energy required for ignition and high gains. A powerful laser pulse or particle beam can be used to drive the ignitor shock to trigger ignition at relatively low driver energies.

ACKNOWLEDGMENT

This work was supported by the U.S. Department of Energy Office of Fusion Energy Science and Office of Inertial Confinement Fusion under Cooperative Agreement No. DE-FC02-04ER54789 and DE-FC52-92SF19460, the University of Rochester, and the New York State Energy Research and Development Authority. The support of DOE does not constitute an endorsement by DOE of the views expressed in this article.

REFERENCES

1. J. D. Lindl, *Inertial Confinement Fusion: The Quest for Ignition and Energy Gain Using Indirect Drive* (Springer-Verlag, New York, 1998).
2. R. Betti and C. Zhou, Phys. Plasmas **12**, 110702 (2005).
3. M. C. Herrmann, M. Tabak, and J. D. Lindl, Nucl. Fusion **41**, 99 (2001).
4. P. W. McKenty, V. N. Goncharov, R. P. J. Town, S. Skupsky, R. Betti, and R. L. McCrory, Phys. Plasmas **8**, 2315 (2001).
5. R. Betti, C. D. Zhou, K. S. Anderson, L. J. Perkins, W. Theobald, and A. A. Solodov, Phys. Rev. Lett. **98**, 155001 (2007).
6. J. Delettrez and E. B. Goldman, Laboratory for Laser Energetics, University of Rochester, Rochester, NY, LLE Report No. 36 (1976).
7. G. P. Schurtz, Ph. D. Nicolaï, and M. Busquet, Phys. Plasmas **7**, 4238 (2000).

LLE's Summer High School Research Program

During the summer of 2007, 14 students from Rochester-area high schools participated in the Laboratory for Laser Energetics' Summer High School Research Program. The goal of this program is to excite a group of high school students about careers in the areas of science and technology by exposing them to research in a state-of-the-art environment. Too often, students are exposed to "research" only through classroom laboratories, which have prescribed procedures and predictable results. In LLE's summer program, the students experience many of the trials, tribulations, and rewards of scientific research. By participating in research in a real environment, the students often become more excited about careers in science and technology. In addition, LLE gains from the contributions of the many highly talented students who are attracted to the program.

The students spent most of their time working on their individual research projects with members of LLE's technical staff. The projects were related to current research activities at LLE and covered a broad range of areas of interest including experimental diagnostic development and analysis, computational modeling of implosion hydrodynamics and electron transport, database development, materials science, computational chemistry, and solid-state switch development (see Table 112.IV).

The students attended weekly seminars on technical topics associated with LLE's research. Topics this year included laser physics, fusion, holographic optics, fiber optics, liquid crystals, error analysis, and global warming. The students also received safety training, learned how to give scientific presentations, and were introduced to LLE's resources, especially the computational facilities.

The program culminated on 29 August with the "High School Student Summer Research Symposium," at which the students presented the results of their research to an audience including parents, teachers, and LLE staff. The students' written reports will be made available on the LLE Web site and bound into a permanent record of their work that can be cited in scientific publications.

Two hundred and eighteen high school students have now participated in the program since it began in 1989. This year's students were selected from approximately 50 applicants.

At the symposium it was announced that Mr. Christian Bieg, a physics teacher at Fairport High School, is the recipient of the 11th annual William D. Ryan Inspirational Teacher Award. This award is presented to a teacher who motivated one of the participants in LLE's Summer High School Research Program to study science, mathematics, or technology and includes a $1000 cash prize. Teachers are nominated by alumni of the summer program. Mr. Bieg was nominated by Rui Wang, a participant in the 2006 Summer Program and a finalist in the 2007 Intel Science Talent Search. "I have moved around the globe during my years of primary and secondary education," Rui wrote in her nomination letter, "yet the teacher whose dedication to science and education has inspired me the most is Mr. Bieg … Mr. Bieg was not only passionate about physics and teaching, but also knew exactly how to bring out the curious side in everyone … He had promised us on the first day that we would never see the world the same way after each class, and, of course, he kept his promise." Mr. David Paddock, principal of Fairport High School, added, "Chris Bieg is an outstanding teacher … He has the ability to make the subject interesting and fun to all students, even those who may not generally favor science. Chris … serves as a wonderful role model for his students."

Table 112.IV: High School Students and Projects—Summer 2007.

Name	High School	Supervisor	Project Title
Joshua Bell	Churchville-Chili	W. R. Donaldson	Development of a GaAs Photoconductive Switch for the Magneto-Inertial Fusion Electrical Discharge System
Margaret Connolly	Mercy	T. C. Sangster, M. McCluskey, S. Roberts	Response of CR-39 to Heat Exposure
Juraj Culak	Brighton	P. B. Radha	Neutron Imaging of Inertial Confinement Fusion Implosions
Daniel Fleischer	Brighton	R. Boni, P. A. Jaanimagi	ROSS Performance Optimization
Jean Gan	Pittsford Sutherland	K. L. Marshall	Patterned Photoresist Spacers and Photo-Induced Alignment Coatings for Liquid Crystal Waveplates and Polarizers
Roy Hanna	Williamsville	J. A. Delettrez	Extension of the Modeling of Blooming and Straggling of the Electron Beam in the Fast-Ignition Scenario
Katherine Manfred	Fairport	R. S. Craxton	Polar-Direct-Drive Simulations for a Laser-Driven HYLIFE-II Fusion Reactor
Richard Marron	Allendale Columbia	R. Kidder	Creation of an Ontology for the OMEGA EP Laser System
Alan She	Pittsford Mendon	R. S. Craxton	Thermal Conductivity of Cryogenic Deuterium
Benjamin Smith	Webster Schroeder	L. M. Elasky	Expansion of Search Capabilities for the Target Fabrication Database
Alexander Tait	Allendale Columbia	W. A. Bittle	Data Analysis for Electro-Magnetic Pulse Measurements
Ernest Wang	Pittsford Mendon	K. L. Marshall	Computational Modeling of Spectral Properties of Azobenzene Derivatives
Eric Welch	Livonia	J. P. Knauer	Design of an X-Ray Photoconductive Device Spectrometer
Andrew Yang	Fairport	R. Epstein	Unfolding X-Ray Spectra from a Multichannel Spectrometer

FY07 Laser Facility Report

The OMEGA Facility conducted 1514 target shots for a variety of users in FY07 (see Table 112.V). A total of 27 D_2 and 17 DT low-adiabat cryogenic target implosions that required high-contrast pulse shapes were performed. Such pulse shapes are typically characterized by a narrow picket pulse on top of a low-intensity foot pulse, followed by a high-intensity drive pulse (see Fig. 112.39). Substantial strides have been made with low-adiabat-drive pulse shapes and shock timing. Small picket timing and intensity changes have been demonstrated to effect cryogenic target areal-density measurements in agreement with theory. OMEGA Availability and Experimental Effectiveness averages for FY07 were 92.8% and 95.9%, respectively. Highlights of other achievements for FY07 include the following:

- An offline OMEGA frequency-conversion-crystal (FCC) tuning test bed was developed and activated to tune new OMEGA and OMEGA EP FCC's. This facility supports the ongoing refurbishment of OMEGA crystals and is used to precisely characterize the performance of OMEGA EP FCC's.

- More than 25 new or significantly modified target-diagnostic systems were qualified for use on the OMEGA Experimental Facility in FY07. These diagnostics supported LLE, LLNL, LANL, AWE, and CEA experiments and all were supported by LLE and the cognizant laboratory. Diagnostic improvements in FY 2007 include

  – integration of the LLNL/OMEGA high-resolution velocimeter (OHRV) diagnostic,

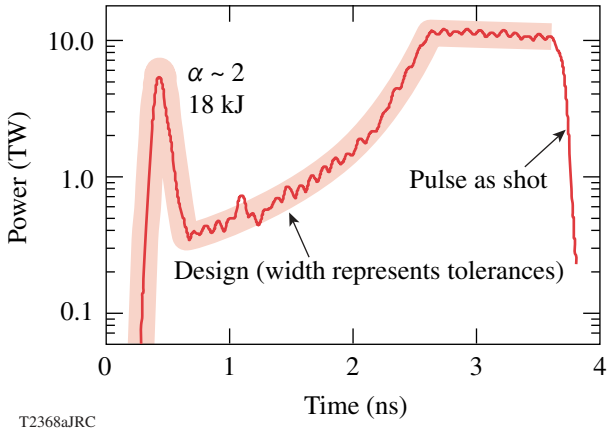

Figure 112.39
OMEGA single-beam pulse shape from a low-adiabat cryogenic target implosion (shot 47206) using pulse shape HE363001p.

Table 112.V: The OMEGA target shot summary for FY07.

Laboratory	Planned Number of Target Shots	Actual Number of Target Shots	IDI NIC	DDI NIC	Total NIC	Non-NIC
LLE	629	698	174	502	676	22
LLNL	386	422	235	0	235	187
LANL	158	192	73	0	73	119
NLUF	117	121	0	0	0	121
CEA	40	40	0	0	0	40
AWE	20	26	0	0	0	26
SNL	11	15	15	0	15	0
Total	1361	1514	497	502	999	515

  - upgrade of the active shock breakout (ASBO) diagnostic with a new long-pulse laser system, two ROSS streak cameras, and an off-axis telescope option,

  - integration of an electromagnetic interference (EMI) monitor system to provide baseline and operational data to support short-pulse operations,

  - activation of the magneto inertial fusion energy delivery system (MIFEDS), and

  - qualification of nine x-ray imaging and spectrometer diagnostics.

Significant modifications were made to the OMEGA Laser Facility in FY07 to integrate the OMEGA EP short-pulse beam into the OMEGA target chamber. These modifications include the following:

- Ten-inch manipulator #2 was modified for near-vertical operation and moved from port H7 to port H3.

- The gated microchannel-plate x-ray imager (GMXI) was modified and moved from port H9 to port H12.

- The turning mirror structure and surrounding platform were extensively modified to accommodate the short-pulse beam tube (SPBT) and the off-axis parabola inserter/manipulator (OAPI/M); these modifications include replacing two segments of the personnel platform and the addition of a new two-level platform to provide personnel access.

- The bore diameter of port H7 was increased to provide clearance for the off-axis parabola.

- The SPBT connecting the OMEGA target chamber to the OMEGA EP grating compressor chamber (GCC) was installed.

National Laser Users' Facility and External Users' Programs

During FY07, 826 target shots were taken on OMEGA for external users' experiments, accounting for 54.6% of the total OMEGA shots for the year. The external users during this year included six collaborative teams participating in the National Laser Users' Facility (NLUF) program and many collaborative teams from the national laboratories (LLNL, LANL, and SNL), the Commissariat à l'Énergie Atomique (CEA) of France, and the Atomic Weapons Establishment (AWE) of the United Kingdom.

FY07 NLUF Experiments

FY07 was the first of a two-year period of performance for the NLUF projects approved for the FY07–FY08 funding and OMEGA shots (see Table 112.VI). Six of these NLUF projects were allotted OMEGA shot time and received a total of 131 shots on OMEGA in FY07. Some of this work is summarized in this section.

Recreating Planetary Core States on OMEGA in FY07

Principal Investigator: R. Jeanloz (University of California, Berkeley)

Co-investigators: J. H. Eggert, P. M. Celliers, S. Brygoo, D. G. Hicks, and G. W. Collins (LLNL); P. Loubeyre (CEA); T. R. Boehly (LLE); S. McWilliams and D. Spaulding (U.C. Berkeley)

The approach to recreate planetary core states in the laboratory involves driving a laser-induced shock through a sample already precompressed in a diamond-anvil cell (Fig. 112.40). This combines the benefits of static and dynamic high-pressure experiments, allowing the final pressure–volume–temperature (P–V–T) state of the sample to be tuned across a broad range of thermodynamic conditions. Much higher densities are achieved through this approach than through traditional shock-wave

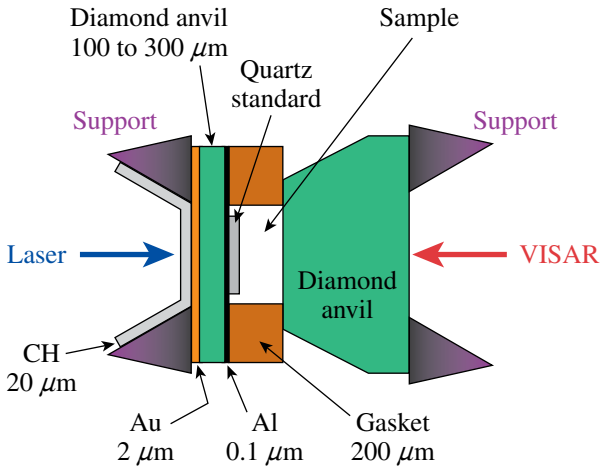

Figure 112.40
Schematic cross section of the diamond cell. The diamond anvil on the entry (drive laser) side must be thin in order to minimize attenuation of the shock front before it enters the sample, and diagnostics include velocity interferometry system for any reflector (VISAR) as well as pyrometry (not shown) collected through the thicker anvil on the exit side.

Table 112.VI: FY07–FY08 NLUF Experiments.

Principal Investigator	Affiliation	Proposal Title
R. Jeanloz	University of California, Berkeley	Recreating Planetary Core States on OMEGA in FY07
R. P. Drake	University of Michigan	Experimental Astrophysics on the OMEGA Laser
P. Hartigan	Rice University	Laboratory Experiments on Supersonic Astrophysical Flows Interacting with Clumpy Environments
R. Mancini	University of Nevada, Reno	Multiview Tomographic Study of OMEGA Direct-Drive-Implosion Experiments
R. D. Petrasso, C. K. Li	Massachusetts Institute of Technology	Monoenergetic Proton Radiography of Laser–Plasma-Generated Fields and ICF Implosions
R. Falcone, H. J. Lee	University of California, Berkeley	X-Ray Compton Scattering on Compressed Matter

(Hugoniot) measurements because thermal effects come to dominate the latter but are suppressed by the precompression.

Thus, states directly relevant to the deep interiors of giant planets are reproduced, and we can study interatomic-bonding forces at much closer packing than is otherwise possible through laboratory experiments. This is important both for planetary science and for validating (and extending) the condensed-matter theory based on first-principles quantum-mechanical calculations.

This year we developed a technique that uses quartz as a reference standard for Hugoniot, temperature, and reflectivity measurements of planetary fluids.[1] This new technique greatly reduces the uncertainty of shock-compression data, and measurements were completed for He.[2] This work establishes how the compressibility changes with ionization and interparticle interaction and will serve as a key benchmark for models of the evolution and structure of solar and extra-solar giant planets. Temperature and reflectivity measurements on He were also finished this year, and we have collected the highest-density and pressure data for He.[3]

In addition to He, we have finished collecting shocked precompressed data on H_2 and D_2. While the deuterium data (for samples that start at the same density as liquid deuterium), have the same compressibility as impedance-matched liquid deuterium, contrasting H_2 and D_2 measurements reveals an interesting isotope dependence for the compressibility. In essence, the hydrogen shows a larger compressibility than deuterium at the same precompressed pressure. This is likely because the compressibility is sensitive to the excitation of degrees of freedom that increases the compressibility and the interparticle interaction that increases pressure and reduces the compressibility. In fact, all the tabular equation-of-state (EOS) models show this signature, with the maximum compressibility decreasing with precompression (still, the final density increases with precompression). Hydrogen, which has a larger zero-point volume because of its smaller mass, behaves like deuterium, having a lower initial density.

The reflectivity and temperature data for hydrogen reveal that contours of constant reflectance are nearly parallel to the predicted plasma phase transition derived from Saumon and Chabrier[4] and from Bonev's density functional calculations[5] (Fig. 112.41).

Finally we have finished our first set of measurements on He/H_2 mixtures, finding that the temperature and optical reflectivity are between those of He and H_2. The reflectivity of He increases slowly with shock pressure as compared to H_2. At the same time, the temperature of He increases rapidly with shock pressure as compared to H_2. These two observations are related: the reason H_2 stays colder with increasing shock pressure compared to He (over the pressure range studied) is because H_2 dissociates; also, it ionizes at much lower shock pressure than He, and the dissociation and ionization (which leads to enhanced optical reflectance) lower the shock tempera-

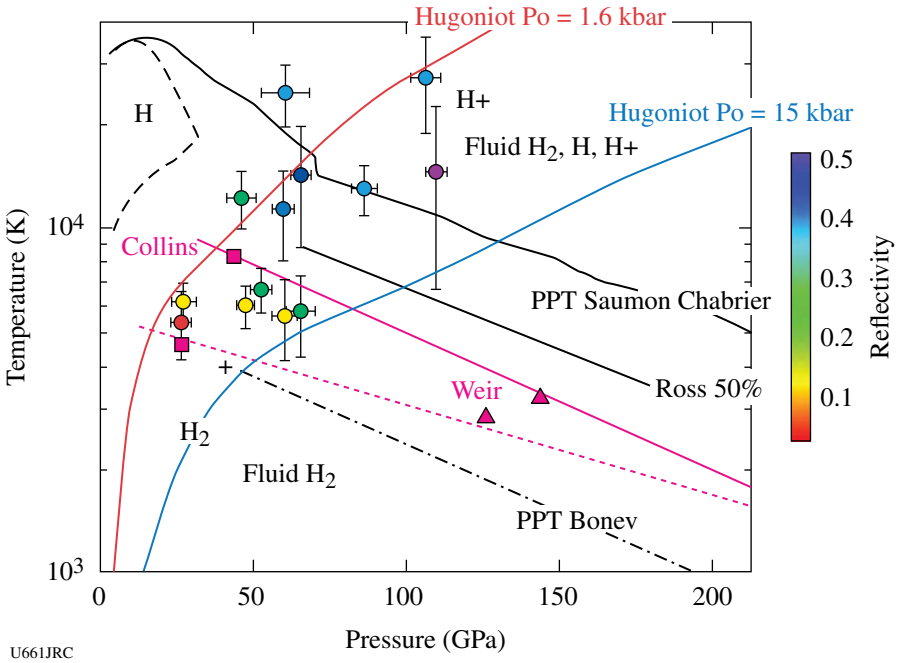

Figure 112.41
Reflectivity versus temperature and pressure for shocked precompressed H_2. Data show a continuous transition between the molecular and plasma phases in this range of temperature and pressure.

ture. Over the same pressure range (0.1 to 2 Mbar), He exhibits much lower ionization. Therefore, increasing shock pressure rapidly increases shock temperature.

The 50/50 mixture of He/H_2 shows that the temperature and shock reflectivity lie between those of H_2 and He, suggesting that the mixture can be modeled as ideal (Figs. 112.42 and 112.43).

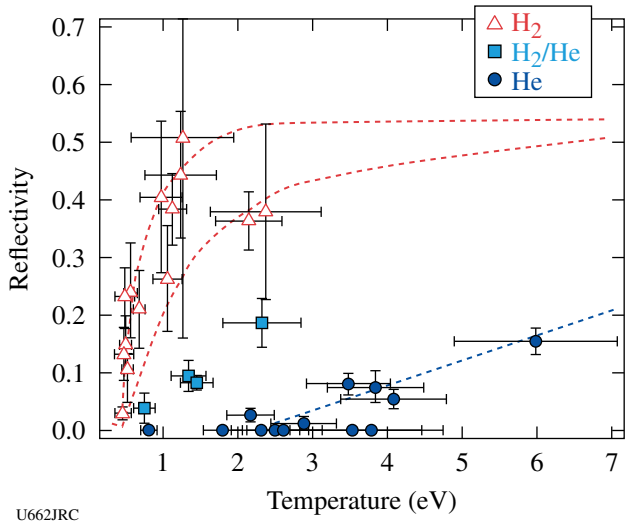

Figure 112.42
Reflectivity versus temperature for H_2, He, and a 50/50 mixture of H_2/He. These data start off at very different initial densities but, since the reflectivity is largely temperature dependent, the reflectivity for each material follows a specific trend. The reflectivity (and the temperature versus pressure) for the mixture is intermediate between that of H_2 and He.

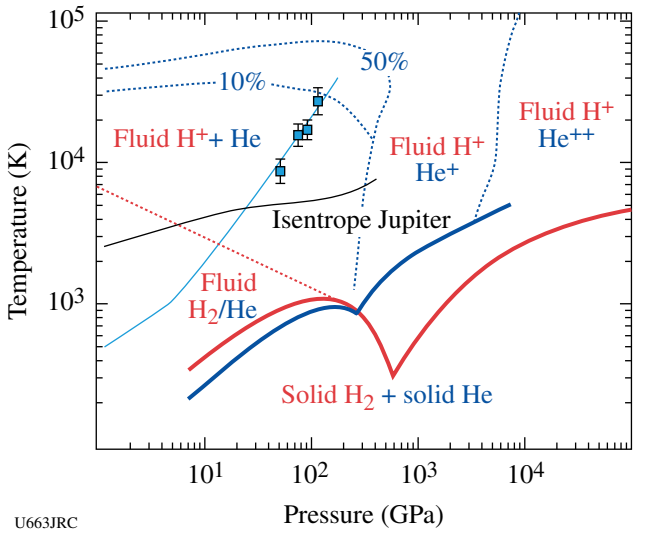

Figure 112.43
Temperature versus pressure for He/H_2. These are the first high-temperature, high-pressure data collected for this mixture that provide key information on the properties of the H_2–He mixtures dominating giant planetary interiors.

These data suggest that over the warm, dense matter states tested here, which are relevant to the outer 20% of Jupiter, the mixture does not phase separate. This is an important result, providing new constraints on models of the interior structure and evolution of giant planets. It warrants further analysis, both to refine our understanding of the experimental observations and to fully understand the implications for the evolution, therefore formation, of planets.

In summary, we completed 23 experiments in two shot days, filling out our database for H_2, He, and one mixture of He/H_2. We have characterized key properties of dense planetary fluids and have documented an interesting isotope effect in the compressibility of H_2 relative to D_2. Helium becomes electronically conducting at ~1 Mbar and 1 eV, largely by a thermally activated process. The He/H_2 mixture seems to behave like an ideal solution up to ~1 Mbar and 2 eV. Several papers are published or are in the process of publication,[1–3,6–9] and this work has ignited an explosion of papers on He, H_2, and mixtures at planetary-core conditions.

Experimental Astrophysics on the OMEGA Laser

Principal Investigator: R. P. Drake (University of Michigan)
Co-investigators: D. Arnett (University of Arizona); T. Plewa (Florida State University); A. Calder, J. Glimm, Y. Zhang, and D. Swesty (SUNY Stony Brook); M. Koenig (LULI, Ecole Polytechnique, France); C. Michaut (Observatorie de Paris, France); M. Busquet (France); J. P. Knauer and T. R. Boehly (LLE); P. Ricker (University of Illinois); B. A. Remington, H. F. Robey, J. F. Hansen, A. R. Miles, R. F. Heeter, D. H. Froula, M. J. Edwards, and S. H. Glenzer (LLNL)

The OMEGA laser is able to produce processes similar to those that occur in astrophysics because it can generate extremely high energy densities, corresponding to pressures greater than 10 Mbar in millimeter-scale targets. This project is focused on two such issues in astrophysics: the contribution of hydrodynamic instabilities to the structure in supernovae and the dynamics of radiative shock waves. To explore hydrodynamic instabilities in supernovae, it was necessary to develop new radiographic diagnostics capable of improved imaging in two orthogonal directions. We have accomplished this goal and are proceeding to study the contributions of various initial modes to the enhanced spike penetration.

In the experiment, ten OMEGA laser beams irradiate a plastic disk with UV light for 1 ns. The total energy of the beams is ~5 kJ and the average irradiance is ~9.5×10^{14} W/cm^2, producing an ablation pressure of ~50 Mbar in the plastic layer

of the target. This large pressure creates a strong shock in the plastic material, which evolves into a blast wave. The blast wave crosses a perturbed interface into a lower-density material. This process is similar to what occurs in a supernova explosion. In the experiment, we monitor the unstable evolution of the interface between the two materials using x-ray radiography.

Figure 112.44 shows data from the latest experiments to obtain physics data using simultaneous, orthogonal, point-projection backlighting. The data are obtained by using a brief (1-ns) x-ray source to project a signal onto an exposed piece of x-ray film. This experiment was imaged 21 ns after the initial laser beams had been pulsed. One can see on these images the structures that have evolved from an initial condition defined by $a_0\sin(kx)\sin(ky)$, where $a_0 = 2.5\ \mu$m and $k_x = k_y = 2\pi/(71\ \mu\text{m})$. Image (a) shows mass extensions that extend from the primary spike toward the shock. This phenomenon has not been previously observed. We have also studied the impact of a selected range of initial conditions. In the next year we plan to do an experiment that will investigate initial conditions more realistic to an actual supernova.

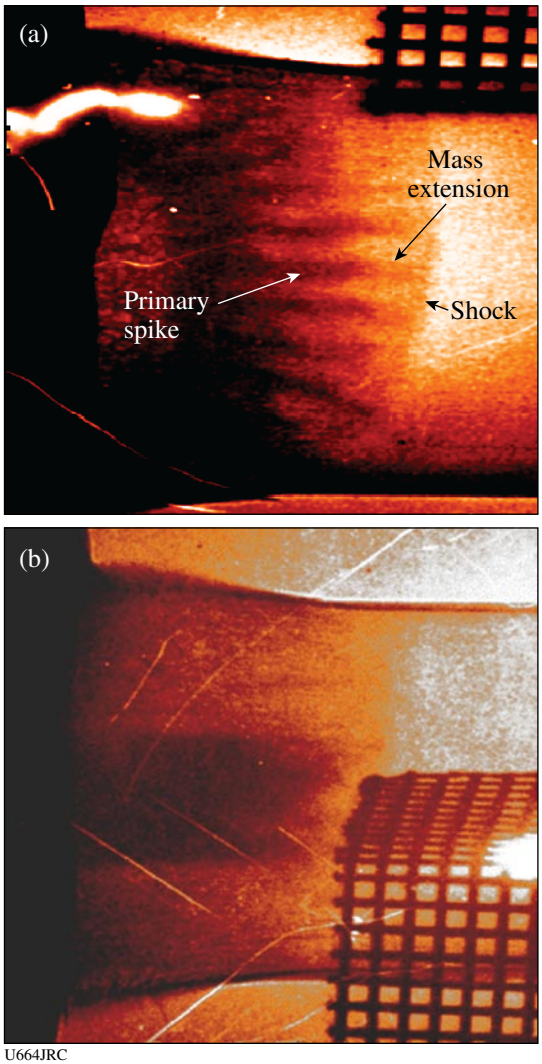

U664JRC

Figure 112.44
Simultaneous, orthogonal, point-projection x-ray backlighting images (a) and (b) of blast wave propagation in plastic material.

Laboratory Experiments on Supersonic Astrophysical Flows Interacting with Clumpy Environments

Principal Investigator: P. Hartigan (Rice University)
Co-investigators: R. Carver (Rice University); A. Frank (University of Rochester); P. A. Rosen, J. M. Foster, and R. Williams (AWE, UK); B. H. Wilde and R. Coker (LANL); B. E. Blue (LLNL)

Supersonic directed jets and outflows are important components of many astrophysical systems. Their interaction with surrounding matter results in the creation of spectacular bow shocks and the entrainment of dense clumps of interstellar material; it may also result in significant deflection of the collimated jet. The objective of this sequence of NLUF experiments is to develop a laboratory platform to study the hydrodynamics of these processes; the laboratory work is complementary to astrophysical observations using the Hubble Space Telescope (HST) and the Kitt Peak National Observatory (KPNO); furthermore, the same computer codes will be used to interpret both the laboratory and astrophysical observations.

In previous experiments on OMEGA, we have developed an experimental platform to create a dense, supersonic, titanium-plasma jet propagating through low-density foam,[10] and we have studied the deflection of this jet by a localized density perturbation.[11] During the past year, two shot days were allocated to this project: we investigated structure potentially seeded in the jet by granularity of the foam medium used in the OMEGA experiments (no significant effect was found), and we progressed further into our project by beginning our study of the interaction of a strong shock with a spherical density discontinuity in the foam. Excellent experimental data were obtained (Fig. 112.45), thereby laying the foundation for further work to study the interaction of shocks and jets with multiple clumps of material—phenomena also being observed in ongoing work using HST and KPNO. The OMEGA experiments were an important component of the case for these further astronomical observations, and our aim is to build a synergistic relationship between experiments, observation, and modeling that will provide new insight into these complex phenomena.

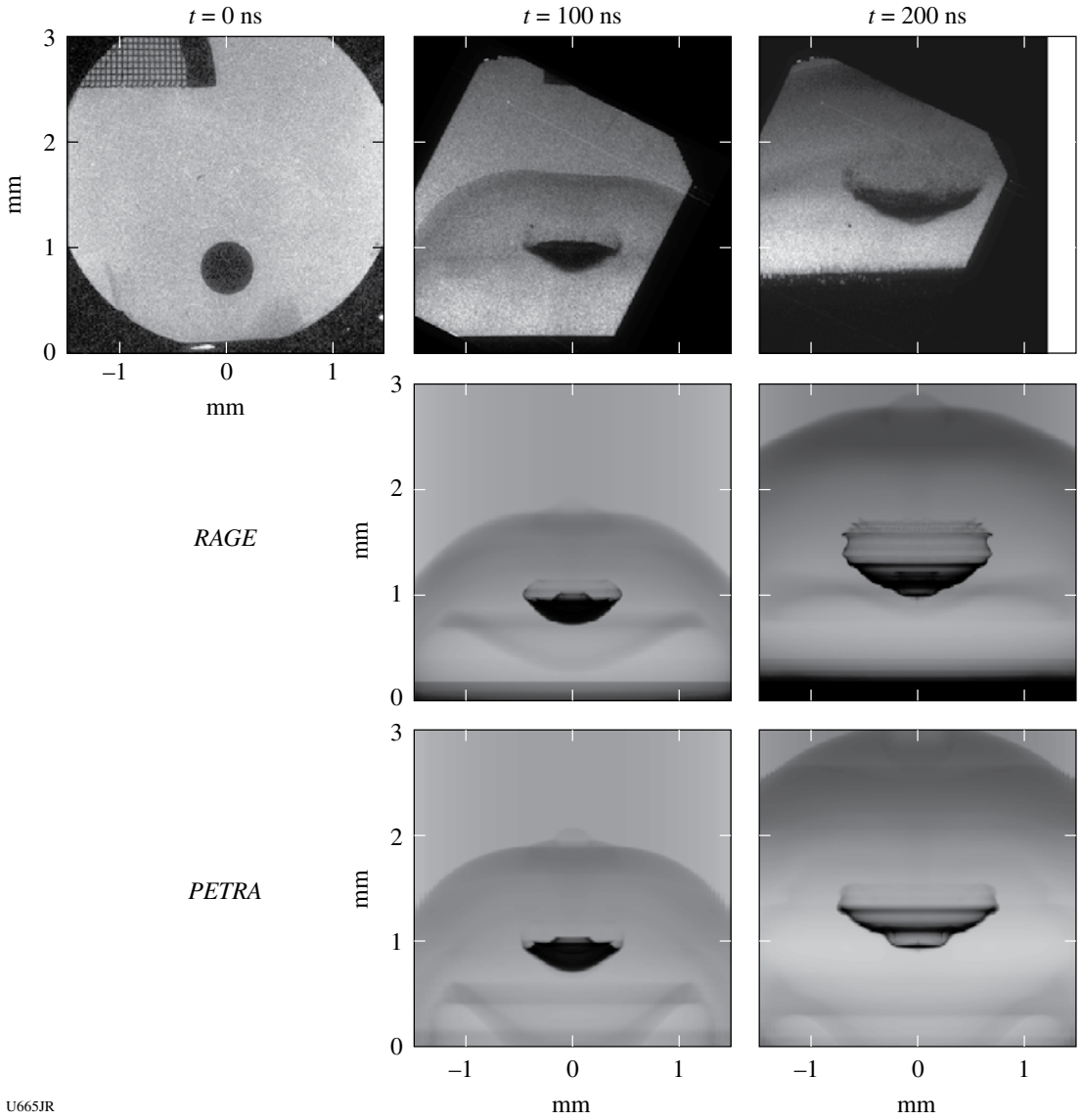

Figure 112.45
Interaction of a strong shock with a density "clump." The OMEGA laser drives a shock through hydrocarbon foam containing a 500-μm-diam sapphire sphere. The sequence of experimental images (top) at 0, 100, and 200 ns shows the shock-driven distortion and entrainment of the sphere by the hydrodynamic flow. The data are compared with modeling (center and bottom) using the *RAGE* and *PETRA* hydrocodes. These phenomena are analogous to those observed in Hubble Space Telescope images of astrophysical jets propagating through interstellar matter.

Multiview Tomographic Study of OMEGA Direct-Drive-Implosion Experiments

Principal Investigator: R. Mancini (University of Nevada, Reno)
Co-investigators: R. Tommasini, N. Izumi, and J. A. Koch (LLNL); I. E. Golovkin (PRISM); D. A. Haynes and G. A. Kyrala (LANL); J. A. Delettrez, S. P. Regan, and V. A. Smalyuk (LLE)

The determination of the spatial structure of inertial confinement fusion implosion cores is an important problem of high-energy-density physics. To this end, three identical multimonochromatic imagers (MMI's) have been designed, built, and fielded in OMEGA implosion experiments to perform observations along three quasi-orthogonal lines of sight (LOS). The implosions were driven with 60 OMEGA beams—23 kJ of UV energy in a 1-ns-duration square laser pulse; the targets were gas-filled plastic shells. At the collapse of the implosion, the hot, dense core plasma achieved temperatures in the 1- to 2-keV range and electron number densities between 1×10^{24} cm^{-3} and $2 \times$

10^{24} cm^{-3}. X-ray K-shell line emission from the argon dopant added to the fuel is a suitable spectroscopy diagnostic for this temperature and density range. In addition, x-ray absorption from a titanium tracer layer embedded in the plastic yields information about the state of the compressed shell.

Core images recorded by MMI instruments are formed by a large array of 10-μm-diam pinholes with an ~100-μm separation between pinholes and are reflected off a depth-graded WB_4C multilayer mirror with an average bilayer thickness of 15 Å. The instrument is equipped with 10-cm-long mirrors that permit the observation of narrowband x-ray images over a photon energy range from 3 to 5 keV. They have a magnification of 8.5, provide spatial resolution of approximately 10 μm, and record gated (framed) images characteristic of a 50-ps time interval. The broad photon energy range, afforded by the use of long mirrors, covers the K-shell line emission from argon ions as well as the K-shell line absorption from titanium L-shell ions. As an illustration of the data recorded by MMI's, Fig. 112.46 displays a time history (i.e., three frames) of narrowband x-ray core images from OMEGA shot 47485 recorded along one LOS at the collapse of the implosion; also shown are examples of narrowband image reconstruction from the data for several spectral features. The data effectively resolve time, space, and photon energy and show several argon line emissions, namely Ly$_\alpha$ ($1s\ ^2S$–$2p\ ^2P$, $h\nu$ = 3320 eV), He$_\alpha$ ($1s^2\ ^1S$–$1s2p\ ^1P$, $h\nu$ = 3140 eV), Ly$_\beta$ ($1s\ ^2S$–$3p\ ^2P$, $h\nu$ = 3936 eV), and He$_\beta$ ($1s^2\ ^1S$–$1s3p\ ^1P$, $h\nu$ = 3684 eV). The photon energy range of these images is given by the (mainly) Stark-broadening widths of the line shapes, which is 60 eV to 70 eV for the plasma conditions achieved in these cores. Core dimensions are in the 60- to 120-μm range. In addition, x-ray absorption in the shell due to titanium ions is also observed. These absorption features are formed by line transitions from n = 1 to n = 2 in L-shell titanium ions (e.g., F-like, O-like, etc.) in the photon energy range from 4500 to 4750 eV driven by continuum radiation emitted in the core, and their analysis permits the characterization of the compressed shell. It is interesting to observe the differences in distribution of brightness associated with the line-based core images, which depends on both temperature and density conditions in the core. Detailed spectral modeling and analysis of the emissivity and opacity of the argon x-ray

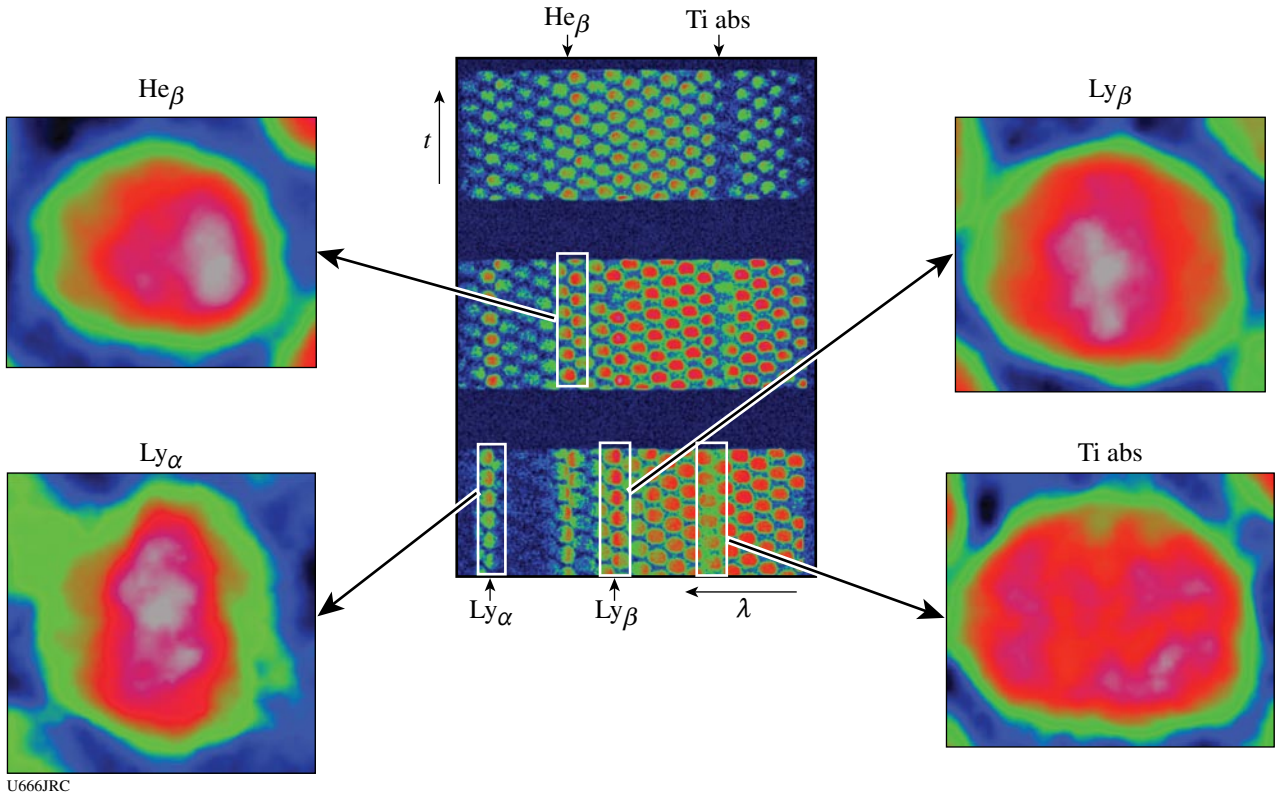

Figure 112.46
Time history (three center frames) of narrowband, x-ray core images recorded by MMI's and four narrowband image reconstructions from this data (OMEGA shot 47485).

emission permit a reconstruction of the spatial structure of the core plasma. Several analysis methods are currently being investigated that simultaneously consider data observed along several lines of sight.

Monoenergetic Proton Radiography of Laser–Plasma-Generated Fields and ICF Implosions

Principal Investigators: R. D. Petrasso and C. K. Li (Massachusetts Institute of Technology)

Co-investigators: J. A. Frenje and F. H. Séguin (MIT); J. P. Knauer and V. A. Smalyuk (LLE); R. P. J. Town (LLNL)

MIT's NLUF program has continued an ongoing series of experiments using monoenergetic charged-particle radiography to study transient electromagnetic fields generated by the interaction of OMEGA laser beams with plastic foils. This work, involving novel studies of time evolution, field instabilities, and magnetic reconnection, has resulted in the publication of three Physical Review Letters publications[12–14] and two invited talks at conferences.[15,16]

Figure 112.47 shows the basic experimental setup.[17] One or more OMEGA laser beams interact with a plastic foil, generating plasma bubbles, **B** fields, and **E** fields. A special backlighter and matched imaging detector are used to create a radiographic image of the resultant plasma/field structure. The backlighter is a glass-shell ICF capsule filled with D^3He gas and imploded by 20 OMEGA laser beams, producing D^3He protons (14.7 MeV), DD protons (3 MeV), D^3He alpha particles (3.6 MeV), and a few other fusion products. CR-39 nuclear track detectors are used in conjunction with appropriate filters and processing techniques to record individual charged particles and their energies in the detector plane. Since the burn duration of the D^3He implosion is short (~130 ps) relative to the nanosecond-scale duration of the foil illumination and subsequent evolution, and since the relative timing of the backlighter and the foil illumination was adjustable, it is possible to record images at different times relative to the foil illumination. A metal mesh is interposed between the backlighter and the foil to divide the incident particle flux into beamlets; distortion in the mesh pattern at the detector shows how the particle trajectories were deflected by the fields generated by laser–plasma interactions at the foil.

In one series of experiments (Fig. 112.48), field evolution and instabilities were studied with 14.7-MeV proton radiography when a single interaction beam was used. While the 1-ns interaction beam was on, the plasma bubble and its surrounding megagauss **B** field expanded symmetrically and roughly linearly, but then became increasingly asymmetric as expansion continued and field strength decayed. We believe this is the first direct observation and evidence of the pressure-driven, resistive-interchange instability in laser-produced high-energy-

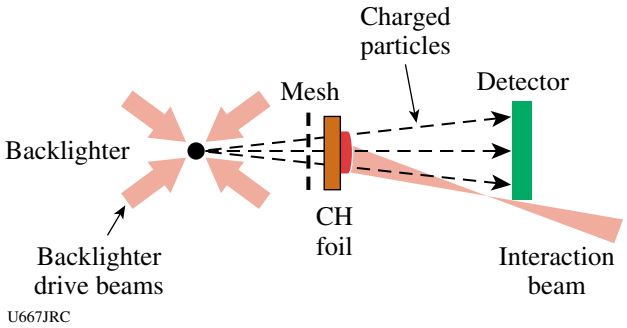

Figure 112.47
Schematic illustration of the experiment setup and the physical relationship between the proton backlighter (imploded D^3He-filled capsule), mesh, CH foil, CR-39 imaging detector, and OMEGA laser beams. Distances of the components from the backlighter were 0.8 cm for mesh, 1 cm for foil, and 30 cm for detector. The hole-to-hole spacing in the mesh was 150 μm.

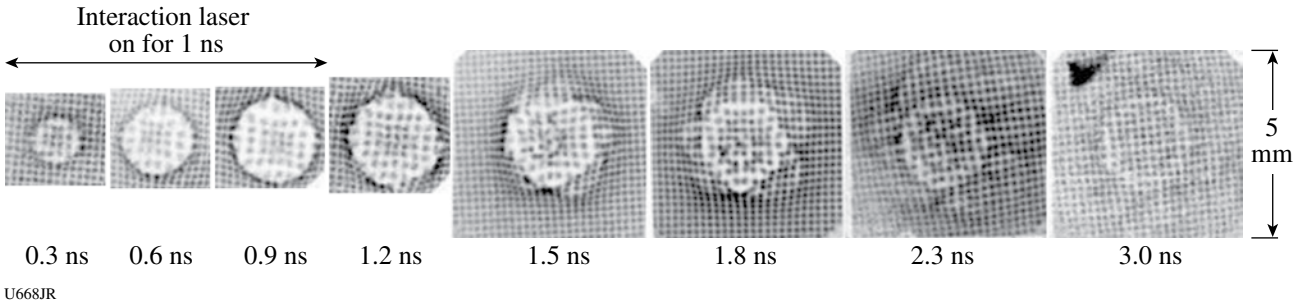

Figure 112.48
Radiographs showing the spatial structure and temporal evolution of the **B** fields generated by laser–plasma interactions. Each image, made with 14.7-MeV protons, is labeled by the time interval between the arrival at the foil of the interaction beam and the arrival of the imaging protons, and each image corresponds to an area about 5 mm by 5 mm at the foil. Note that the laser pulse lasted only 1 ns.

density plasmas. Details and quantitative analysis are given in Ref. 13. In a second series of experiments utilizing 14.7-MeV-proton radiography, multiple laser interaction beams were used simultaneously and resulted in the first direct observation of field reconnection in the high-energy-density regime. Figure 112.49 shows plasma bubbles resulting from two interaction lasers at a time when the bubbles have expanded just enough to contact each other. Quantitative field maps derived from the radiographs revealed precisely and directly, for the first time, the changes in magnetic topology that resulted from reconnection. Details may be found in Ref. 14.

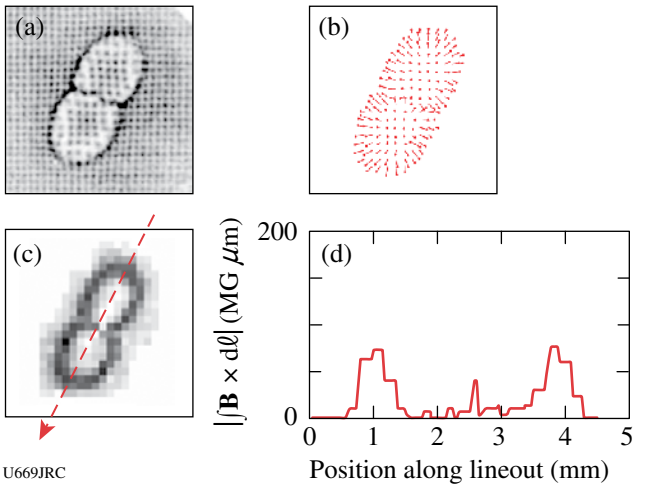

Figure 112.49
A monoenergetic proton radiograph of two plasma bubbles generated in a foil by two interaction lasers was used to deduce a map of the **B** field at the foil. In (a), the location of each beamlet can be compared with the location it would have had with no **B** fields (beamlets on the image edges define the grid of "undeflected" locations); (b) shows displacement vectors. The displacement amplitudes are shown as an image in (c), where each pixel represents one beamlet, with value proportional to displacement. Displacement is proportional to $\int \mathbf{B} \times d\ell$ along the particle trajectory, so the lineout along the arrow in (c) provides quantitative measurements of $\left|\int \mathbf{B} \times d\ell\right|$ at the foil location (d), showing the loss of field energy where the bubbles collided and magnetic reconnection occurred (at about 2.5 mm on the horizontal axis).

X-Ray Compton Scattering on Compressed Matter

Principal Investigators: R. Falcone and H. J. Lee (University of California), P. Neumayer, O. L. Landen, and S. H. Glenzer (LLNL)

These experiments are aimed to measure exact electron density (n_e), temperature (T_e), and ionization (Z) of dense matter with the development of the Compton-scattering technique on the OMEGA Laser Facility. Since an x-ray source can propagate through the critical electron density ~10^{22} cm^{-3}, x-ray Compton scattering has been the most useful diagnostic of local plasma conditions of dense matter with solid density and above. The Compton-scattering cross-section diagnostic is related to the dynamic structure factor $S(k,\omega)$, which presents the Fourier transform of total electron-density fluctuation. It has been understood by decomposing total density distribution: the sum of the motion of electrons and the motion of ions.

Two types of a planar Be target coupled with a Mn backlighter are designed for the x-ray Compton-scattering technique with 90° and 25° scattering angles at the OMEGA Laser Facility. The target consists of a 250-μm-thick Be, 50-μm-thick plastic substrate coated with 3 μm of Mn, 50 μm of Ta with a slot window, and two Au/Fe shields, as shown Fig. 112.50(a). Eleven heater beams of 4-ns flat pulse, $I_{av} \sim 2 \times 10^{14}$ W/cm^2 at 531 nm, are focused symmetrically onto solid Be with an

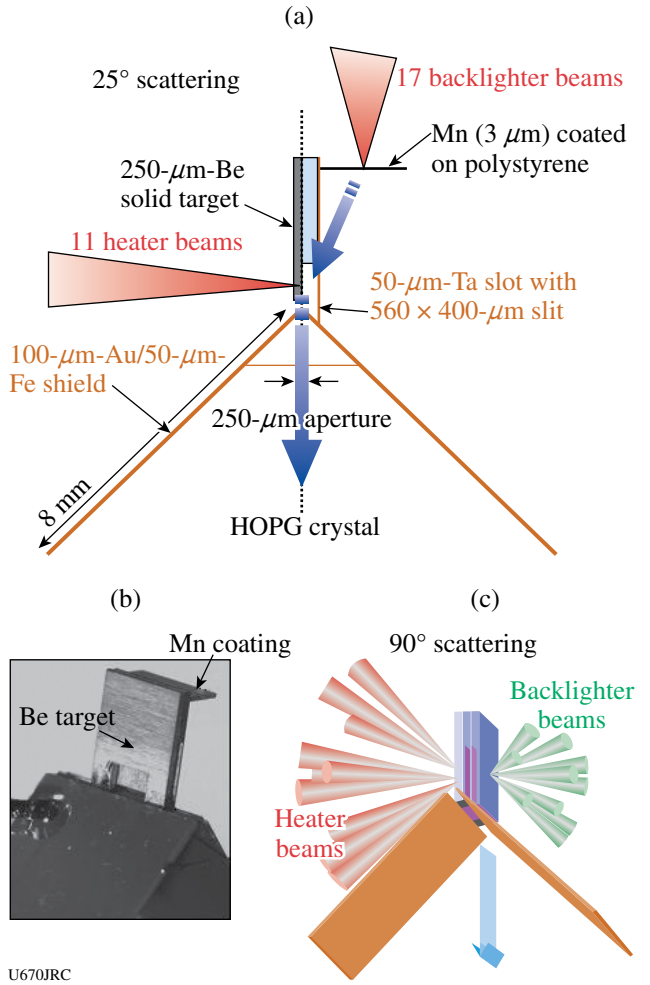

Figure 112.50
(a) Schematic of the target details for 25° scattering; (b) a real image of the target; (c) target schematic for 90° scattering.

~800-μm spot. To create ~6.18-keV Mn He$_\alpha$ x-ray photons, we applied 12 backlighter beams to Mn-coated plastic for 25° scattering (17 backlighter beams for 90° scattering) with a focal spot of 200 μm. Figures 112.50(b) and 112.50(c) present a photograph of 25° scattering target and an image for 90° scattering target that has a Mn backlighter parallel to Be. A highly oriented pyrolytic graphite (HOPG) crystal coupled to an x-ray framing camera with 500-ps gating time in TIM-3 has been used as a spectrometer and a detector.

Figures 112.51(a) and 112.51(b) show scattering spectra (black lines) and fits (thick white lines) to the data of 90° and 25° scattering geometries. In the noncollective scattering regime of 90°, the spectrum shows Compton downshifted peaks in addition to the elastic-scattering peaks at E_{01} = 6.18-keV Mn He$_\alpha$ and E_{02} = 6.15-keV intercombination x-ray lines. With the broadening by the thermal motion of electrons, the intensity and shape of Compton peaks are sensitive to T_e and n_e. For the analysis, we calculated $S(k,\omega)$ theoretical x-ray scattering spectra using the random phase approximation. The calculated spectrum with $n_e = 7.5 \times 10^{23}$ cm^{-3}, T_e = 13 eV, and $Z = 2$ for a Fermi temperature of E_F = 30 eV gives a best fitting to the data. The 25° forward scattering independently provides a unique data set on the n_e and T_e of compressed matter. In the collective scattering regime, the probing wavelength is larger than the Debye screening length and the scattered spectrum is dominated by plasmon resonance, which is associated with electron plasma-wave resonance. The measured spectra of Fig. 112.51(b) show downshifted plasmon peaks; the position of the peak is very sensitive to n_e. The thick white line presents a best fitting to the data. The n_e and T_e measured from the plasmon peak show very good agreement with the parameters obtained from the backscattering spectra as well as from the hydrodynamic calculation on compressed Be plasmas.

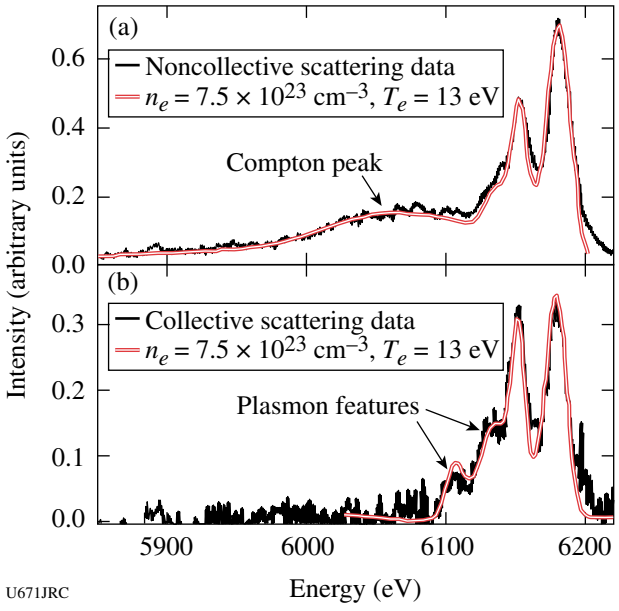

Figure 112.51
Experimental scattering data (black line) and fitting results (thick white line) of (a) 90° scattering geometry and (b) 25° scattering geometry.

Through this project, we successively measured the Compton and plasmon resonance on shock-compressed Be. With the comparison to the theoretical calculation, we find that compressed plasmas of $n_e = 7.5 \times 10^{23}$ cm^{-3}, T_e = 13 eV, and $Z = 2$ within ~15% error bars could be reached under the pressure in the range of 20 to 30 Mbar. From these experiments, we have proved that the x-ray Compton-scattering technique is a precise experimental tool for determining the exact densities and temperatures in compressed matter and characterized compressed states of matter.

FY07 LLNL OMEGA Experimental Programs

In FY07 Lawrence Livermore National Laboratory (LLNL) led 404 target shots on the OMEGA Laser System. This total represents a shot rate approximately 8% higher than nominal (373 shots scheduled for the year). This is an improvement over last year's operations (4% above nominal) and is especially noteworthy considering that programmatic needs frequently require complex configuration changes both overnight and mid-day.

National Ignition Campaign (NIC) Experiments: About 57% of the LLNL shots were dedicated to advancing the National Ignition Campaign in preparation for future experiments at the National Ignition Facility (NIF). This represents a slight percentage decrease from the prior year, as effort transitions to the NIF itself. Campaigns on OMEGA had many objectives, including studies of the laser–plasma interaction (LPI) physics in physical conditions relevant for the NIF ignition targets, improving the diagnostic suite for ignition, and studying dense-plasma physics via collective x-ray scattering; however, this year there was a special emphasis on assessing the physical characteristics of proposed ignition capsule materials.

A variety of LPI experiments were conducted in FY07, some in collaboration with CEA, typically using gas-filled hohlraums arranged so that one OMEGA beam (beam 30) could be used as an on-axis probe beam.

In work now submitted for publication, experiments demonstrated a significant reduction of stimulated Brillouin scattering (SBS) by polarization smoothing in conditions (T_e ~

3 keV) with no ponderomotive and thermal filamentation (see Fig. 112.52). Measurements showed that adding polarization smoothing increases the intensity threshold for SBS by a factor of 1.7. For intensities less than 2×10^{15} W/cm^2, more than an order of magnitude reduction in the backscattered power is observed. This reduction in backscatter was shown to increase the total transmission through a plasma for conditions that are comparable to those in current ICF target designs. A simple model relevant to ICF plasma conditions is able to explain a direct effect on the SBS gain exponent and, consequently, the threshold for when SBS becomes energetically important.

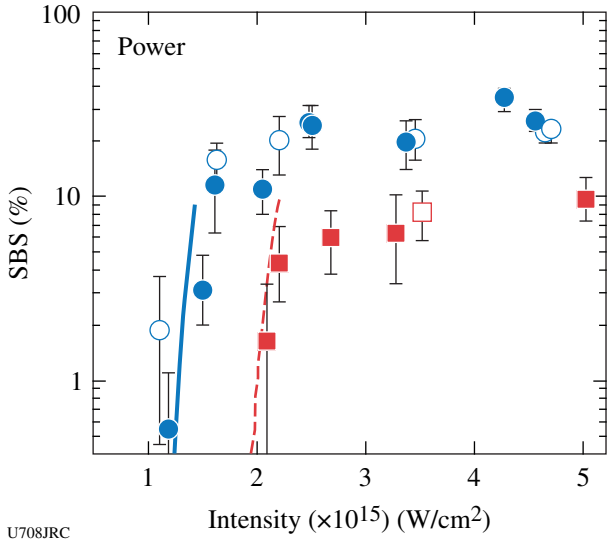

Figure 112.52
The measured instantaneous SBS reflectivity at t = 700 ps is plotted as a function of the interaction beam intensity; three laser-smoothing conditions are shown: continuous phase plates (CPP's, circles), CPP's plus polarization smoothing (squares), and with 3-Å SSD (open symbols). The calculated reflectivities using an analytical model reproduce the measured thresholds and a factor-of-1.7 reduction in the SBS threshold when polarization smoothing is applied to a CPP-smoothed laser beam. An analytical model that calculates the thresholds is shown for the CPP only (solid curve) and when polarization smoothing is applied (dashed curve).

Another experimental result now submitted for publication, and detailed in Fig. 112.53, extends the limits of plasma length in inertial fusion laser–plasma interaction experiments. Laser-beam propagation and low backscatter were demonstrated in laser-produced hohlraum plasmas of ignition plasma length. At intensities $<5 \times 10^{14}$ W/cm^2, greater than 80% of the energy in a blue (351-nm) laser is transmitted through an L = 5-mm-long, high-temperature (T_e = 2.5 keV), high-density ($n_e = 5 \times 10^{20}$ cm^{-3}) plasma. For an intensity of $I = 6 \times 10^{14}$ W/cm^2, these experiments also show that the backscatter scales exponentially with plasma length, from <0.05% at a 1.3-mm length to >10%

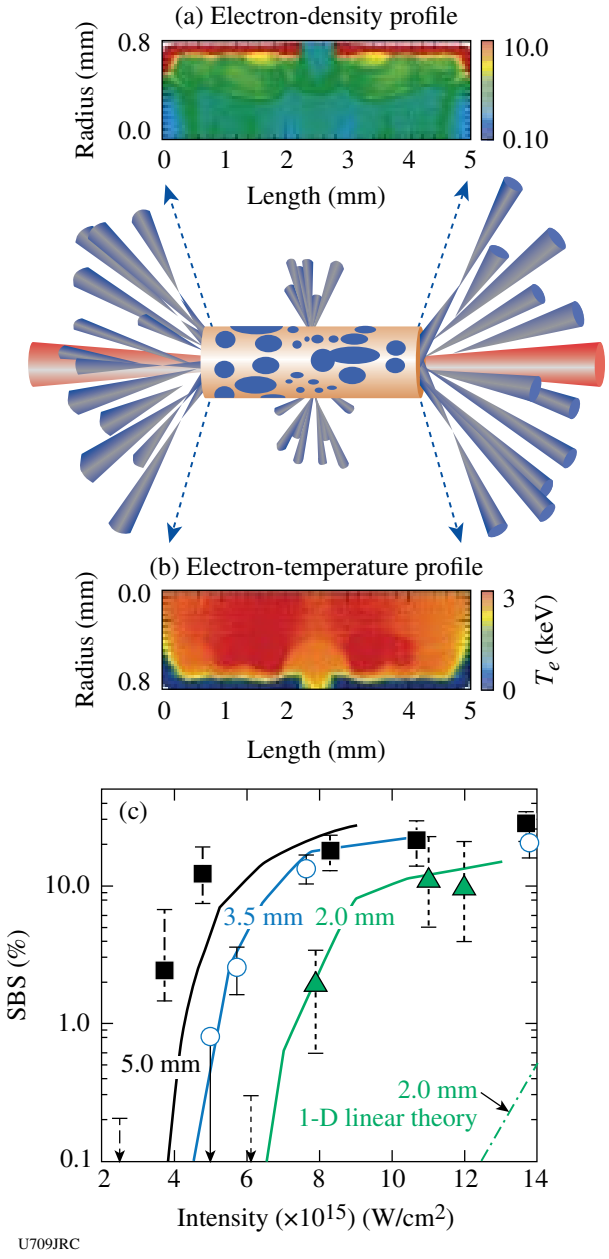

Figure 112.53
(a) Simulated electron-density and electron-temperature profiles for a 5-mm-long LPI hohlraum at peak electron temperature (900 ps after the heater beams turn on). Three LEH's are equally spaced around the hohlraum equator to allow the addition of 17 laser beams. In total, 53 laser beams irradiate the hohlraum wall, producing electron temperature T_e along the axis in excess of 2.5 keV. The interaction beam is aligned along the axis of the hohlraum, interacting with a uniform 5×10^{20} cm^{-3} plasma plateau. (b) The measured instantaneous SBS reflectivity is plotted as a function of vacuum intensity for the three target lengths: 2 mm (triangles), 3.5 mm (circles), and 5 mm (squares). The solid curves are simulations performed by SLIP. For reference, a line is shown (dashed–dotted) calculated using linear theory for the 2-mm-long targets where a gain of $\Gamma_s \beta_s = 11$, for an intensity of 1×10^{15} W/cm^2, is determined by post processing the hydrodynamic parameters.

at a 4.0-mm length. This result is consistent with linear theory. The backscatter calculated by a new steady-state, 3-D laser–plasma interaction code (SLIP) developed for large ignition plasmas is in good agreement with the measurements. These results span the gap between previous studies ($L < 2$ mm, $T_e = 2.5$ keV) and future ignition hohlraum plasmas ($L = 5$ mm, $T_e > 3$ keV) and indicate that backscatter can be controlled at ignition plasma conditions and intensities.

Additional laser–plasma interaction experiments on the high-electron-temperature gas-filled hohlraum target platform demonstrated the effectiveness of Landau damping in multiple-ion species plasmas to reduce backscatter. By adding hydrogen to a CO_2 gas fill, the SBS reflected power was suppressed from >30% to ~1%, while SRS was below the detection threshold (Fig. 112.54). Improved heater beam coupling into the hohlraum by suppression of the total backscatter resulted in an increase in measured hohlraum radiation temperature. As a result of these findings, a multiple-ion-species gas fill is now included in the NIC hohlraum point design.

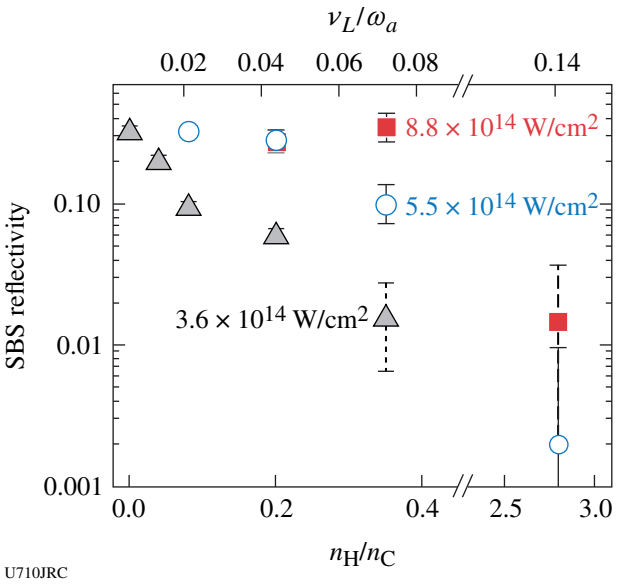

Figure 112.54
The SBS reflectivity is reduced from >30% to ~1% when increasing Landau damping by adding hydrogen to the CO_2 hohlraum gas fill (probe-beam intensities of 3.6, 5.5, and 8.8×10^{14} W/cm^2).

In pursuit of a more precise understanding of hohlraum energetics, and to develop methods for diagnosing possible ignition failure modes, half of an extended day was dedicated to a series of shots designed to study the impact of x-ray flux originating from outside the laser entrance hole (LEH) of a laser-heated hohlraum—measured with the OMEGA Dante diagnostic—on the interpretation of the observed radiation temperature inside the hohlraum. An empty gold hohlraum was heated with 38 beams using a 2.6-ns-long pulse. In addition, two beams were used to illuminate the hohlraum outside of the LEH. One beam had a large spot size, mimicking the effect of LEH closure during the heating; the second beam had a small spot size, providing an indicator of the x-ray emission due to a mispointed heater beam. A soft x-ray imager was used to identify the various sources of x-ray emission, and Fig. 112.55 shows a set of images for three different x-ray regimes, i.e., around 250 eV, 750 eV, and above 2 keV. For this particular shot, the start times of the cone 2 and cone 3 heater beams were tuned to also study the spot formation. The series of shots indicated that without correcting the x-ray flux measured by Dante with respect to its origin, the derived radiation temperature was about 1% higher.

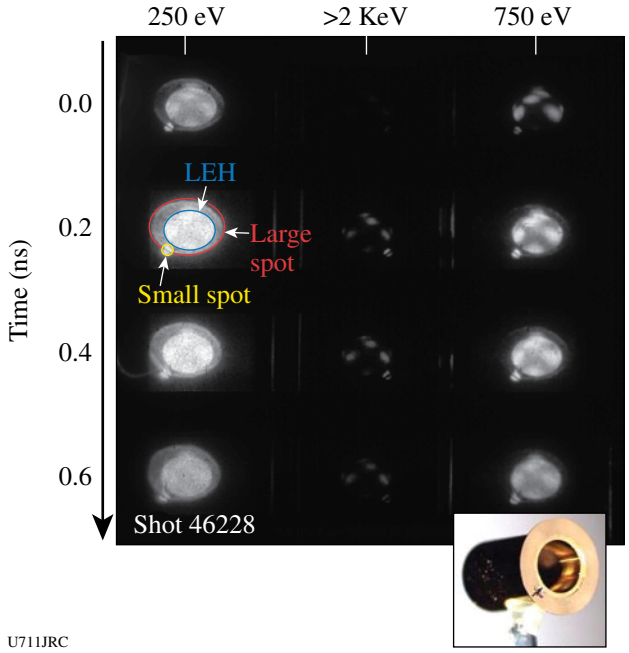

Figure 112.55
Soft x-ray images taken from the laser-heated Au hohlraum, together with a picture of the target. The x-ray images show the emission from the LEH with various spots from the heater beams. Additional x-ray emission originates from a large beam spot and a small beam spot, which hit the gold washer and provide the required emission area outside of the LEH to mimic the "LEH closure" scenario. The washer also contains a spatial fiducial (cross hair).

Progress also continued in characterizing the physical properties of warm, dense matter. Experiments studying x-ray scattering on radiatively heated solid-density beryllium at different scattering angles provided a first direct test of dense matter theories describing ion–ion correlations at long scale lengths in dense matter, as shown in Fig. 112.56.

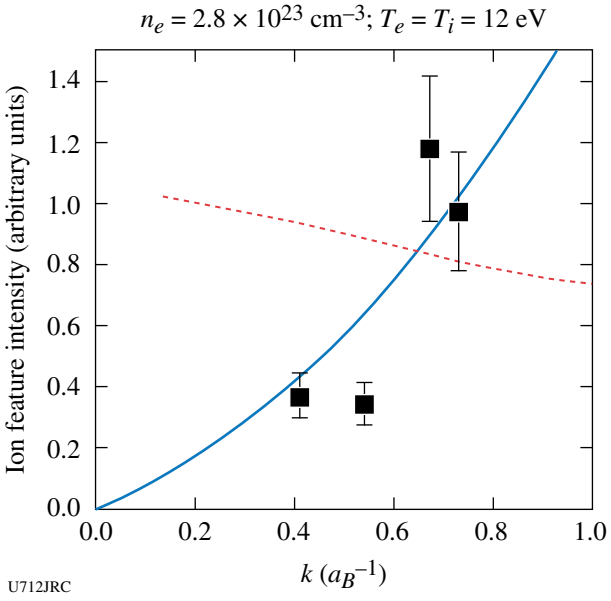

Figure 112.56
Comparison of measured elastic scattering feature with theoretical predictions, showing better agreement with the HNC TCP calculations.

Ignition capsules face challenging physics requirements since they must transmit shocks into the DT ignition fuel without also producing hydrodynamic instabilities that would dilute the fuel with higher-Z ablator material. This translates into requirements for very low surface roughness and specific shock response properties. In FY07, the physical properties of capsules based on copper-doped beryllium and high-density carbon (synthetic diamond) were studied extensively, using new techniques that significantly extend previous work on, e.g., Rayleigh–Taylor growth measurements, imploding-capsule radiography, and velocity interferometry of shocked surfaces.

Simulations predict that residual microstructure and velocity fields in melted Be could still seed some hydrodynamic instabilities upon shock breakout, but at a level below that expected and acceptable from growth of known surface imperfections. To validate these expectations, we have designed OMEGA experiments that amplify their perturbation seeding using high-growth-factor [GF ~ exp($\gamma\tau$)] Rayleigh–Taylor instability drives. To achieve this, an 8- to 10-ns-long drive has been developed [see Fig. 112.57(b)], which for a given achievable radiographic accuracy, ΔGF/GF = $\tau\Delta\gamma$, leads to an improved growth-rate accuracy $\Delta\gamma \sim 1/\tau$. This drive also provides sufficient sensitivity to directly measure, through x-ray radiography, 3-D growth from BeCu planar foils with a level of surface roughness equal to the NIF ignition design surface-roughness tolerance [see Fig. 112.57(c)]. The results—when compared to simulations that ignore possible growth from

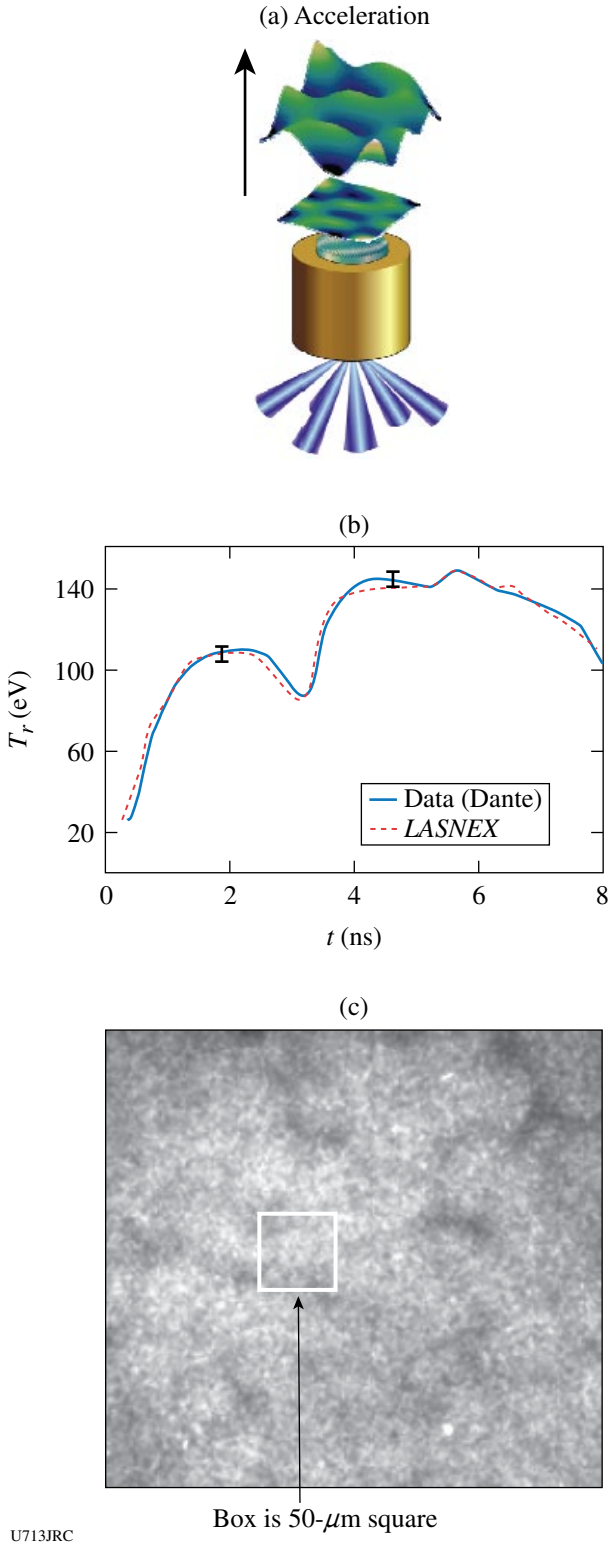

Figure 112.57
(a) Experimental setup for ablation-front Rayleigh–Taylor growth measurement; (b) measured versus calculated x-ray drive T_r; (c) 4.3-keV radiograph of growth of NIF-surface roughness on Be(Cu) foil at 8.2 ns.

Be microstructure and, therefore, consider only growth from surface perturbations—suggest that, at least for ablation-front instability growth, microstructure is not important.

Determining ablator performance during an implosion is a critical part of the NIF tuning campaign. In particular, it is vital to have accurate, time-resoved, in-flight measurements of the velocity, areal density, and mass of the ablator as it converges. In tests on OMEGA we have developed a new technique that achieves time-resolved measurements of all these parameters in a single, area-backlit, streaked radiograph of an indirectly driven capsule. This is accomplished by first extracting the radial density profile at each time step from the measured radiograph; then scalar quantities such as the average position, thickness, areal density, and mass of the ablator are determined by taking integral moments of this density profile. Results from implosions of Cu-doped Be capsules are shown in Fig. 112.58.

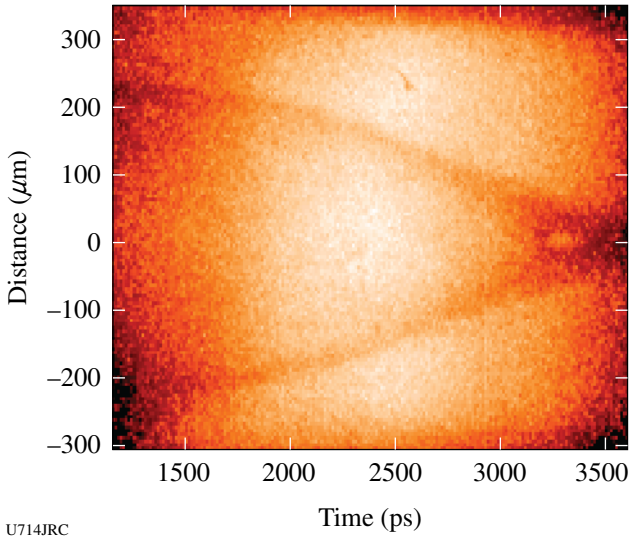

Figure 112.58
Streaked radiograph showing converging capsule leading up to bang time at 3300 ps.

Synthetic diamond is a promising ablator material for ICF capsules because of its low-Z and high density. It is important, however, to know the high-pressure phase diagram of diamond since the tuning design for ICF capsules requires that the first-shock state remain completely solid and the second-shock state be completely melted. Having successfully measured first-shock melting of diamond on OMEGA last year, a new method was developed this year to detect second-shock melting. This involved launching a first shock into diamond between 2 to 4 Mbar, followed by a strong second shock between 15 and 25 Mbar. As shown in Fig. 112.59, by measuring the thermal emission of the second shock through the transparent first shock, it was possible to determine the temperature of the second-shock Hugoniot versus pressure. Evidence of melting was found in the discontinuity in the second-shock Hugoniot above 20 Mbar.

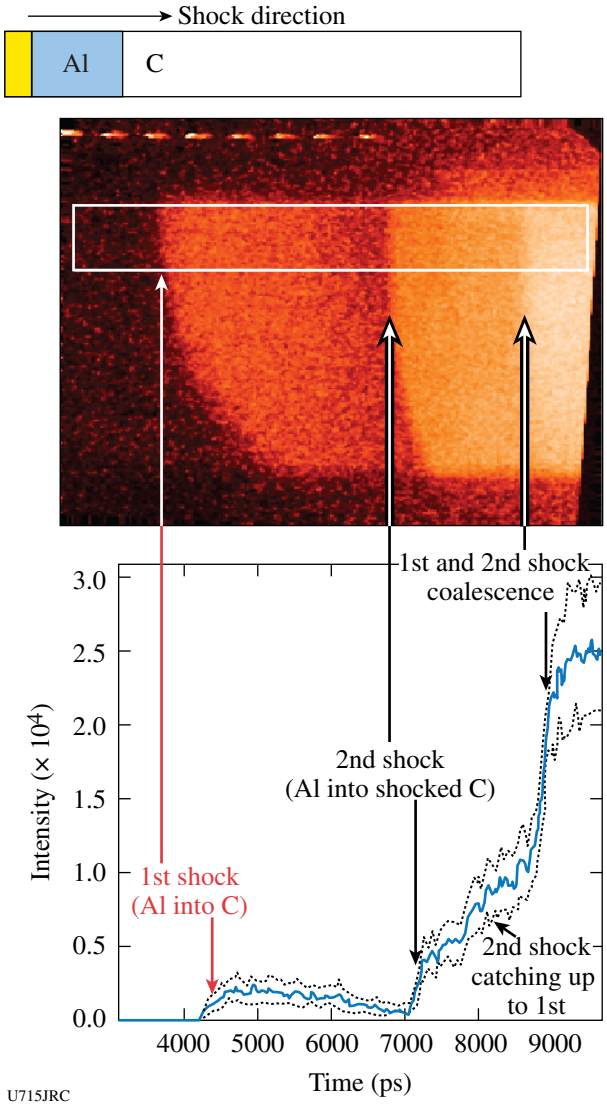

Figure 112.59
Streaked, space-resolved measurement of the thermal emission from a doubly shocked Al/diamond sample.

Determining the level of velocity uniformities created by microscopic perturbations in NIF ablator materials is a challenging measurement task. The measurement diagnostic must detect these nonuniformities at a level of a few parts in 10,000 to be relevant to the NIF requirements. The CAPSEED campaigns were fielded to make these measurements with a

new technique. During FY07 a high-resolution velocity interferometer was fielded on the TIM-6 diagnostic location. The instrument, called the OMEGA High-Resolution Velocimeter (OHRV), is a 2-D space-resolving "velocity interferometer from the surface of any reflector" (VISAR), which probes the velocity distribution across a moving reflecting surface with 2-μm spatial resolution and few-m/s velocity resolution in a single 2-D snapshot. Its main mission is to measure the seed-level nonuniformities in NIF capsule ablator candidate materials and to verify that the seed levels are consistent with current model predictions of capsule performance. Assembly and qualification of the instrument took place during the summer, commissioning in early September, followed by a successful experimental campaign in October (Fig. 112.60). Experiments testing Be(Cu), high-density carbon, and Ge-doped plastic ablators are continuing in FY08.

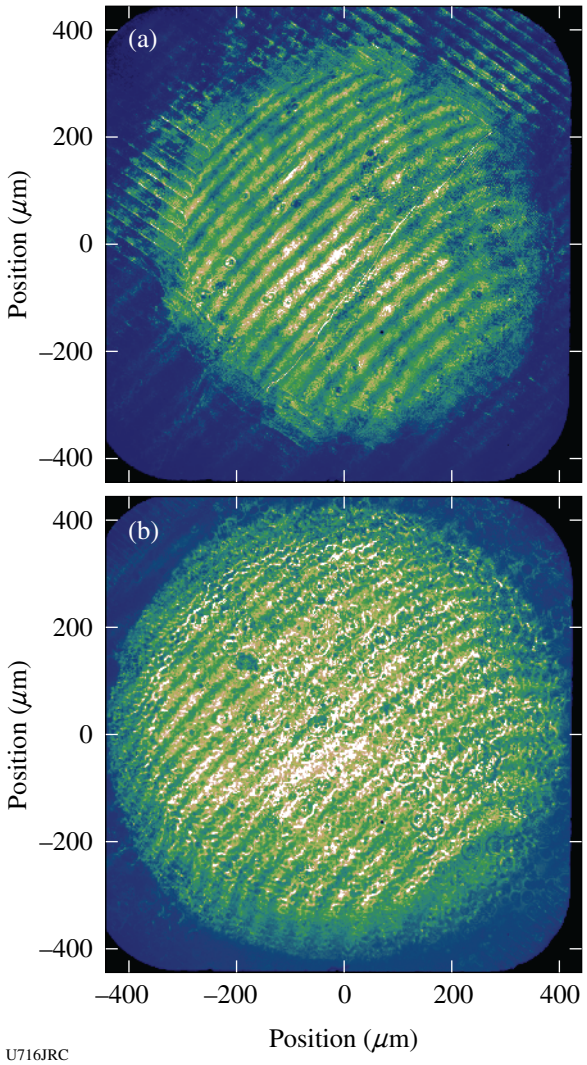

High-Energy-Density Science (HEDS) Experiments: About 43% of the LLNL shots were dedicated to HEDS campaigns, including quasi-isentropic compression experiments (ICE), dynamic hohlraums, opacity measurements of hot plasmas in local thermodynamic equilibrium (LTE), and non-LTE implosion physics. High-temperature hohlraums, long-duration point backlighter sources, and foam-walled hohlraums were also studied to develop HED experimental platforms for future NIF experiments.

LLNL has for some time been developing laser-based experimental platforms that can compress materials quasi-isentropically to very high pressures at ultrahigh strain rates. This laser-driven, ramped (shockless) drive is used to study material properties such as strength, equation of state, phase, and phase-transition kinetics under extreme conditions. In FY07 an effort was launched to develop a platform compatible with NIF, based on ICE drive by indirect x-ray illumination from a hohlraum onto a reservoir/package assembly on the side of the hohlraum at the midplane.

Development of such a hohlraum-driven ICE platform requires an understanding of the hydrodynamics of hohlraum radiation coupling to the ICE pressure, planarity of the pressure drive on the package, hohlraum filling at late times for package radiography, and potential preheat of the reservoir and package by the hohlraum M band.

Initial experiments used the normal OMEGA VISAR (ASBO) system and a tilted target package (since the VISAR does not have a view orthogonal to a standard hohlraum axis). This approach provided helpful information on obtaining VISAR data from hohlraum packages, but it resulted in hard-to-model 3-D effects on the drive and insufficient planarity. A new tilted ASBO telescope was developed that is able to measure packages normal to the hohlraum axis. It has now been tested and fully qualified for the next set of experiments, presently scheduled for January 2008.

Figure 112.60
(a) Two-dimensional interferogram of a shock front emerging from a Be(Cu) ablator sample approximately 200 ps after breakout into a plastic layer (central 600-μm-diam circular region). Bias fringes run from bottom left to top right; a preimposed ripple machined into the Be surface is visible in the edges of the image (periodic pattern oriented perpendicular to the fringes). (b) Velocity interferogram of a shock front emerging from a diamond ablator into a plastic layer, approximately 1 ns after breakout. The high-frequency spatial modulations superimposed on the fringe pattern indicate nonuniformities in the shock front.

A parallel set of experiments studied the hohlraum plasma filling at late times. Hohlraums with and without thin CH liners were probed using a 6.7-keV Fe backlighter. The radiographic data were used to assess the Au filling from the walls at late times (t = 20, 60, and 80 ns after the hohlraum drive); these results agreed well with 2-D simulations. The hohlraum stays open at late times with minimal filling, providing support for future ICE-driven Rayleigh–Taylor radiography experiments at late times on the NIF.

To understand the drive on the reservoir, the radiation temperatures of different types of hohlraums were studied and compared with *LASNEX* 2-D simulations. Figure 112.61 shows the Dante measurements and *LASNEX* simulations from both CH-lined and non-CH-lined hohlraums. The peak radiation temperature data are in good agreement with the simulation, but the simulation shows the radiation temperature remaining higher later in time than the data indicate. This might be caused by the on-axis stagnation effect, which is more pronounced in the symmetric 2-D simulation as opposed to the experiments, which have enough 3-D effects to reduce the axial stagnation. The study of late-time hohlraum energetics is significant for multiple HEDS campaigns and will continue in FY08.

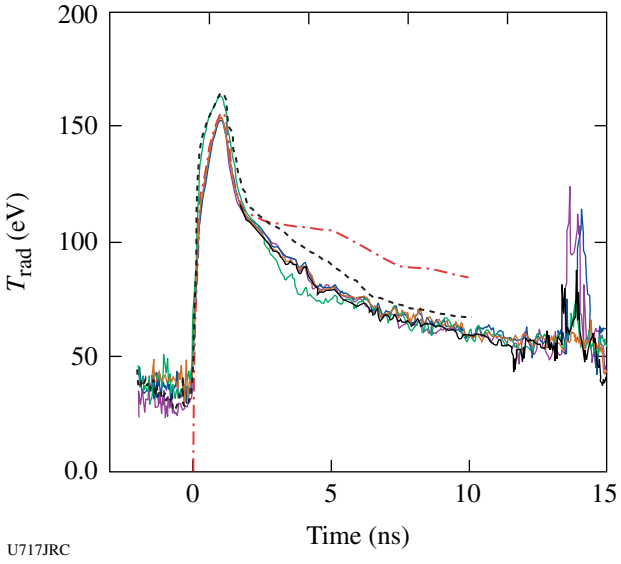

Figure 112.61
Dante radiation-temperature measurements (solid) from scale-1.37 hohlraums driven with 12.5 kJ in a 1-ns square pulse, compared with 2-D *LASNEX* simulations (dashed).

Over the past year, LLNL has continued experiments with laser-driven dynamic hohlraums (LDDH's). These experiments have compared the neutron yield and the areal fuel density produced by "standard" xenon-filled LDDH's (see Fig. 112.62) to those of capsules where the xenon is replaced by neopentane; the latter gas fill replicates the hydrodynamics of a xenon-filled LDDH but does not create the high-Z radiation-trapping cavity (hohlraum), thus making it possible to measure the difference in yield and fuel density due to the hohlraum effect. Analysis of this data is underway. Additional LDDH experiments have explored the robustness of dynamic hohlraums when driven by laser beams in a polar configuration, such as would be necessary on the NIF; the experiment showed that repointing the laser beams along the polar axis can compensate for the nonuniform laser drive.

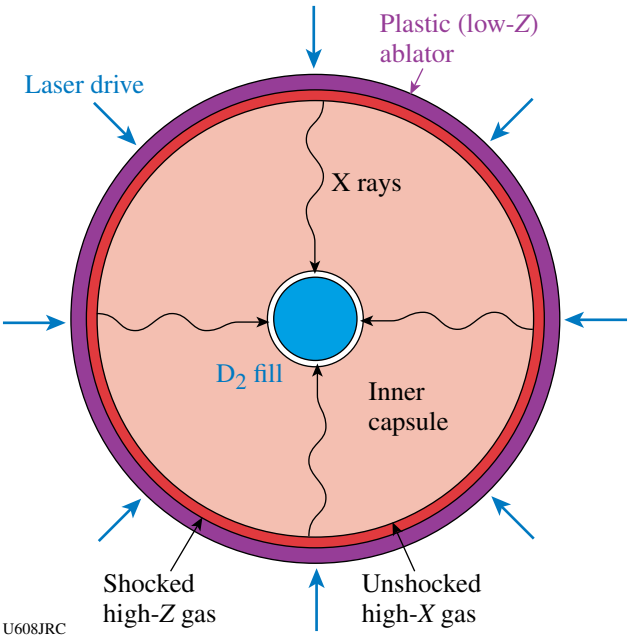

Figure 112.62
Concept of "dynamic hohlraum:" shock-heated Xe gas between shells radiates x rays that ablatively implode inner shell. Data obtained include x-ray-streaked images of the self-emitted x rays, multiple x-ray images, charged-particle information (collaboration with MIT), and multiple standard OMEGA neutron diagnostics.

Prior results having shown that LDDH's emit very bright, spectrally smooth bursts of multi-keV x rays, it was decided to explore whether LDDH's might scale down for use as bright, broadband backlighters suitable for absorption spectroscopy experiments. Early in FY07, a set of small, Kr-filled plastic capsules were imploded using ten polar direct-drive beams and produced bright continuum emission at photon energies up to at least 5.5 keV (Fig. 112.63). These capsules proved bright enough to be used as backlighters for spectroscopic transmission measurements of hot plasmas. Previous continuum x-ray sources either required too many beams (so that the hot plasmas

could not be produced) or did not work at photon energies above ~3500 eV (Ref. 18). In a follow-up experiment, initial data were obtained for $n = 1$ to $n = 2$ absorption of Ti samples at LTE conditions near 100 eV inside hohlraums. LLNL plans to use this new capability to measure the temperatures of high-temperature LTE opacity samples in FY08.

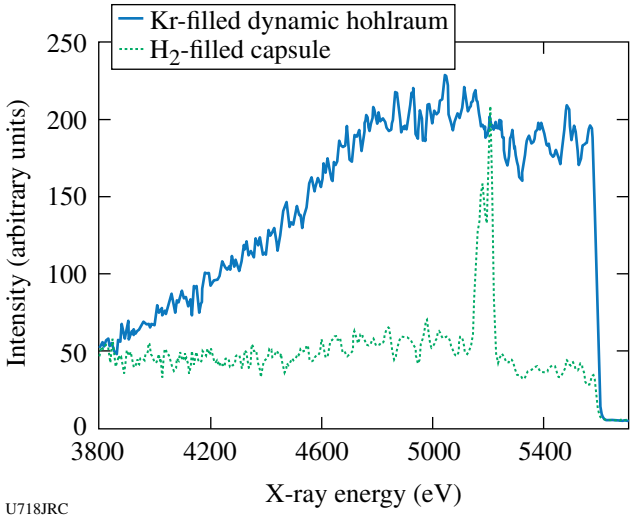

Figure 112.63
Gated spectra produced by an H_2-filled capsule (dotted) and a Kr-filled capsule (solid). Instrument configurations were identical for both shots; Dante data for this band show a factor-of-2 increase in peak x-ray yield. The lines near 5200 eV in the H_2 spectrum are from a vanadium dopant in the shell for that capsule.

The goal of the nonlocal thermodynamic equilibrium (NLTE) campaign is to build a platform to study energy balance in implosions by measuring ion, electron, and radiation temperatures as a function of high-Z dopant concentration. In the FY07 experiments, all 60 beams of the OMEGA Laser Facility were used for direct-drive implosions of thin (4 μm) glass capsules filled with 10 atm of D^3He gas and 0.01 atm of Kr gas as a spectroscopic tracer. We used Xe as the high-Z dopant gas, with concentrations from 0 to 0.06 atm. As a time-resolved electron-temperature (T_e) diagnostic, we fielded a new mica conical crystal spectrometer (Fig. 112.64), which was coupled to a streak camera, and viewed K-shell emission lines from the Kr dopant. Time-integrated spectra were also recorded with the HENEX spectrometer developed by NIST/NRL. The time-resolved spectra show that the addition of Xe reduces T_e proportionally, in agreement with simulations. Time-dependent ion temperatures (T_i), inferred from proton and neutron emission time histories and spectra, also show a reduction in the compression-phase T_i with increasing Xe concentrations. Finally, secondary neutron measurements as well as gated x-ray

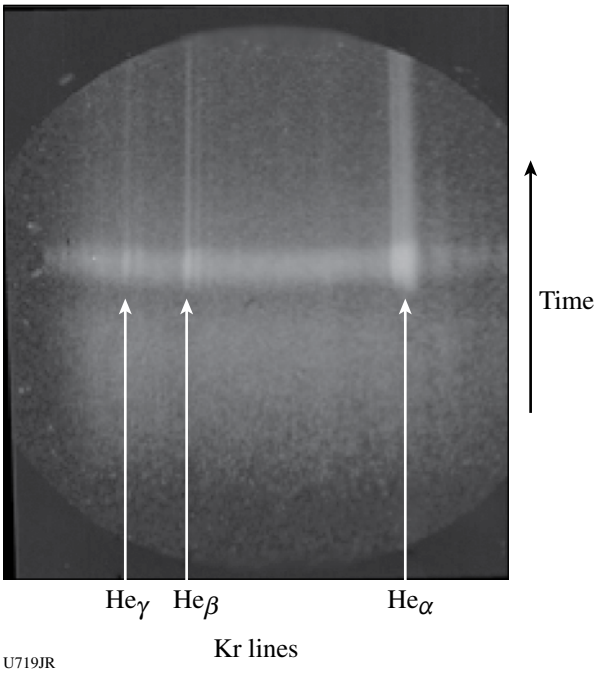

Figure 112.64
Typical time-resolved spectrum from the mica conical crystal spectrometer for a capsule without Xe dopant.

pinhole images show a dramatic reduction in areal density and core size as the Xe concentration is increased.

One of the campaigns planned for the NIF will study the opacities of high-temperature plasmas in LTE conditions. Present-generation long-pulse facilities produce LTE plasmas in the range of 100 to 180 eV, and the intent is to extend this range upward on the NIF. To do so, it is desirable to optimize the coupling of high-intensity laser radiation to produce x rays from small targets, which in turn heat samples in LTE conditions. In FY07 the high-temperature hohlraum development campaign began studying the utility of rear-wall burnthrough radiation from the back of a small halfraum as a technique for radiatively heating samples several hundred microns away. Figure 112.65 shows data from plastic (carbon) and chromium samples diagnosed with x-ray spectroscopy. Surprisingly, the samples were cooler (under-ionized) relative to what was predicted. Future work will focus on improving the modeling to match the observations and then looking for ways to optimize the experimental configuration.

To produce multiple radiographic images with a single NIF shot, with a minimum number of NIF beams devoted to the backlighter, it is desirable to have a long-duration point-projection backlighter source. To this end, a few half-days were devoted to developing a long-duration, pinhole-apertured,

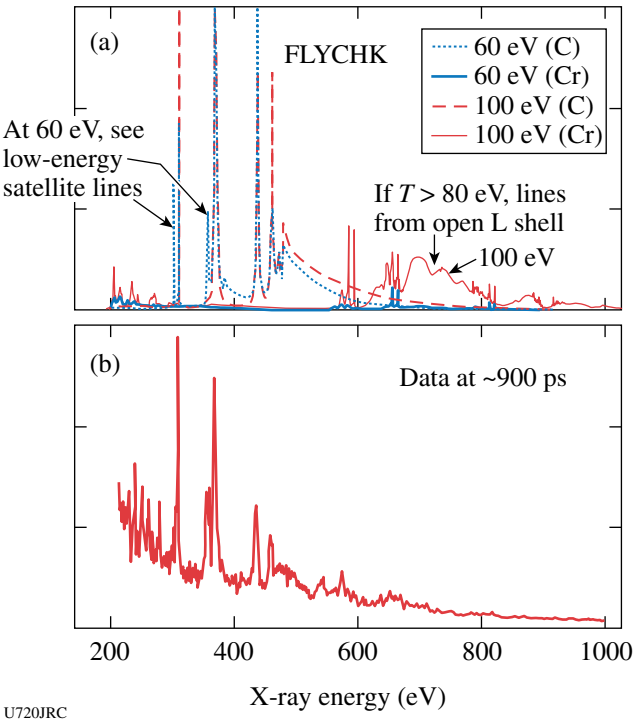

Figure 112.65
(a) Spectroscopic data from a target radiatively heated by the thin back wall of a tiny holraum. (b) Comparison with modeling indicates target temperature is 60 to 70 eV at this time.

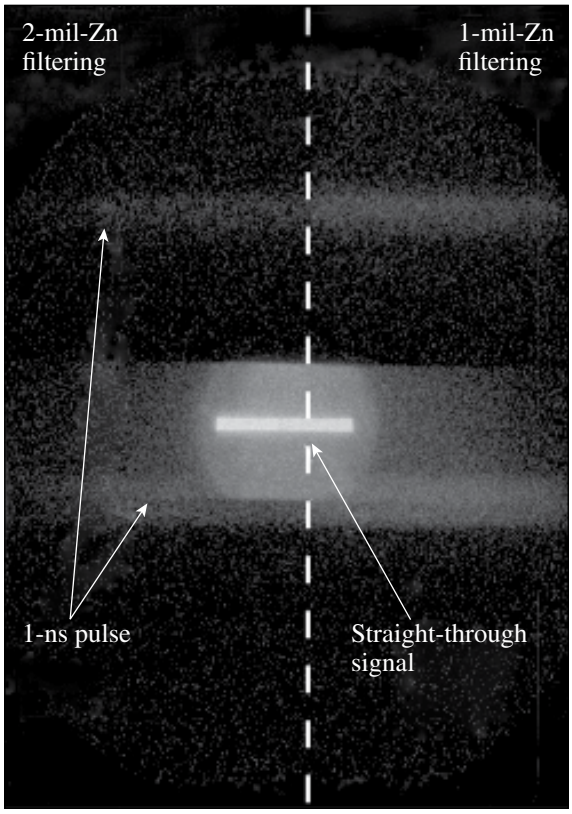

Figure 112.66
Streak measurement of Zn backlighter radiation from multiple OMEGA laser pulses, demonstrating adequate signal-to-test, long-duration backlighter concepts for the NIF.

point-projection zinc K-shell backlighter to diagnose NIF experiments. Current laser experiments use pulses of typically 0.2 to 1.0 ns. Extending the backlighter duration out to the desired 8 ns for the NIF leads to issues of pinhole closure and signal strength. Initial experiments using a streak camera with an open slit showed a significant contribution to the background from the streak camera's retrace signal. Subsequent experiments (Fig. 112.66) showed that increasing the laser intensity on the backlighter and using zinc filtering to block unwanted low-energy radiation was sufficient to produce an adequate signal above the retrace and other backgrounds. The continuation of this campaign in FY08 will explore pinhole closure time and new backlighter designs aimed at increasing the signal-to-noise ratio without sacrificing resolution.

To further improve hohlraum heating efficiency and reduce plasma filling (which obscures radiographic views of HED material samples), hohlraum development experiments have been conducted using laser-driven cylindrical hohlraums whose walls were machined from Ta_2O_5 foams of 100-mg/cc and 4-g/cc densities. Measurements of the radiation temperature, shown in Fig. 112.67, demonstrate that the lower-density walls produce higher radiation temperatures than the higher-density

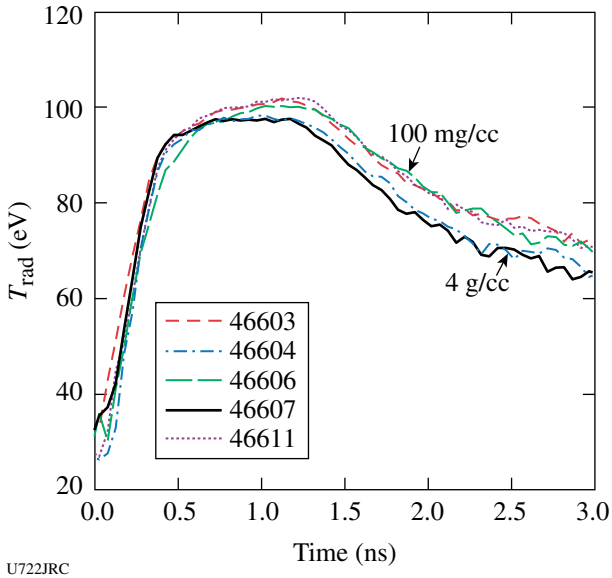

Figure 112.67
Radiation temperature from Dante measurements for five foam-walled hohlraums.

walls. The difference in temperature is determined by the difference in energy lost to the walls. For higher-density walls, the radiation front propagates subsonically, so the density seen by the front is dominated by the density profile established by the rarefaction wave. For lower densities the radiation-front velocity is supersonic so the energetics of the wall are determined by the equation of state and the opacity of the wall material.

FY07 LANL OMEGA Experimental Programs

During FY07 Los Alamos National Laboratory (LANL) successfully fielded a range of experiments on OMEGA to study the physics relevant to inertial confinement fusion (ICF) and high-energy-density laboratory plasmas (HEDLP) in support of the national program. LANL conducted a total of 192 target shots on OMEGA, 22% higher than the nominal allocation. Collaborations with LLNL, LLE, MIT, and AWE remain an important component of LANL's program on OMEGA. In particular, the LANL-led symergy campaign has provided a better understanding of symmetry control for the future NIF ignition experiments.

Radiation Transport in Inhomogenous Media: The inhomogeneous radiation flow experiment was allotted a single shot day in FY07. This experiment studies the transport of radiation through inhomogeneously mixed media; that is, where discrete particles of random size are randomly dispersed in a host material. For a constant gold fraction, the effective opacity of the mixture is expected to increase as the particle size decreases, thereby slowing the radiation propagation in the media. Many models describe this phenomenon,[19–24] but it has not been demonstrated that these models are implemented correctly in our codes.

The radiation source for these experiments is a hohlraum nominally heated by 7.5 kJ of laser energy to a peak temperature of about 210 eV (Fig. 112.68). The radiation from the hohlraum drives a temperature front into a gold-loaded foam. The foams are nominally 55 to 60 mg/cm^3 of triacrylate ($C_{15}H_{20}O_6$) foam containing nominally 12% by atom gold particles. The size of the gold particles is varied during these experiments to observe how the particle size impacts the temperature-front propagation.

An example of the effect the gold particle size has on the temperature-front propagation is shown in Fig. 112.69. The data clearly show this effect for the temperature-front propagation for two gold particle cases: 5-μm diameter and atomic mix. At early times, the temperature-front propagation is similar; however, at 2.5 ns there is roughly a 100-μm difference between the two cases. Also, simulations with the Langrangian radiation hydrodynamics code NYM[25] (Fig. 112.70) show excellent agreement with the experimental data in the atomic-mix case.

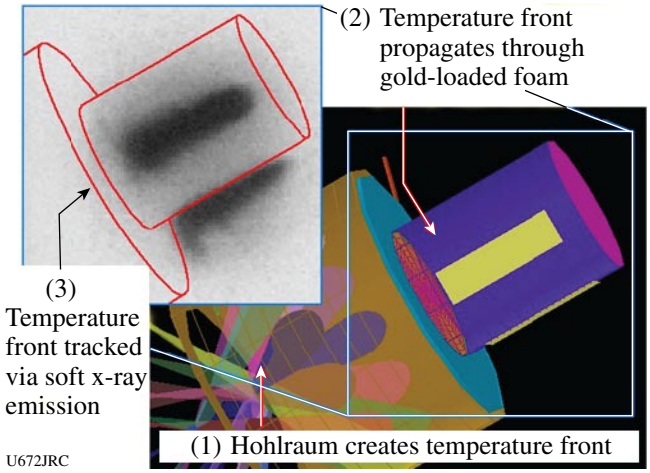

Figure 112.68
A schematic of the inhomogeneous radiation flow platform.

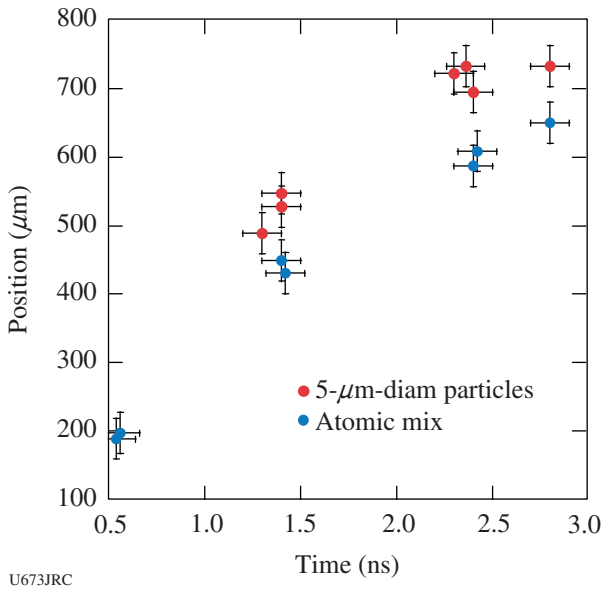

Figure 112.69
Experimentally determined temperature-front position showing the differences between foams loaded with 5-μm-diam gold particles and an atomic mix with gold particles. By 2.5 ns, the temperature front has propagated 100 μm farther in the 5-μm particle case than in the atomic-mix case.

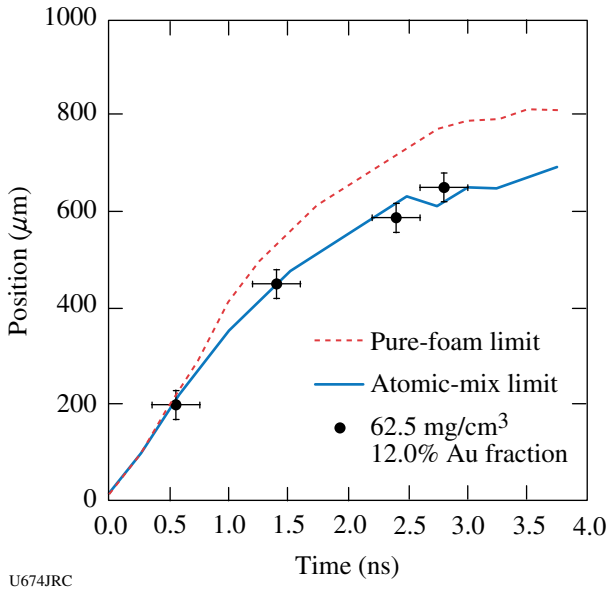

Figure 112.70
A comparison of the simulation in the pure-foam and the atomic-mix limits versus the experimental data. The atomic-mix simulation is in excellent agreement with the experimental results.

Off-Hugoniot Experiments: Recent experiments by LANL on OMEGA explored the hydrodynamic evolution of embedded layers subject to radiative heating. These experiments, focusing on hydrodynamic evolution, are being used for quantitative validation of 3-D Advanced Scientific Computing (ASC) calculations of both large- and small-scale hydrodynamic motion. In contrast to traditional shock-interaction experiments, the material conditions are constantly changing with time before and during the shock-interaction process. The complex material and density gradients developed during the heating phase significantly change the shock evolution from what it would be with the initial "as-built" profile. Thus far, the types of embedded features fielded include planar disks, rectangular gaps, and, most recently, single-mode sinusoids. This campaign began in 2004 and continues today with significant collaboration from the Atomic Weapons Establishment (AWE). Current efforts have shifted from data collection to analysis and quantitative comparison with simulations. In FY07 LANL conducted two days of shots on OMEGA that yielded high-quality images of both heated and shocked-gap targets as well as newly fielded sinusoid targets (Figs. 112.71 and 112.72). Data from the sinusoid targets show a recurring phase inversion of the sinusoid pattern as predicted by 3-D ACS calculations.

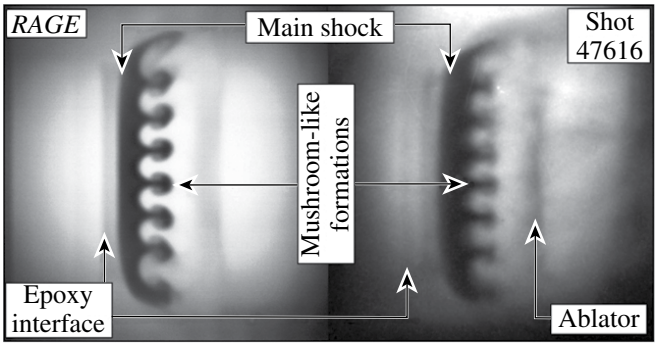

Figure 112.72
Comparison of 3-D ASC *RAGE* calculation (left) with experimental data (right) of heated and shocked sinusoid targets.

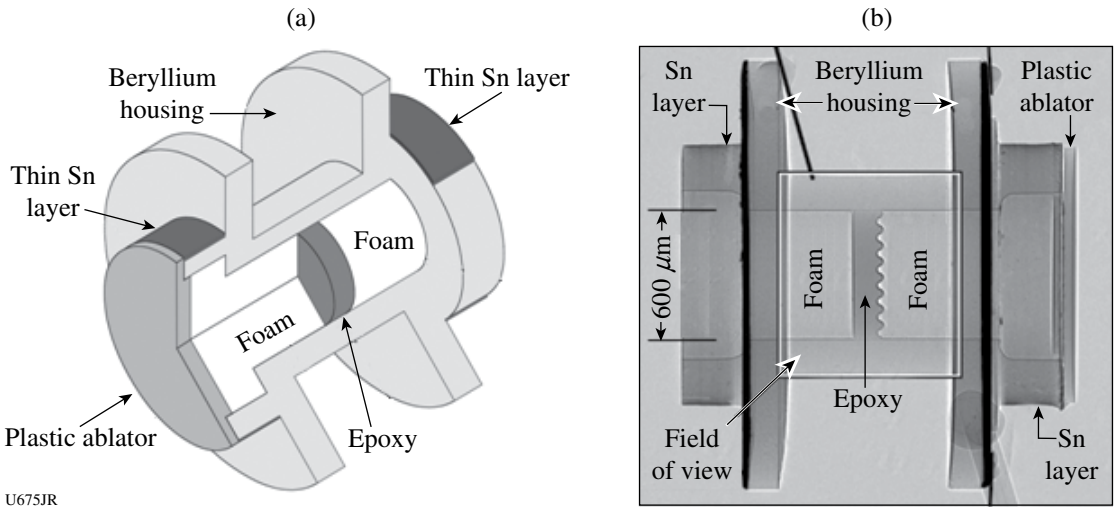

Figure 112.71
(a) Targets consist of a Be housing with epoxy between 60-mg/cm^3 foam parts. A plastic ablator is used to generate shocks. (b) Full target characterization is performed before shots including radiographic images to determine part alignment and material impurities.

NIF Platform #5: The NIF Platform #5 (NIF 5) Campaign is developing x-ray diagnostic techniques to measure temperature in radiation-transport experiments on the future National Ignition Facility (NIF). In FY07 NIF 5 had 1.5 shot days and obtained extremely useful data. This year NIF 5 met both of its main objectives: to measure the spectrum of a suitable backlighter source and to determine the temperature of a foam that had been radiatively driven.

The NIF 5 platform (Fig. 112.73) utilizes a quasi-continuum backlighter and a hohlraum to heat a low-density foam. In some configurations, the backlighter alone is used to measure its x-ray emission spectrum.

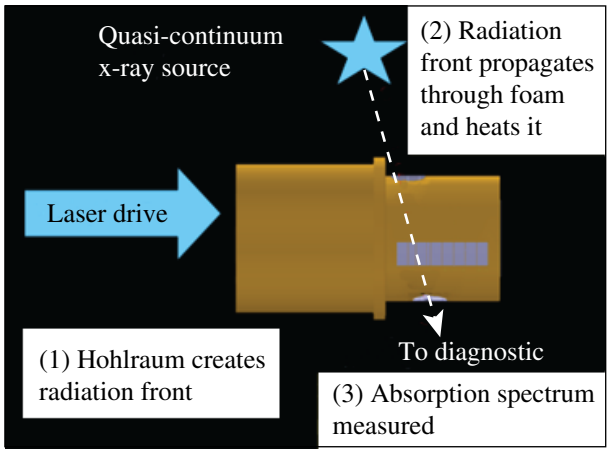

Figure 112.73
A schematic of the NIF 5 platform experimental configuration.

Figure 112.74 displays an example of the absorption data obtained. The emission present is due to the M-band emission of the gold backlighter. The backlighter emission was initiated before the foam was heated and continued during the heating

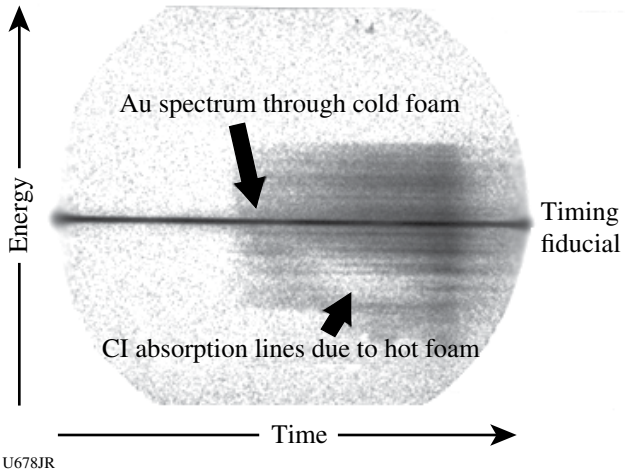

Figure 112.74
Measured absorption spectrum due to a heated foam. The vertical axis is the spectral energy (increasing to the top) and the horizontal axis is time (increasing to the right). The emission is due to the M band of the gold backlighter.

phase of the foam. As the foam heats, the absorption spectrum profile changes, which is captured by the data.

Symergy: LANL fielded two days of OMEGA experiments to test the concept of using thin shells to quantify asymmetry during the foot of the NIF pulse in support of the National Ignition Campaign. Figure 112.75 shows the ~0.7-scale NIF hohlraum geometry used for these experiments. Three cones of beams enter the hohlraum from each side with a 3-ns laser pulse to produce a peak radiation temperature of ~115 eV, comparable to the foot pulse incident on an ignition capsule.

The emission levels from the capsule implosions (Fig. 112.76) proved the concept of thin-shell capsules as a symmetry diagnostic for the NIF. Furthermore, the variation in symmetry with beam cone pointing shows that one-way capsule asymmetries could be corrected at the NIF. These quantitative results showed

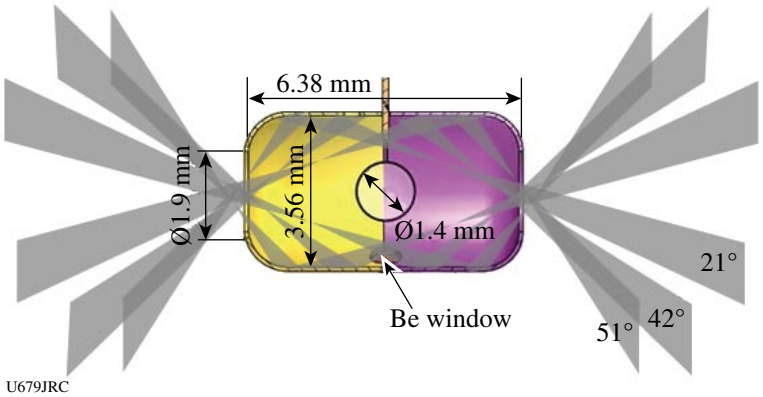

Figure 112.75
Gold hohlraum with an x-ray diagnostic port used in thin-shell symmetry capsule experiments. The capsule is a 1400-μm-diam, 15-μm-thick CH shell filled with 1 atm of D_2.

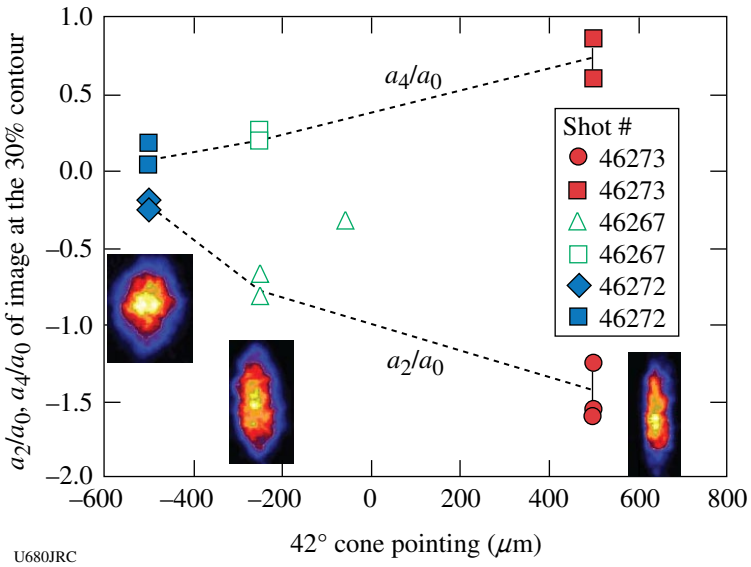

Figure 112.76
Observed time-integrated x-ray images and corresponding P_2 and P_4 asymmetries as the pointing of the 42° cone is moved along the hohlraum axis.

that we can now proceed to tune asymmetry in the foot of a full-scale NIF ignition capsule using the 96-beam configuration in FY08!

Convergent Ablator: Two shots days were dedicated to investigating the slowing of protons from the D + ^{3}He reaction to diagnose the ablator remaining at ignition in a NIF target in collaboration with MIT. Capsules were imploded in a 3/4-scale OMEGA hohlraum driven by 19 kJ in a 1-ns square pulse with hohlraum temperatures peaking at ~270 eV. By driving different thicknesses of CH capsules we could obtain different final ablator and fuel ρR's to test our ability to observe and calculate downshifts of the 14.7-MeV proton by up to ~1.5 MeV.

The results of this campaign confirmed our predictions of hohlraum temperature and our ability to observe gated images in self-emission of the imploding capsules. Figure 112.77 shows the observed neutron yields from nine capsules for capsule wall thicknesses varying from 25 to 55 μm thick. The points labeled "Nom 70% LEH" are calculated yields without mix. The triangles include expected degradation by mix as the capsules converge more with increasing initial thickness. Observed x-ray images for all but the 55-μm-thick capsules were round. MIT is now analyzing the charged-particle detectors to obtain total proton yield and spectra from emitted protons. Initial results with a 35-μm-thick capsule had enough yield to obtain a spectra, and calculations agreed with the measured energy shift.

In a similar experiment,[26] abundant hard x rays were measured indicative of hot-electron production. By varying laser energy in each of the three laser cones, we were able to determine that hard x rays were being produced almost entirely by the innermost cone, and that hot-electron temperatures were >100 keV. The particle temporal diagnostic (PTD) and neutron temporal diagnostic (NTD) instruments, modified to become hard x-ray detectors, showed peak emission at ~0.7 ns and a subsequent decrease, within the 1-ns laser pulse. In calculations this corresponded to the appearance of a quarter-critical-density surface between hohlraum wall and capsule ablator expansions. We showed increased x-ray production when the plastic-capsule ablator was changed to beryllium from CH, and no 3/2ω radiation from either type. These results are still being analyzed but

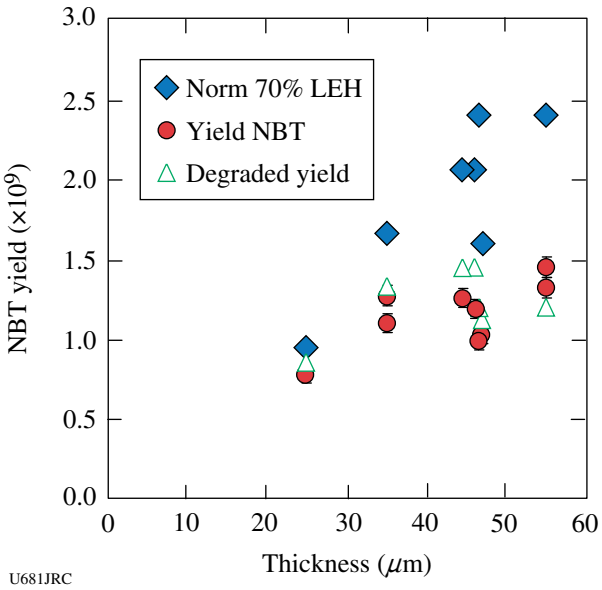

Figure 112.77
Observed and calculated D + D neutron yields from the convergent ablator experiment.

suggest that Raman scattering plays an important role in hot-electron production, as suggested from laser-instability postprocessing of the *LASNEX* hohlraum calculations.

Laser–Plasma Interactions: Gas-filled hohlraums are often used for high-energy-density laser experiments including inertial confinement fusion. While the gas fill is needed to provide a hot ionized plasma whose pressure prevents the ablated wall material from filling the hohlraum, it can also potentially lead to large laser–plasma instability growth since a long-scale-length quasi-homogeneous plasma is often created. One instability that may be detrimental to gas-filled hohlraum experiments is stimulated Raman scattering (SRS), which occurs when intense laser light resonantly decays into an electron-plasma wave and a backscattered light wave. Two strategies for mitigating SRS were investigated in FY07 on the OMEGA laser using gas-filled hohlraums.

The first strategy uses a small amount of a high-Z dopant in the low-Z gas fill, which had previously been observed to reduce SRS in experiments at the Helen laser and last year on the OMEGA laser. These experiments, which were a continuation of experiments started in FY06, heated a 1.6-mm-diam, 2.0-mm-length, Au gas-filled hohlraum. The hohlraum is filled with ~1-atm C_5H_{12} gas and has 0.25-μm-thick polyimide windows over the 0.8-mm-diam laser entrance holes (LEH's). The target is aligned along the B30 axis and heated with up to 12 kJ using 32 beams in three cones in a 1-ns pulse. After plasma formation, B30 is used to interact with the long-scale-length plasma with an intensity ~10^{15} W/cm^2, smoothed with a 150-μm CPP and full-bandwidth SSD. The 3ω transmitted-beam diagnostic (TBD) measures the transmitted light, and the full-aperture backscatter station (FABS) measures SRS and SBS growth. For this set of experiments, a small amount of Xe dopant was added to the gas fill and systematically varied up to 9% atomic fraction. These experiments indicate greater than a factor-of-2 decrease in SRS reflectivity when the Xe dopant is 1%. Experiments with a B30 intensity of 1.8×10^{15} W/cm^2 with SSD on or at 10^{15} W/cm^2 with SSD off show little change in SRS with 1% Xe. Comparison of these results with radiation hydrodynamic calculations is ongoing and will help rule out whether the effect can be simply explained by an increase in inverse Bremsstrahlung absorption, or whether competition of SRS with beam spray is the mechanism responsible for the observed decrease in SRS.

The second strategy examined this year used lower-density gas fills to increase Landau damping via the dimensionless parameter $k\lambda_D$, where k is the wave number and λ_D is the Debye wavelength. To examine the effects of high-$k\lambda_D$ regimes on SRS, the critical onset intensity for SRS is measured. A critical onset occurs theoretically for a random-phase-plate–smoothed laser beam with a distribution of intensities with a well-defined spatial correlation length (speckle length). As the average laser intensity increases, the calculated SRS gain diverges, leading to a saturated reflectivity. This is experimentally determined by measuring a sharp increase from no reflectivity to large reflectivity for a small increase in laser intensity. As $k\lambda_D$ increases, Landau damping of the electron-plasma wave increases, thus increasing the SRS critical onset intensity. In these experiments, mixtures of C_5H_{12} and C_3H_8 were used at different pressures to vary the electron density. B30 was used at an intensity of 10^{15} W/cm^2 with SSD to interact with the preformed hohlraum plasma and drive SRS. As the electron density is lowered, the critical onset for SRS occurs at a higher intensity, qualitatively consistent with theory. In Fig. 112.78, the presence of large SRS (>10%) is plotted in the gray circles, and the presence of small SRS (<1%) is plotted as open circles. For a small change in plasma density at a fixed laser intensity, or a small change in laser intensity at a fixed plasma density, SRS increases rapidly to a saturated state. The dashed line is plotted as a guide to indicate the demarcation of the measured critical onset.

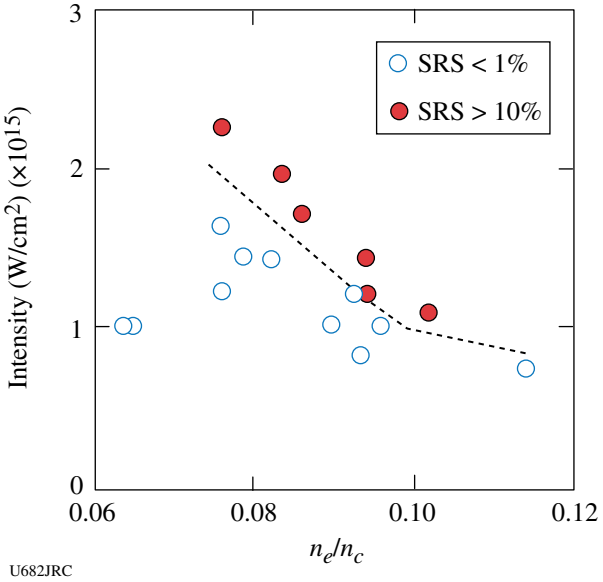

Figure 112.78
SRS levels as a function of n_e/n_c. The dashed line is plotted as a guide to indicate the demarcation of the measured critical onset.

Hi-Z: To better understand the effects of instability growth and the resulting mix, we need to be able to calculate the performance of capsule implosions with known quantities of

preimposed mix. Two days of directly driven implosions on the OMEGA laser in 2007 have tested the effects of pre-mix of Ar, Kr, and Xe in D_2 + ^{3}He–filled glass microballoons. In FY07 we focused on the effects of argon pre-mix, while earlier experiments explored Kr and Xe. Diagnostics included D + D and D + T neutron yields, D + ^{3}He proton yields and spectra, Doppler-broadened ion temperatures, time-dependent neutron and proton burn rates, and time-gated, high-energy filtered x-ray images. Simulated yields agree better with the experiment when calculated by XSN LTE[27] than by non-LTE atomic physics packages.

Measured yields with a small amount of pre-mix, atom fractions of ~5×10^{-3} for Ar, 2×10^{-3} for Kr, and 5×10^{-4} for Xe are more degraded than calculated, while the measured ion temperatures are the same as without pre-mix. There is also a decrease in fuel ρR. The neutron burn histories suggest that the early yield coming before the reflected shock strikes the incoming shell is undegraded, with yield degradation occurring afterward. Adding 20%-by-atom ^{3}He to pure-D fuel seems to produce a similar degradation. This ^{3}He degradation was previously observed in directly driven plastic shells by Rygg *et al.*[28] Figure 112.79 shows how calculated gated x-ray images agree in radius with the observed images when the reflected shock strikes the incoming shell at 1.18 ns but are smaller than the observed images afterward. This lack of convergence and lower fuel density partially explains the yield degradation as well as the low fuel and whole capsule ρR's observed in secondary T + D neutrons and slowing of the D + ^{3}He protons. Neither the LTE nor non-LTE models capture the degradation by ^{3}He or with low Ar, Kr, and Xe pre-mix levels, nor do they match the large shell radii after impact of the reflected shocks.[29]

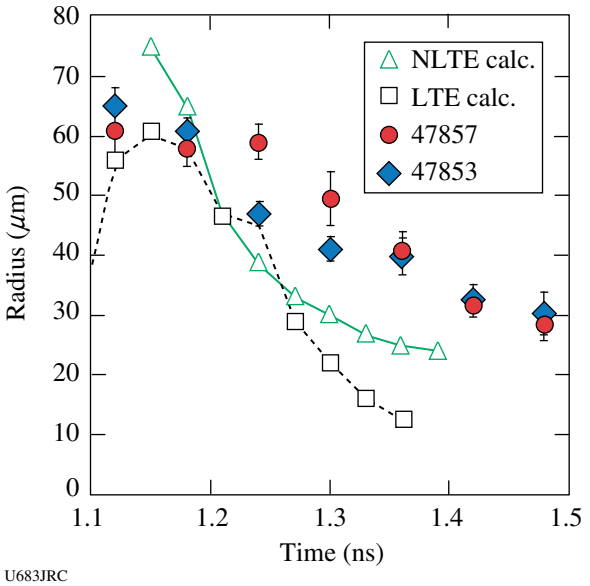

Figure 112.79
X-ray-image radius with (shot 47857) and without (shot 47863) ^{3}He versus simulated using LTE and non-LTE.

Reaction History: In October 2006, LANL conducted the *Reaction History Structure Using a Double Laser Pulse* experiment to study the effects of time-dependent mix in a DT capsule implosion. Two temporally separated laser pulses, as seen in Fig. 112.80(a), were used to obtain double peaks in the fusion reaction history as determined by deconvolved measurements from the gamma-based gas Cherenkov detector (GCD) and the

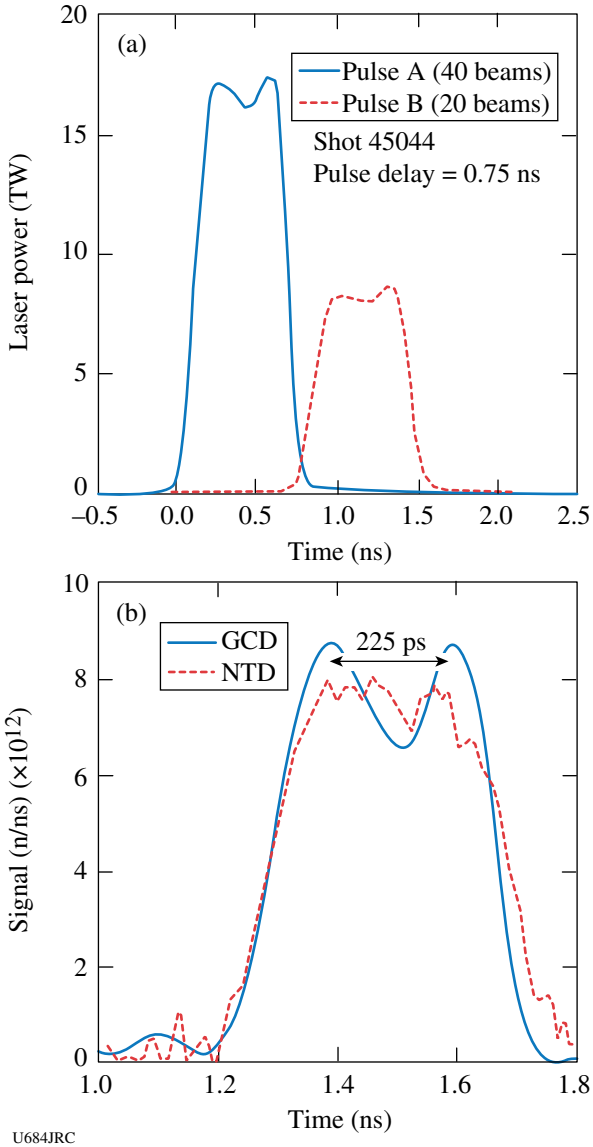

Figure 112.80
(a) Double-pulse laser waveforms; (b) double-pulse reaction history.

neutron temporal diagnostic (NTD) as shown in Fig. 112.80(b). The expected double-peak character of the reaction history is well resolved by the GCD. The first laser pulse contained 10 kJ in 40 beams and the second 5 kJ in 20 beams. Each was a square 600-ps pulse. This shorter-than-usual 1-ns laser pulse allows the shock and compression fusion burn components to be separated in time. Comparisons with modeling are indicating that the first peak is dominated by shock yield and the second peak, a result of compression burn, becomes significant only when the delays between pulses are less than 800 ps. This is contrary to the leading mix models, such as Scannapieco and Cheng, which predict a dominant compression burn, and is requiring us to invoke the harsh mix of a fall-line mix model to explain these observations.

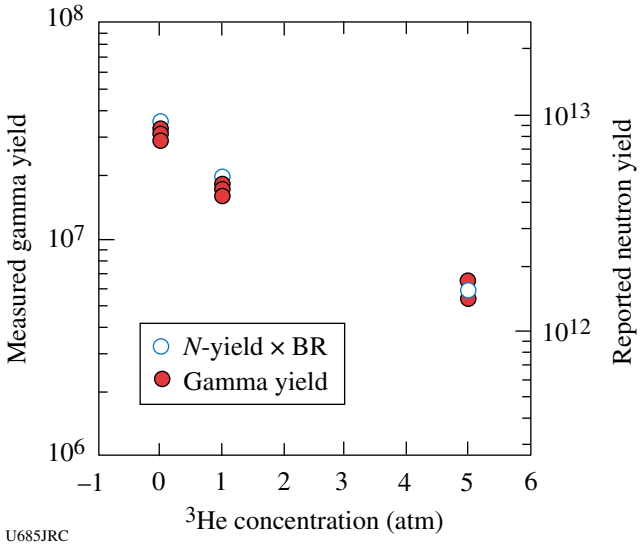

Figure 112.81
Neutron and γ-ray yields versus ^{3}He concentration shows a decrease in yield as the ^{3}He concentration is increased.

DTRat: In June 2007, LANL conducted the *DT Ratio-^{3}He Addition (DTRat)* experiment to investigate the effect of ^{3}He on the yield and reaction history of DT implosions. The DTRat experiment also used 600-ps laser pulses, but at 50% more energy: 15 kJ versus 10 kJ in the first pulse of the double-pulse experiment. As seen in Fig. 112.81, the absolute DT fusion gamma and neutron yields are consistent with each other and dropped by 80% in going from 0% to 33% ^{3}He addition (i.e., 5 atm ^{3}He). The shock and compression burns agree with the Scannapieco and Cheng mix model relatively well as determined by the GCD-measured reaction history shown in Fig. 112.82, so there was no need to resort to fall-line mix in this case. In both calculations and experiment, the compression burn is clearly much more degraded by the addition of ^{3}He than is shock burn.

The MIT group had previously determined that the addition of ^{3}He to DD in thick plastic shells resulted in approximately a factor-of-2 anomalous drop in scaled yield [i.e., yield over clean (YOC)] at 50% ^{3}He by atom as compared to pure DD or nearly pure ^{3}He, as seen in Fig. 112.83 (Ref. 27). While a drop in scaled yield with the addition of ^{3}He was observed for DT, it was not

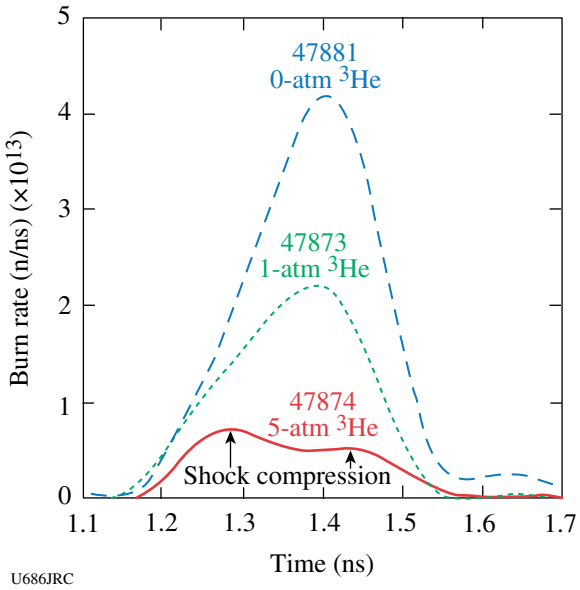

Figure 112.82
Burn history versus ^{3}He concentration.

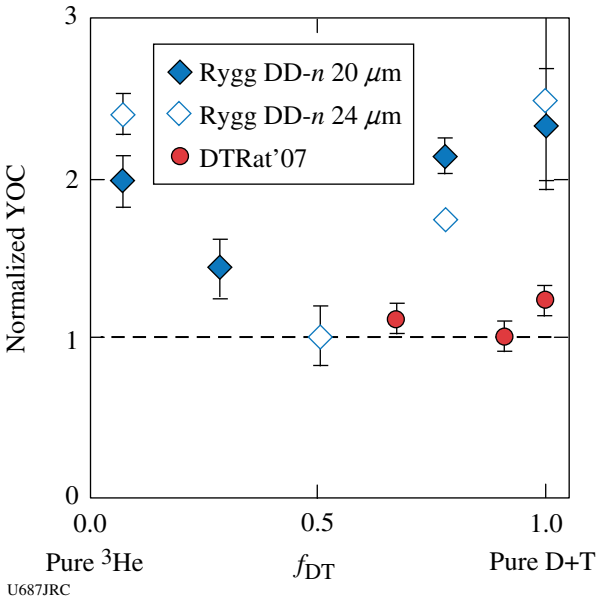

Figure 112.83
Scaled neutron yield normalized to 1 at the minimum for 20- and 24-μm plastic shells (Rygg) and 4.7-μm glass shells (DTRat'07).

nearly as significant as reported for DD. These data are the first of a planned series to study the effects of ^{3}He concentration on implosion yield and reaction history using DT capsules.

Beta Mix: Ignition experiments at megajoule/terawatt laser facilities will take the field of high-energy-density science into new frontiers, in terms of both physics and diagnostic capabilities. In particular, understanding the nature and amount of mix caused by hydrodynamic instabilities in inertial confinement fusion (ICF) targets is important from a fundamental physics perspective as well as for optimizing target performance. A radiochemical diagnostic to measure the amount of mix is being developed at Los Alamos National Laboratory. Figure 112.84 shows a conceptual diagram of how the diagnostic would be implemented. Neutrons produced in deuterium and tritium fusion interactions traverse the fuel to the ablator interface where they can upscatter tritons to MeV energies. Given the electron density or temperature (T_e) in this region, the triton range is quite short. Thus, the probability for ^{9}Be(t,x) interactions will depend strongly on the amount of mix that has occurred.

The diagnostic proposed for the National Ignition Facility is to collect and measure ^{8}Li atoms produced in ^{9}Be(t,α) interactions. Short-lived radiochemical signatures, such as ^{8}Li (half-life of 840 ms, and a Q_β of 13.4 MeV), provide a distinguishable signature for measuring mix, as MeV-scale backgrounds from prompt activation at the millisecond and greater timescales should be small. Further, this approach is not subject to systematic uncertainties from nontarget backgrounds from which stable and metastable isotope techniques can suffer. The two keys to executing this diagnostic are the ability to collect target debris after the implosion and the ability to begin counting the radionuclide decays of interest within this collected debris.

To gain insight into the issues surrounding radionuclide counting after a high-yield ICF shot, experiments were performed on OMEGA. Detectors were located both on the target chamber wall and inside a re-entrant tube to provide a prompt, high-fluence flash of radiation that must be addressed prior to initiating counting. The prompt radiation burst was also used as an activation source for counting experiments. Activation targets were located directly in front of the counters and included graphite and ^{15}N-enriched NH_4Cl. The graphite provided a source of ^{12}B atoms ($\tau_{1/2}$ = 20.2 ms, Q_β = 13.4 MeV) through ^{12}C(n,p)^{12}B interactions, while the ammonium chloride was a source of ^{15}C atoms ($\tau_{1/2}$ = 2.45 ms, Q_β = 4.5 and 9.8 MeV) through ^{15}N(n,p)^{15}C interactions. Figure 112.85 shows the results of measurements made with the graphite target. The data were collected using a scintillation telescope, with a Pilot-B scintillator and Burle 8575 photomultiplier tubes (PMT's). The PMT bases were custom bases that included a gating circuit to reverse bias the photocathode of the PMT to partially blind the tube during the prompt radiation burst. The anode signals from each PMT were discriminated, subjected to a coincidence requirement, and recorded in a multchannel scaler. The scaler data were then fit in the region of the ^{12}B decay, and an abundance calculation was made. From this abundance measurement, and a Geant 4 simulation to estimate efficiency and acceptance, it is possible to make a preliminary ^{12}C(n,p)^{12}B cross-section measurement of 300±30 μb at 14.1 MeV.

Debris collection appears to be the most challenging of the two key issues for this diagnostic. A number of attempts have been made to collect target debris at various laser facilities around the world, including OMEGA, but with mixed results. Although gas-collection schemes appear to have been successful, they are not practicable for short half-life counting diagnostics. Figure 112.86 illustrates why it is challenging to

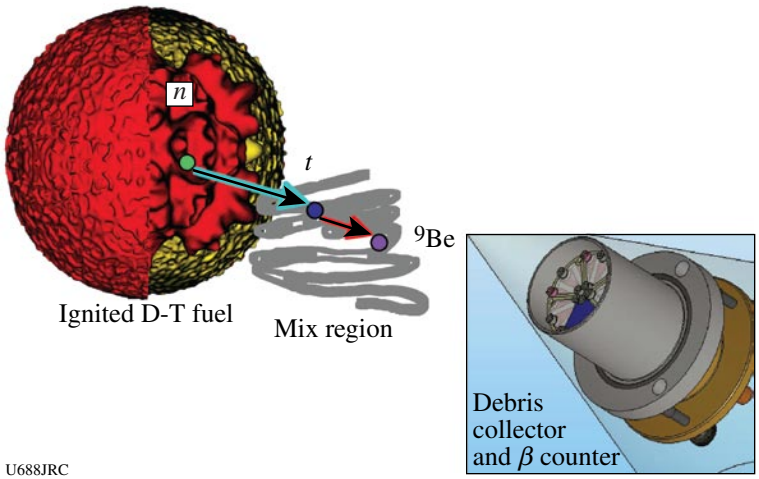

Figure 112.84
Illustration of the "beta-mix" diagnostic concept. Fast neutrons upscatter tritons in the fuel–ablator mix region. Triton–ablator reactions produce unstable daughters with millisecond to second half-lives that are collected and counted by a distant detector.

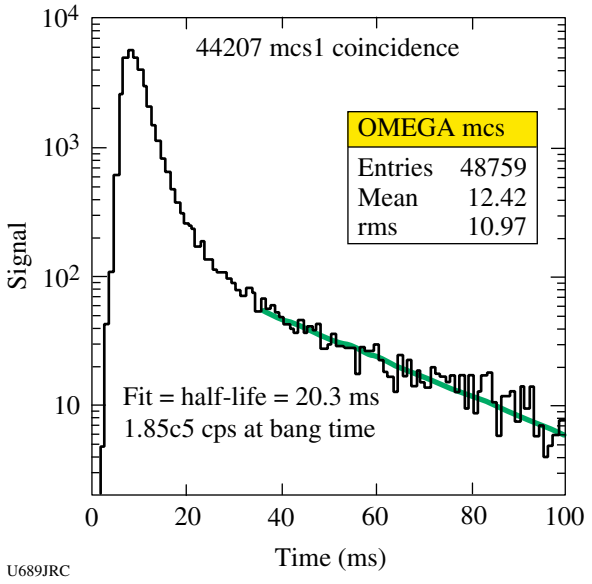

Figure 112.85
Counting data from a Pilot-B coincidence telescope. The half-life fit to the data is consistent with ^{12}B, and the resulting abundance is used to calculate a $^{12}C(n,p)^{12}B$ cross section of 14.1 MeV of 300±30 μb.

collect solid debris on direct-drive experiments. In an effort to improve efficiency of collection within a diagnostic cone, it is desirable to place collector materials as close to the target as possible. Unfortunately, in yield-producing direct-drive shots, two precursor shock waves strike the collector prior to the debris of interest. The first shock is due to the x rays produced at maximum compression. The second, and more damaging, shock in direct-drive scenarios is produced by the ions ablated from the target during laser illumination. The ions are calculated to have ~40 keV of kinetic energy, and if the collector is located close enough to the target, the energy density delivered to the surface of the collector is sufficient to eject a significant amount of mass from this collector. This ejected material drifts with velocities in the cm/μs range normal to the surface. Ejecta formation is illustrated in Fig. 112.87, which shows the surface profile of a 0.004-in. Ti collector foil that was exposed to three direct-drive shots. The foil was positioned 15 cm from the targets and partially covered. Approximately 160 nm of Ti foil was removed from the exposed portion of the foil on each shot. Disassembled target material, which would carry the mix signal of interest in putative experiments, follows the precursor shock materials with kinetic energies calculated to be ~10 keV. Stopping calculations estimate the mean implantation depth of the ~10-keV ions in room-temperature, solid-density Ti is of the order of ~20 nm, which is eight times less than the thickness of material removed by the ablated material shock. These dynamics may explain why past solid collection schemes have met with marginal success.

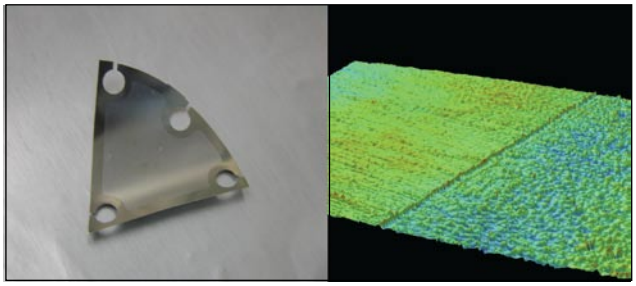

Figure 112.87
A Ti debris-collector foil exposed to three direct-drive shots of CH shells filled with 5 atm of D_2. The right panel shows the difference between exposed and unexposed surfaces. Approximately 160 nm of material was removed on each shot.

During the past year, both counting detector optimization and debris collection experiments have been performed on OMEGA, in support of the Mix in Inertial Confinement Fusion, LDRD DR at Los Alamos National Laboratory. The experi-

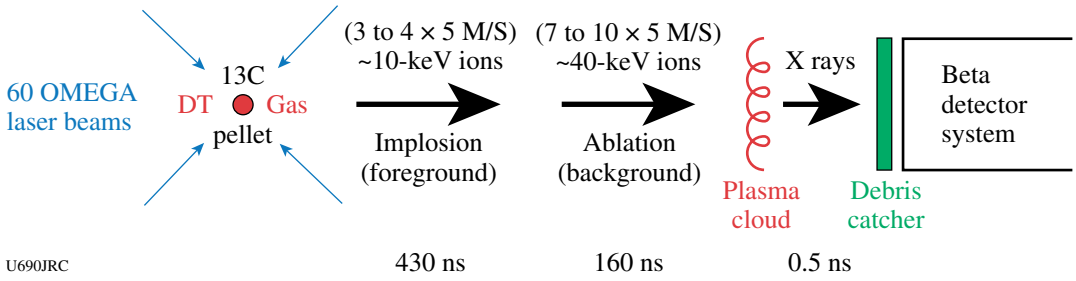

Figure 112.86
Illustration of the shock fronts impinging a debris collector in direct-drive ICF implosions. For a mix diagnostic, the signal is carried in the third shock front to strike the collector.

ments have shown that it is straightforward to count millisecond half-life decays of radionuclides following high-yield implosions on OMEGA. Further, studies are underway to optimize the performance of the counting scheme and to understand the issues to implement such a system in an environment appropriate for megajoule/terawatt-class laser facilities. Debris collection studies have also been initiated. The dynamics of solid debris collection are beginning to be understood, and work during FY08 will be focused on furthering understanding of the dynamics and implementing mitigation strategies to optimize the collector efficiency.

FY07 Sandia National Laboratories
OMEGA Experimental Programs

HDC Ablation-Rate Measurements in Planar Geometry: Accurate knowledge of the x-ray ablation rates of low-*Z* capsule materials will be essential for successful indirect-drive ICF ignition experiments. As part of the U.S. National Ignition Campaign, we have over the past few years performed experiments to measure the x-ray ablation rates in beryllium, copper-doped beryllium, polystyrene (CH), germanium-doped CH, and polyimide. In FY07, we performed the first measurements of the x-ray ablation rates of the diamond-like high-density-carbon (HDC) ablator that has been proposed as a NIF ignition capsule material.[30] The experimental technique for ablation-rate measurements in planar geometry is illustrated in Fig. 112.88 (details in Ref. 31). Basically, ablator samples are placed over an opening on the end of a halfraum. Laser beams that enter through the LEH provide the input power required to maintain the radiation field. The Dante array of K- and L-edge filtered photocathodes views the hohlraum wall through the LEH, and a time- and spectrally resolved measurement of the hohlraum radiation field is obtained from this data. An x-ray framing camera views the interior surface of the ablator sample, and the relative x-ray re-emission of the ablator versus the Au wall is determined. The streaked x-ray imager (SXI) diagnostic views the exterior surface of the ablator sample. The SXI employs an imaging slit, a transmission grating, an offset slit, and a streak camera to provide a highly time-resolved streaked image of the x-ray burnthrough flux on the exterior-facing side of the sample (as shown in Fig. 112.88). The combined information from these three measurements over a series of experiments is used to determine the mass ablation rate

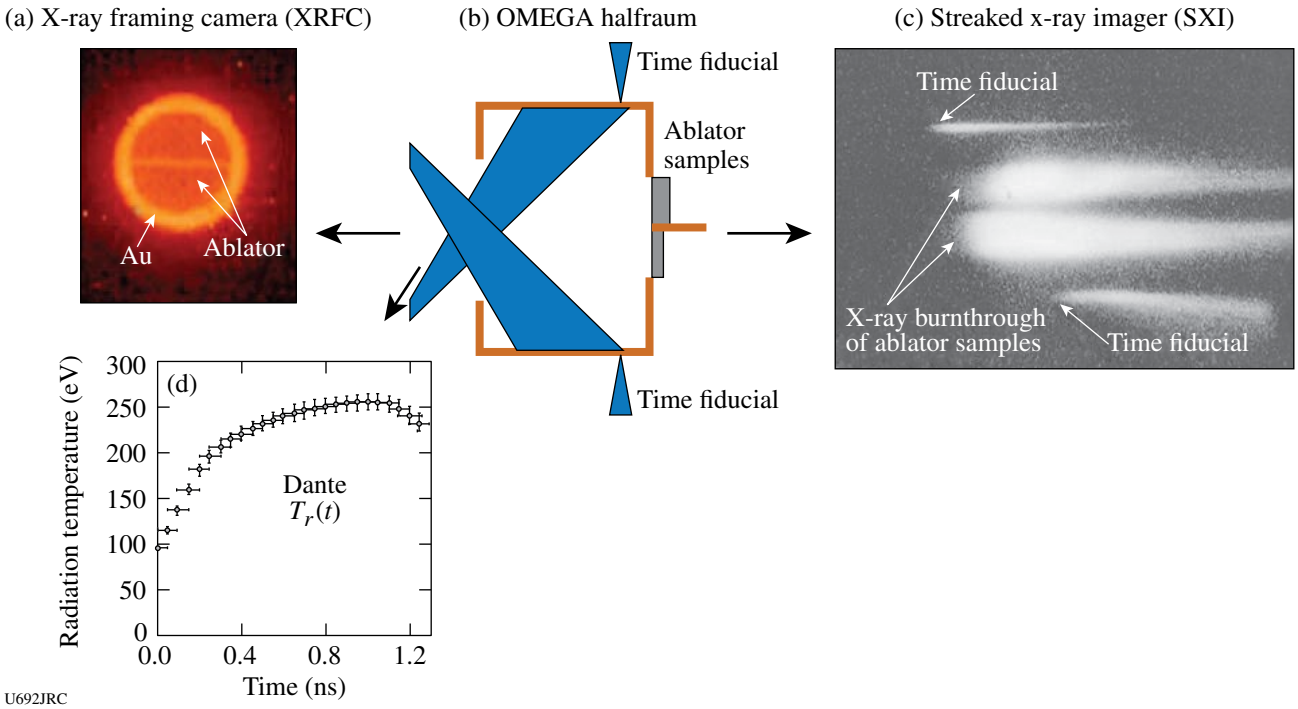

Figure 112.88
(a) The x-ray framing camera (XRFC) provides an x-ray re-emission flux relative to the re-emission of the Au wall (and, therefore, an estimate of the absorbed x-ray flux). (b) Schematic of the burnthrough experiment. (c) The streaked x-ray imager (SXI) measures burnthrough time for each ablator sample thickness. (d) The Dante diagnostic provides a time-resolved hohlraum radiation temperature.

(mg/cm^2/ns) as a function of hohlraum radiation temperature. In previous work, we found that the ablation rates in beryllium range from about 3 to 12 mg/cm^2/ns for hohlraum radiation temperatures in the range of 160 to 250 eV [Fig. 112.89(a)]. As expected, the HDC ablation rates are a bit lower, in the range of 2 to 9 mg/cm^2/ns for temperatures in the range of 170 to 260 eV [Fig. 112.89(b)]. The corresponding implied ablation pressures are in the range of 40 to 160 Mbar for beryllium and 20 to 140 Mbar for diamond (Fig. 112.90). Our post-shot computational simulations (shown as squares

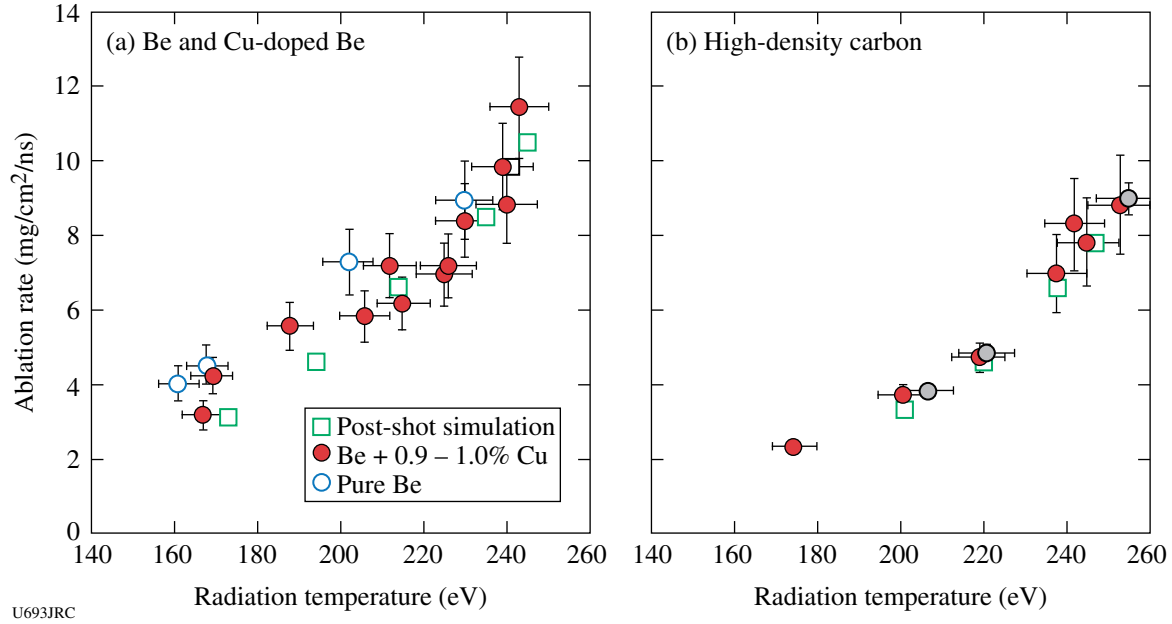

Figure 112.89
Ablation rates measured for radiation temperatures in the range of 160 to 260 eV for (a) Be and Cu-doped Be and (b) high-density carbon.

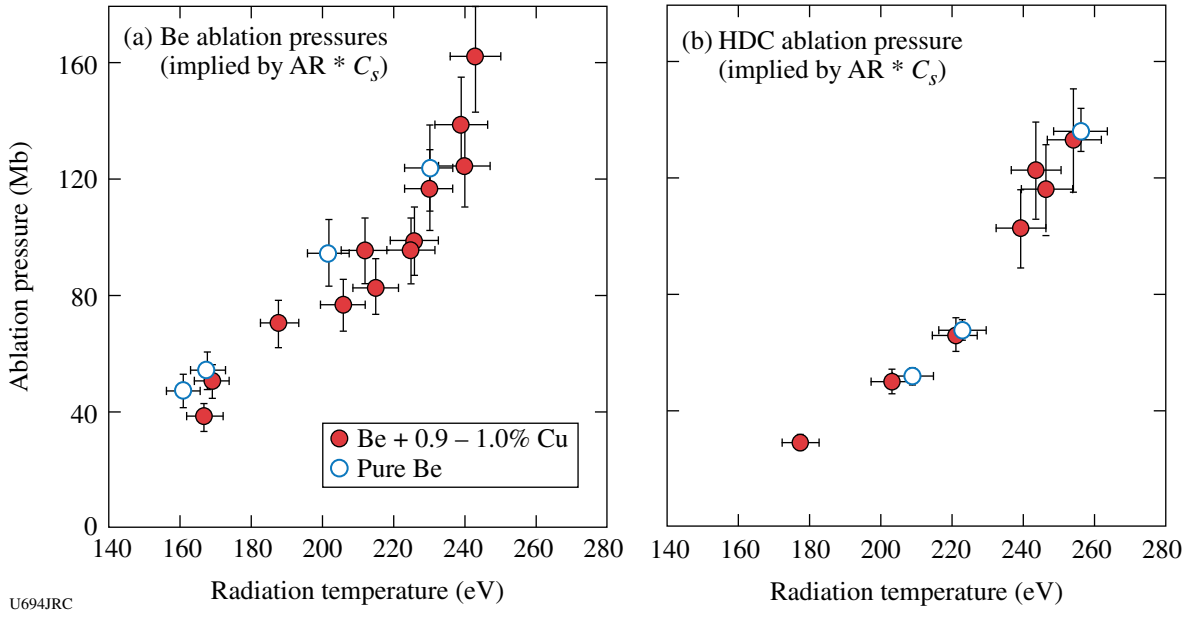

Figure 112.90
Corresponding ablation pressures implied by the data of Fig. 112.89. The Be and HDC ablators approximately follow a $P_r \sim T^{3.5}$ scaling.

on the Fig. 112.89 plots) are mostly within the uncertainties of the ablation-rate measurements. An iterative rocket model has been developed and used to relate the planar ablation-rate data to convergent OMEGA ablation-rate experiments and also to full-scale NIF ignition capsule calculations.

FY07 CEA OMEGA Experimental Programs

Wall-Motion Experiment: Measurements of wall and laser-spot motion in a cylindrical hohlraum were obtained on the OMEGA Laser Facility on 11 September 2007. Wall motion was measured using axial imagery with an x-ray framing camera (XRFC) in the axis of the hohlraum while laser-spot motion was measured using an x-ray streak camera (SSCA) looking through a thinned wall of the target (Fig. 112.91).

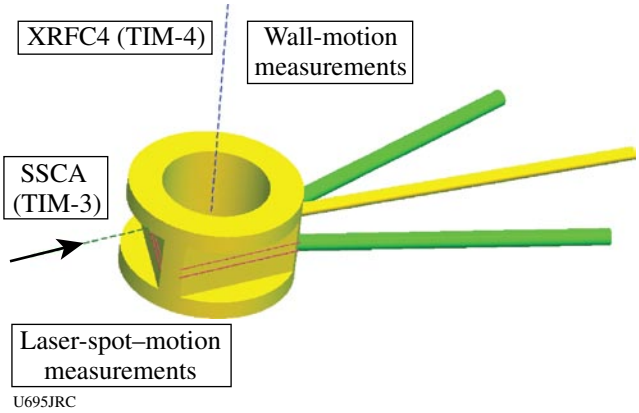

Figure 112.91
Schematic of experimental configuration for OMEGA wall-motion experiments.

Empty hohlraums, CH-lined hohlraums, and a propane-filled hohlraum were shot. Axial imagery (Fig. 112.92) shows that plasma striction comes early in empty hohlraums, while lined and gas-filled targets restrict wall expansion during the PS26 laser irradiation.

Streak images corroborate these results by showing a quicker expansion of laser spots in the case of an empty Au hohlraum (Fig. 112.93).

Neutron Imaging on OMEGA: In a directly driven implosion of a DT capsule, the CEA neutron-imaging[32] system uses a penumbral coded aperture to cast an image of the neutron source onto a detector. The system now routinely provides neutron images with 20-μm resolution. Recently, the system has been used for the first time ever during the implosion of a DT cryo target. An image of the DT cryo implosion is shown in Fig. 112.94(a); an image of a gas-filled target

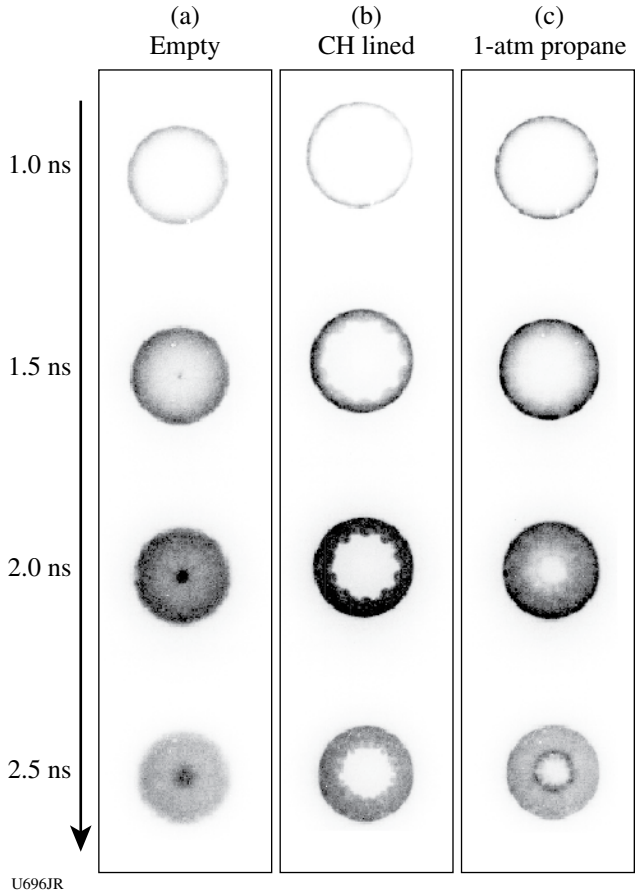

Figure 112.92
Axial x-ray framing camera images of wall motion in (a) empty, (b) CH-lined hohlraums, and (c) 1-atm-propane–filled, respectively.

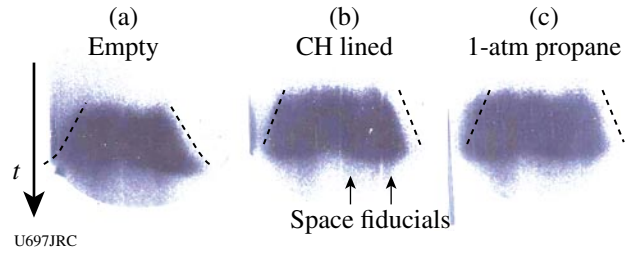

Figure 112.93
Spatially resolved streak-camera images of laser-spot motions in (a) empty, (b) CH-lined, and (c) propane-filled hohlraums.

imploded during the same shot day is shown in Fig. 112.94(b) for comparison.

On the diagnostic technique, the last step of development is to achieve a more valuable measurement with a 10-μm resolution at the source. Novel detectors made of capillaries filled with a liquid scintillator now reach a few-hundred-microns

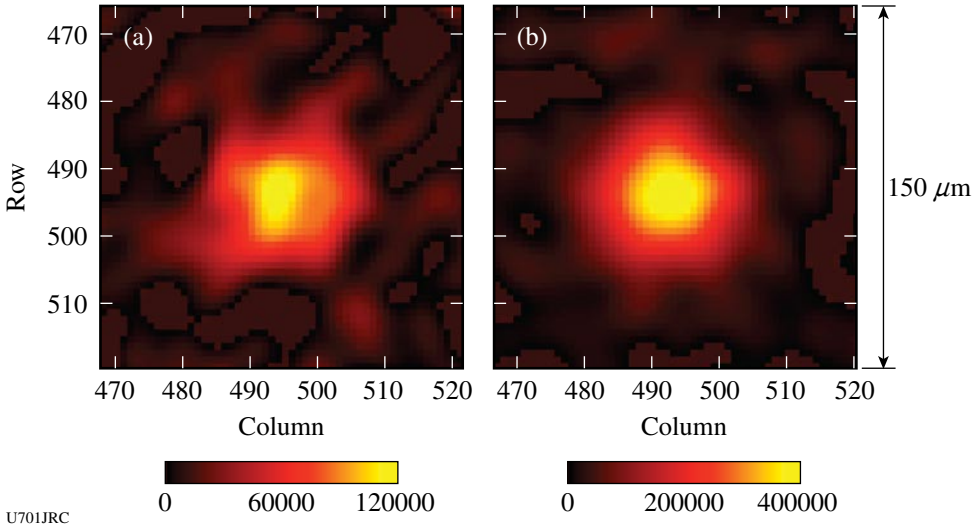

Figure 112.94
(a) Image of DT cryo implosion (shot 47575) yielding 1.1×10^{12} neutrons; (b) image of a DT(15)CH[15] implosion (shot 47551) producing 1.5×10^{13} neutrons.

spatial resolution, which moderates the required magnification ratio of the system and reduces the diagnostic line of path to a more practical distance (<30 m). A high-resolution diagnostic design now appears to be achievable but still requires addressing the resolution and the transmission across the field of view of the neutron aperture. As an example for the penumbral technique, a neutron point source transmitted through the aperture material casts a finite penumbra whose shape depends on the source location in the aperture field of view. This can result in an image distortion as classical unfolding methods assume a constant response across the field of view. These issues have been addressed this year both experimentally on OMEGA and with Monte Carlo calculations.

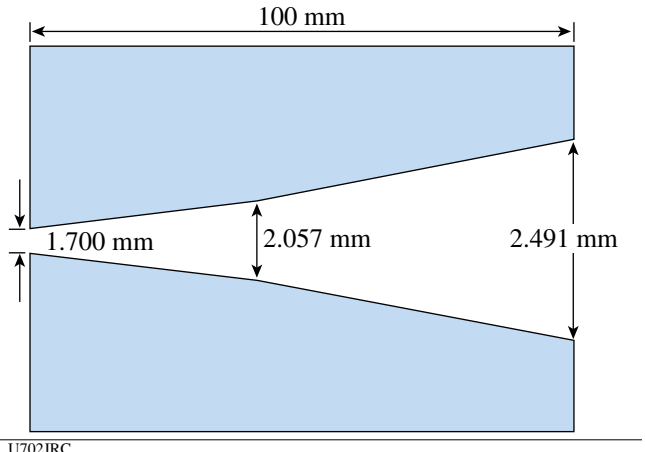

Figure 112.95
Penumbral aperture with a biconical shape made of tungsten.

Our work is performed with a penumbral aperture made by a pair of intersecting cones on the same axes (Fig. 112.95). The middle of the aperture is set at 260 mm from the target chamber center and has a ±100-μm field of view. Using the Monte Carlo code Geant 4, neutrons are transported through the biconical penumbral aperture. The neutron originates from a 50-μm-diam source, and penumbral images are generated for different locations of the source in the aperture field of view. Each of these images is unfolded using our standard autocorrelation method.[33] The reconstructed images present large distortions when the entire source is out of the field of view (see Fig. 112.96). However, when the source is at the edge of the field of view, there is clear distortion in the images.

Such distortions have also been investigated experimentally on OMEGA. The implosion of DT(15)CH[15] capsules produces an intense neutron source. Several neutron images using penumbral or annular apertures have shown a reproducible spherical source of 50-μm mean diameter. Therefore, the penumbral aperture was displaced between various shots performed with this target. The reconstructed sources are presented in Fig. 112.97 and agree with the conclusion deduced from the Geant 4 calculations. The ±100-μm field of view defined by the intersection of the two cones of the penumbral aperture appears to be very effective.

In the future, we plan to reproduce these experiments with a ring aperture as Monte Carlo calculations predict enhanced image distortion with the source position in the field of view.

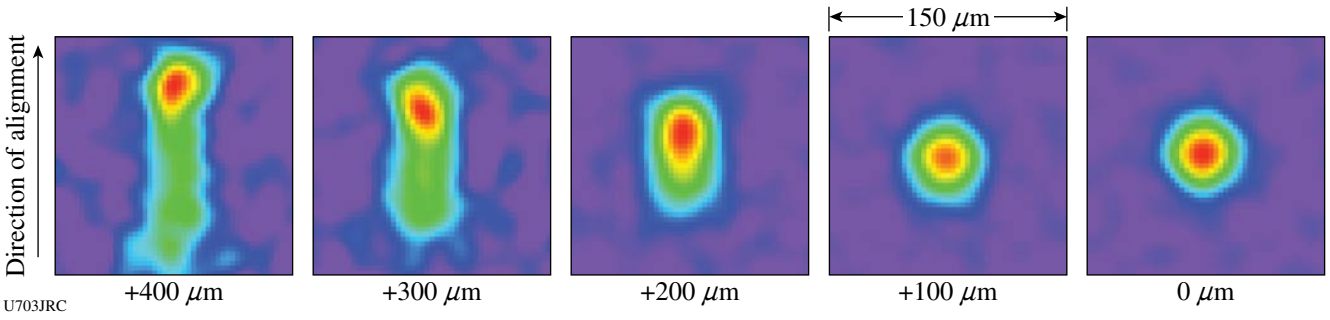

Figure 112.96
A 50-μm-diam neutron source at different locations in the field of view of a penumbral aperture using the Monte Carlo code Geant 4.

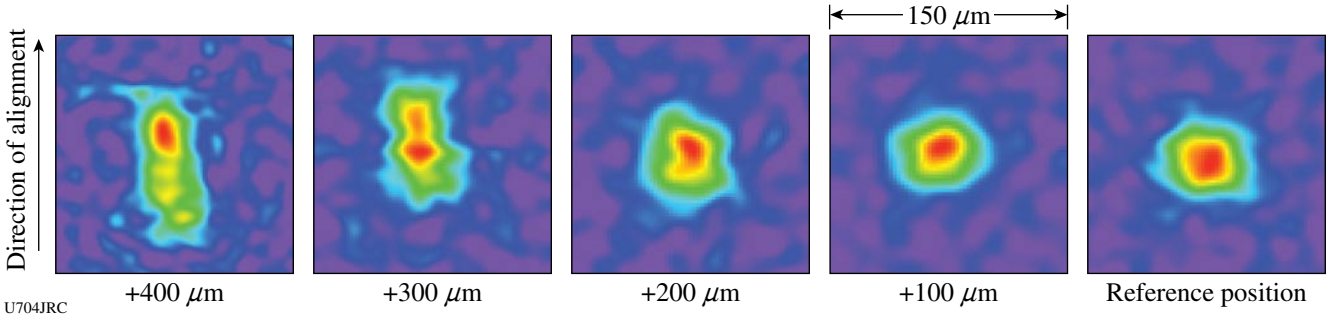

Figure 112.97
Experimental neutron images recorded at different positions in the field of view of a penumbral aperture. All images were recorded on a DT(15)CH[15] target implosion.

Also, the construction of a 150-mm-diam camera will allow us to record the image at a finer spatial resolution.

Neutron Flux and Duration Emission Measured with CVD Diamond Detectors: A series of chemical-vapor-deposition (CVD) diamond detectors have been implemented on OMEGA during a directly driven implosion of a DT capsule yielding 10^{13} to 10^{14} neutrons. These detectors discriminate neutrons by the time-of-flight technique and can provide a neutron-yield measurement after a calibration with the usual copper activation diagnostic. Neutron bang time and ion-temperature measurement can also be deduced from the probed signal as long as the diamond detectors exhibit temporal properties in the 100-ps range. Here the diamond devices used were grown and fabricated by CEA with controlled impurity levels (nitrogen, oxygen) that affect the sensitivity and the response time of the diamond detectors.[34] The relation between the level and nature of impurities with respect to the detector performances is, to date, empirical and has, therefore, required an experimental approach. These experiments have aimed at identifying the relevant characteristics of the diamond detectors to be suitable for neutron-yield, bang-time, and ion-temperature diagnostics.

Diamond detectors were inserted at distances of 30 cm, 1 m, and 2 m from the target chamber center using the TIM diagnostic insertion mechanisms. The distances and neutron-yield range provide the ability to probe the performances of the detectors within two decades of the neutron flux (n/cm^2). The detectors exhibit a linear response over the dynamic range explored. Sensitivity was also found reproducible on the A281103 diamond device tested in December 2005 and March 2007 (Fig. 112.98). Further, the diamond sensitivity can vary by a factor of 10^4 (Table 112.VII), which is mainly attributed to the material nature and the contribution of the added impurities since the geometrical dimensions of all detectors remained almost equal (3×3-mm^2 surface, 200 to 400 μm thick). Such results are essential to determine the required diamond detector characteristics as a function of location and detection volumes as NIF and LMJ experiments will require the neutron diagnostics to operate in the 10^{12} to 10^{18} neutron-yield range.[35]

The relative sensitivity between the diamonds as measured with the 14-MeV neutrons was also probed for comparison with 16-MeV electrons produced on a Linac accelerator at CEA (Bruyères le Châtel) (Fig. 112.99). A simple test on an electron

accelerator will make it possible to classify the diamond detectors prior to their installation on large ICF facilities.

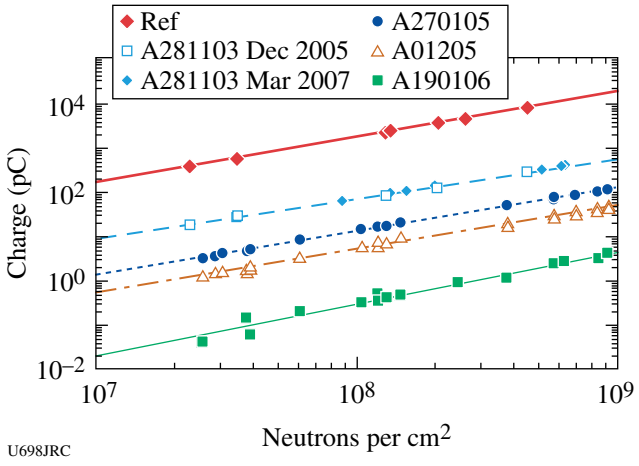

Figure 112.98
Linear response of a chemical-vapor-deposition (CVD) diamond measured on OMEGA.

The temporal properties of the detectors, such as rise time, FWHM, and decay time, were also measured from the short duration (25 ps) of the Linac electron pulses. Several diamond detectors show a 10% to 90% rise time below 100 ps and a subnanosecond decay time (Table 112.VIII). On OMEGA, the 150-ps-long neutron pulse makes it possible to measure the main temporal characteristics of the diamond detectors.

The detector signal propagates through 30 m of cable before reaching a 7-GHz-bandwidth single-shot oscilloscope (IN7100). After software removal of the dispersion caused by this cable, the diamond detector exhibits a signal duration at FWHM and a decay time comparable to those measured using the 16-MeV electrons. The signal rise time observed during DT implosions is, however, somewhat different since the neutron pulse duration at the detector position is determined by the 150-ps duration of the neutron source, convoluted with the temporal broadening induced by the DT ion's main energy at bang time. This ion-temperature effect is clearly observed on the signal rise time by probing the response at varying

Table 112.VII: Diamond sensitivity measured with a pulse of 14-MeV neutrons.

CVD	Type	Thickness	Size	Gold Contact	High Voltage	Sensitivity (C.n^{-1})
Ref	Monocrystalline	225 μm	4 × 4 mm	3 × 3 mm	–100 V	2.03×10^{-16}
A040406	Monocrystalline	260 μm	3 × 3 mm	2 × 2 mm	–750 V	4.15×10^{-18}
A281103	Polycrystalline	260 μm	5 × 5 mm	4 × 4 mm	–750 V	5.84×10^{-18}
A270105	Polycrystalline	250 μm	5 × 5 mm	4 × 4 mm	–750 V	1.06×10^{-18}
A010205	Polycrystalline	630 μm	5 × 5 mm	4 × 4 mm	–360 V	4.53×10^{-19}
A190106	Polycrystalline	450 μm	5 × 5 mm	4 × 4 mm	–500 V	2.70×10^{-20}

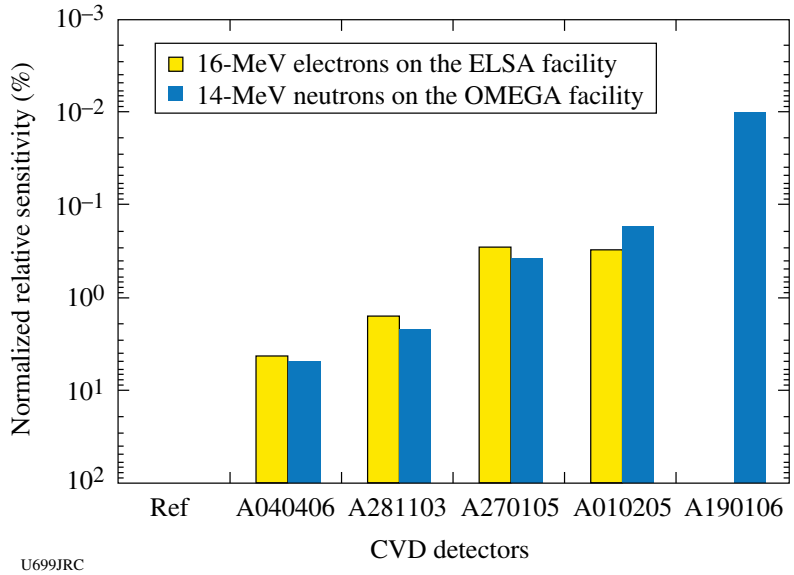

Figure 112.99
Comparison of electron and neutron relative sensitivity. All data are normalized by the most sensitive diamond "Ref."

Table 112.VIII: Temporal properties of diamond detectors as measured under 16-MeV electron pulses of 25-ps duration and 14-MeV neutron pulses of 150-ps duration.

CVD Detector	ELSA Facility 16-MeV Electrons			OMEGA Facility 14-MeV Neutrons		
	Rise (ps)	FWHM (ps)	Decay (ps)	Rise (ps)	FWHM (ps)	Decay (ps)
Ref	219	2870	4228	461	3508	4075
A040406	85	265	627	260	367	1340
A281103	134	434	772	226	442	688
A270105	73	297	608	164	318	601
A010205	86	178	540	133	241	322
A190106	n/a	n/a	n/a	150	266	917

distances—37 cm, 100 cm, or 200 cm—from the target (see Fig. 112.100—probed on the detector A270105).

Using the signal processing technique already used in the NTD diagnostics,[36] we deduce the neutron duration at 2 m from the target, which is mainly determined by the Doppler broadening produced by the ions. The resulting ion temperature and measured time duration are shown in the two last columns of Table 112.IX. For comparison, Table 112.IX also shows the ion temperature measured with the standard OMEGA system, performed at 5 m with a fast scintillator and an MCP photomultiplier. From these values, the time broadening (Δt) is deduced for a measurement at 2 m from target chamber center (TCC). The measured ion temperatures deduced from the CVD diamond at 2 m from the target are in good agreement with the standard OMEGA measurement.

A low-sensitivity CVD diamond with a high level of nitrogen impurity (A190106) demonstrates that diamond detectors can measure very high yield neutron for the NIF and LMJ. The

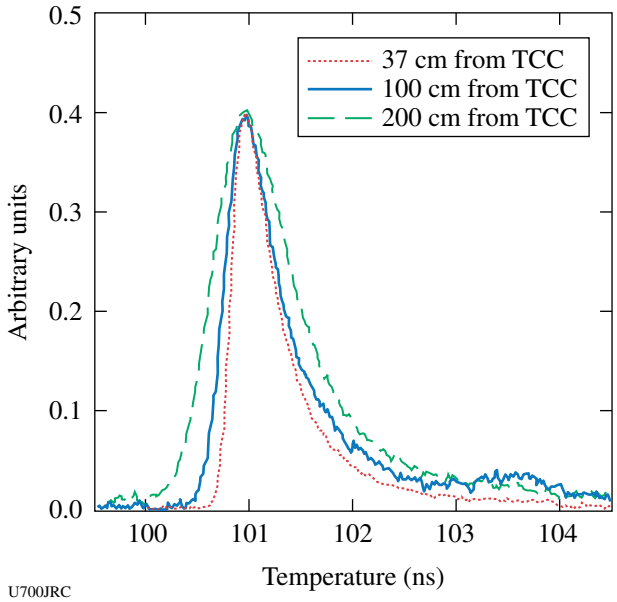

Figure 112.100
Doppler broadening of the neutron pulse.

Table 112.IX: Ion-temperature measurement at 2 m from TCC.

OMEGA Measurement			CVD Measurement		
N° Tir	T_i LLE (±0.5 keV)	Δt	CVD Reference	T_i Measured	Δt Measured
47539	3.4 keV	446 ps	A270105	3.8 keV	474 ps
			A010205	3.6 keV	456 ps
47540	3.6 keV	459 ps	A270105	3.5 keV	450 ps
			A010205	3.4 keV	449 ps
47549	5.4 keV	562 ps	A270105	5.5 keV	565 ps
			A010205	5.7 keV	576 ps
47550	5.1 keV	547 ps	A270105	5.0 keV	542 ps
			A010205	5.0 keV	542 ps

development of faster low-sensitivity CVD diamond detectors will continue with CEA-LIST and OMEGA. Ion-temperature measurement with CVD diamonds will be strengthened with future experiments.

One new challenging task will be to demonstrate the capability of a large, sensitive CVD diamond to measure the downscattered neutron yield for ρR determination.

FY07 AWE OMEGA Experimental Program

Radiation transport through enclosed spaces with inwardly moving walls is a key component of the physics of laser-heated hohlraums. It arises in the laser-heated cavity itself (where inward motion of the wall results in late-time stagnation of dense plasma on the hohlraum axis[37]) and also in the laser-entry and diagnostic holes (where an understanding of hole closure is important to hohlraum design and the interpretation of diagnostic data[38]). To better understand these phenomena, AWE (in collaboration with LLNL and General Atomics) successfully led two days of experiments on OMEGA during FY07.

A laser-heated hohlraum was used (Fig. 112.101) to illuminate annular slits machined in samples of solid-density tantalum and low-density, tantalum-oxide foam. In the first day of experiments (November 2006), the transmitted energy was measured indirectly (by measuring the temperature rise of a "calorimeter" hohlraum), directly (by measuring the emission from the tantalum-oxide component, using a target in which the calorimeter hohlraum was omitted), and by x-ray gated imaging of the slit. In the second series of experiments (May 2007), x-ray point-projection backlighting was used to determine the density distribution of plasma within a radiatively driven slit in solid-density tantalum. Figure 112.102 shows the measured temperature rise of the calorimeter hohlraum in comparison with radiation hydrocode simulation, for slits of two different widths and also for a sample of tantalum-oxide foam with no slit. Heating of the calorimeter arises from two sources: (1) x-ray transmission through the closing slit and (2) radiation burnthrough of the surrounding tantalum-oxide foam material. Both phenomena are modeled well by the simulation. Figure 112.103 shows point-projection radiographs of

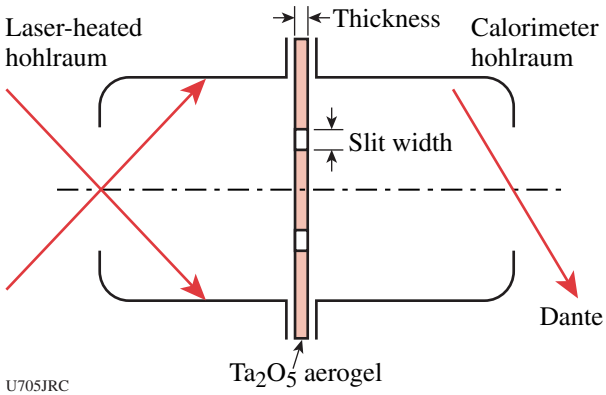

Figure 112.101
Schematic of the experiment to measure radiation transport through slits in low-density tantalum oxide and solid-density tantalum. One surface of the slit is heated by a scale-1.4 hohlraum target, and the transmitted energy either heats a "calorimeter" hohlraum or is measured directly (calorimeter not present). Radiographic measurements of the slit closure are made by point-projection backlighting along the hohlraum axis.

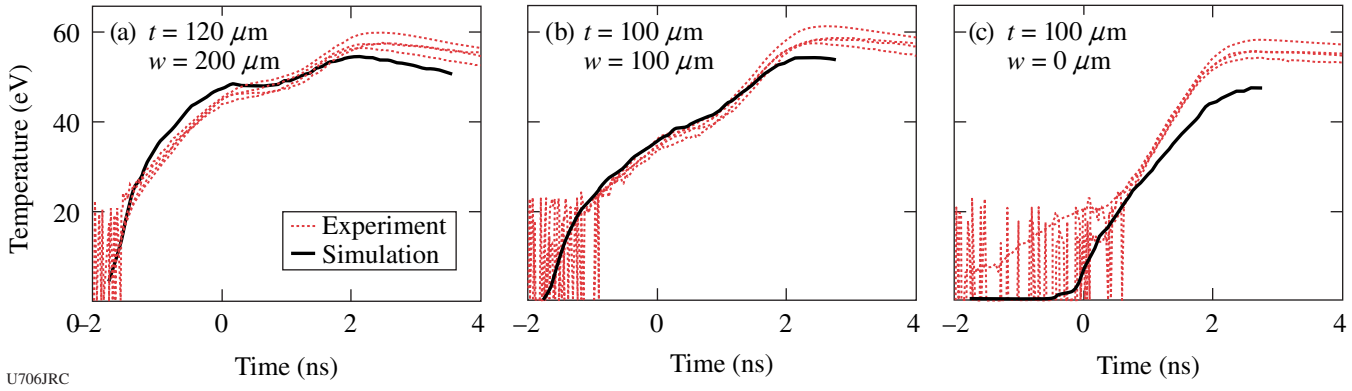

Figure 112.102
Temperature of the calorimeter hohlraum for experiments using low-density (0.25 g cm^{-3}) tantalum-oxide slits of (a) 120-μm thickness and 200-μm width, (b) 100-μm thickness and 100-μm width, and (c) 100-μm thickness with no slit. In each case the temperature inferred from four channels of the Dante diagnostic (a filtered x-ray diode array) is compared with simulation.

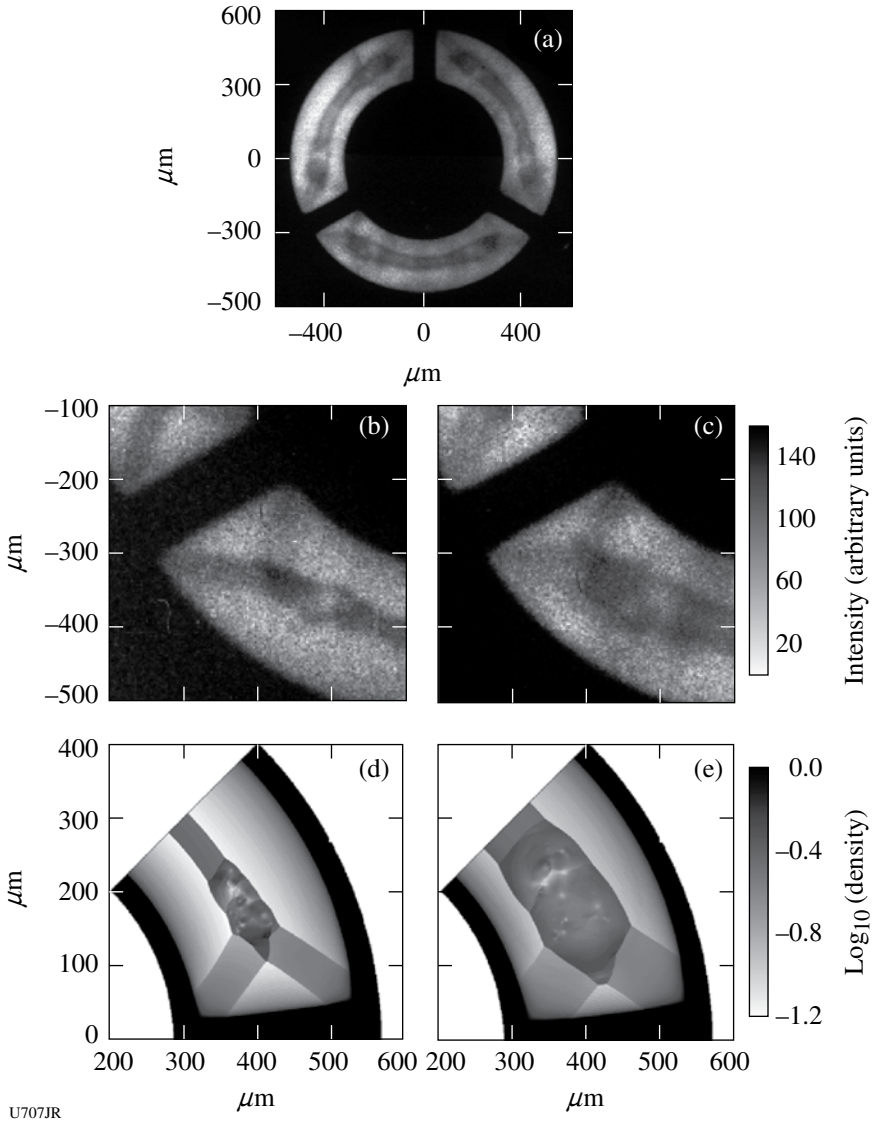

Figure 112.103
Point-projection radiographs of the closure of a 200-μm-wide slit in 50-μm-thick solid-density tantalum. (a) The deceleration shock and axial stagnation region within the slit are clearly visible. Images (b) and (c) are separated by 1.3 ns in time and show detail of the complex shock interactions in the corners bounded by the sides of the slit and the radial spokes supporting the central disk. Radiation hydrocode simulations (d) and (e) approximately reproduce this structure.

an annular slit in solid-density tantalum foil and comparison with a simulation in simplified (2-D Eulerian) geometry. The simulation approximately reproduces the deceleration shock and axial stagnation region at the center of the slit, as well as the complex shock interactions in the neighborhood of the radial spokes supporting the central disk. It is interesting to note that "N-wave" distributions of density, similar to the central stagnation region, also occur, in the astrophysical context, in stellar atmospheres[39,40] and that experiments of this type offer a potential laboratory platform for their investigation.

REFERENCES

1. S. Brygoo *et al.*, "Development of Quartz as an Impedance-Match Standard for Laser Shock Measurements in the Diamond Anvil Cell," submitted to the Journal of Applied Physics.

2. J. Eggert *et al.*, "Hugoniot Data for Helium in the Mbar Regime," to be published in Physical Review Letters.

3. G. W. Collins, Lawrence Livermore National Laboratory, private communication (2007).

4. D. Saumon and G. Chabrier, Phys. Rev. Lett. **62**, 2397 (1989).

5. S. A. Bonev, B. Militzer, and G. Galli, Phys. Rev. B **69**, 014101 (2004).
6. R. Jeanloz *et al*., Proc. Natl. Acad. Sci. USA **104**, 9172 (2007).
7. L. Stixrude and R. Jeanloz, "Fluid Helium at Conditions of Giant Planetary Interiors," submitted to the Proceedings of the National Academy of Sciences of the United States of America.
8. M. Ross, R. Boehler, and D. Errandonea, Phys. Rev. B **76**, 184117 (2007).
9. P. Celliers, Lawrence Livermore National Laboratory, private communication (2007).
10. J. M. Foster, B. H. Wilde, P. A. Rosen, R. J. R. Williams, B. E. Blue, R. F. Coker, R. P. Drake, A. Frank, P. A. Keiter, A. M. Khokhlov, J. P. Knauer, and T. S. Perry, Astrophys. J. Lett. **634**, L77 (2005).
11. R. F. Coker *et al*., Astrophys. Space Sci. **307**, 57 (2007).
12. C. K. Li, F. H. Séguin, J. A. Frenje, J. R. Rygg, R. D. Petrasso, R. P. J. Town, P. A. Amendt, S. P. Hatchett, O. L. Landen, A. J. Mackinnon, P. K. Patel, V. A. Smalyuk, T. C. Sangster, and J. P. Knauer, Phys. Rev. Lett. **97**, 135003 (2006).
13. C. K. Li, F. H. Séguin, J. A. Frenje, J. R. Rygg, R. D. Petrasso, R. P. J. Town, P. A. Amendt, S. P. Hatchett, O. L. Landen, A. J. Mackinnon, P. K. Patel, M. Tabak, J. P. Knauer, T. C. Sangster, and V. A. Smalyuk, Phys. Rev. Lett. **99**, 015001 (2007).
14. C. K. Li, F. H. Séguin, J. A. Frenje, J. R. Rygg, R. D. Petrasso, R. P. J. Town, O. L. Landen, J. P. Knauer, and V. A. Smalyuk, Phys. Rev. Lett. **99**, 055001 (2007).
15. C. K. Li, presented at the Fifth International Conference on Inertial Fusion Sciences and Applications, Kobe, Japan, 9–14 September 2007 (invited) (Paper ThO4.1).
16. R. Petrasso, Bull. Am. Phys. Soc. **52**, 97 (2007) (invited).
17. C. K. Li, F. H. Séguin, J. A. Frenje, J. R. Rygg, R. D. Petrasso, R. P. J. Town, P. A. Amendt, S. P. Hatchett, O. L. Landen, A. J. Mackinnon, P. K. Patel, V. Smalyuk, J. P. Knauer, T. C. Sangster, and C. Stoeckl, Rev. Sci. Instrum. **77**, 10E725 (2006).
18. J. F. Hansen, Lawrence Livermore National Laboratory, private communication (2007).
19. B. L. Henke *et al*., J. Opt. Soc. Am. B **1**, 818 (1984).
20. D. Vanderhaegen, J. Quant. Spectrosc. Radiat. Transf. **36**, 557 (1986).
21. G. C. Pomraning, J. Quant. Spectrosc. Radiat. Transf. **40**, 479 (1988).
22. G. C. Pomraning, *Linear Kinetic Theory and Particle Transport in Stochastic Mixtures*, Series on Advances in Mathematics for Applied Sciences, Vol. 7 (World Scientific, Singapore, 1991).
23. O. Haran, D. Shvarts, and R. Theiberger, Phys. Rev. E **61**, 6183 (2000).
24. C. C. Smith, J. Quant. Spectrosc. Radiat. Transf. **81**, 451 (2003).
25. P. D. Roberts *et al*., J. Phys. D: Appl. Phys. **13**, 1957 (1980).
26. P. Amendt *et al*., Bull. Am. Phys. Soc. **49**, 26 (2004).
27. W. A. Lokke and W. H. Grasberger, Lawrence Livermore National Laboratory, Livermore, CA, Report UCRL-52276, NTIS Order No. UCRL-52276 (1977).
28. J. R. Rygg, J. A. Frenje, C. K. Li, F. H. Séguin, R. D. Petrasso, J. A. Delettrez, V. Yu. Glebov, V. N. Goncharov, D. D. Meyerhofer, S. P. Regan, T. C. Sangster, and C. Stoeckl, Phys. Plasmas **13**, 052702 (2006).
29. D. C. Wilson *et al*., "The Effects of High Z Pre-Mix on Burn in ICF Capsules," submitted to the *Proceedings of the Fifth International Conference on Inertial Fusion Science and Applications (2007)* [to be published by Journal of Physics: Conference Series (Institute of Physics), London, England].
30. D. Ho *et al*., Bull. Am. Phys. Soc. **51**, 213 (2006).
31. R. E. Olson, R. J. Leeper, A. Nobile, J. A. Oertel, G. A. Chandler, K. Cochrane, S. C. Dropinski, S. Evans, S. W. Haan, J. L. Kaae, J. P. Knauer, K. Lash, L. P. Mix, A. Nikroo, G. A. Rochau, G. Rivera, C. Russell, D. Schroen, R. J. Sebring, D. L. Tanner, R. E. Turner, and R. J. Wallace, Phys. Plasmas **11**, 2778 (2003).
32. L. Disdier, A. Rouyer, I. Lantuéjoul, O. Landoas, J. L. Bourgade, T. C. Sangster, V. Yu. Glebov, and R. A. Lerche, Phys. Plasmas **13**, 056317 (2006).
33. A. Rouyer, Rev. Sci. Instrum. **74**, 1234 (2003).
34. P. Bergonzo, D. Tromson, and C. Mer, Semicond. Sci. Technol. **18**, S105 (2003).
35. V. Yu. Glebov, D. D. Meyerhofer, T. C. Sangster, C. Stoeckl, S. Roberts, C. A. Barrera, J. R. Celeste, C. J. Cerjan, L. S. Dauffy, D. C. Eder, R. L. Griffith, S. W. Haan, B. A. Hammel, S. P. Hatchett, N. Izumi, J. R. Kimbrough, J. A. Koch, O. L. Landen, R. A. Lerche, B. J. MacGowan, M. J. Moran, E. W. Ng, T. W. Phillips, P. M. Song, R. Tommasini, B. K. Young, S. E. Caldwell, G. P. Grim, S. C. Evans, J. M. Mack, T. Sedillo, M. D. Wilke, D. C. Wilson, C. S. Young, D. Casey, J. A. Frenje, C. K. Li, R. D. Petrasso, F. H. Séguin, J. L. Bourgade, L. Disdier, M. Houry, I. Lantuejoul, O. Landoas, G. A. Chandler, G. W. Cooper, R. J. Lepeer, R. E. Olson, C. L. Ruiz, M. A. Sweeney, S. P. Padalino, C. Horsfield, and B. A. Davis, Rev. Sci. Instrum. **77**, 10E715 (2006).
36. R. A. Lerche, D. W. Phillion, and G. L. Tietbohl, Rev. Sci. Instrum. **66**, 933 (1995).
37. R. T. Eagleton *et al*., Rev. Sci. Instrum. **68**, 834 (1997).
38. R. E. Chrien *et al*., Rev. Sci. Instrum. **70**, 557 (1999).
39. D. Mihalas and B. Weibel-Mihalas, *Foundations of Radiation Hydrodynamics* (Oxford University Press, New York, 1984).
40. T. K. Suzuki, Astrophys. J. **578**, 598 (2002).

Publications and Conference Presentations

Publications

A. C.-A. Chen, J. U. Wallace, K. P. Klubek, M. B. Madaras, C. W. Tang, and S. H. Chen, "Device Characteristics of Organic Light-Emitting Diodes Comprising Terfluorene Modified with Triphenyltriazine," Chem. Mater. **19**, 4043 (2007).

C. Dorrer, I. A. Begishev, A. V. Okishev, and J. D. Zuegel, "High-Contrast Optical-Parametric Amplifier as a Front End of High-Power Laser Systems," Opt. Lett. **32**, 2143 (2007).

C. Dorrer, A. V. Okishev, I. A. Begishev, J. D. Zuegel, V. I. Smirnov, and L. B. Glebov, "Optical Parametric Chirped-Pulse–Amplification Contrast Enhancement by Regenerative Pump Spectral Filtering," Opt. Lett. **32**, 2378 (2007).

H. Huang and T. Kessler, "Tiled-Grating Compressor with Uncompensated Dispersion for Near-Field-Intensity Smoothing," Opt. Lett. **32**, 1854 (2007).

I. V. Igumenshchev, V. N. Goncharov, W. Seka, D. Edgell, and T. R. Boehly, "The Effect of Resonance Absorption in OMEGA Direct-Drive Designs and Experiments," Phys. Plasmas **14**, 092701 (2007).

I. Kang and C. Dorrer, "Method of Optical Pulse Characterization Using Sinusoidal Optical Phase Modulations," Opt. Lett. **32**, 2538 (2007).

J. R. Marciante, W. R. Donaldson, and R. G. Roides, "Averaging of Replicated Pulses for Enhanced-Dynamic-Range Single-Shot Measurement of Nanosecond Optical Pulses," IEEE Photon. Technol. Lett. **19**, 1344 (2007).

J. Qiao, A. Kalb, M. J. Guardalben, G. King, D. Canning, and J. H. Kelly, "Large-Aperture Grating Tiling by Interferometry for Petawatt Chirped-Pulse–Amplification Systems," Opt. Express **15**, 9562 (2007).

E. Reiger, S. Dorenbos, V. Zwiller, A. Korneev, G. Chulkova, I. Milostnaya, O. Minaeva, G. Gol'tsman, J. Kitaygorsky, D. Pan, W. Słysz, A. Jukna, and R. Sobolewski, "Spectroscopy With Nanostructured Superconducting Single Photon Detectors," J. Sel. Top. Quantum Electron. **13**, 934 (2007).

S. N. Shafrir, J. C. Lambropoulos, and S. D. Jacobs, "Subsurface Damage and Microstructure Development in Precision Microground Hard Ceramics Using Magnetorheological Finishing Spots," Appl. Opt. **46**, 5500 (2007).

A. Simon, "Comment on 'Magnetic Field Effects on Gas Discharge Plasmas' [Phys. Plasmas 13, 063511 (2006)]," Phys. Plasmas **14**, 084703 (2007).

L. Sun and J. R. Marciante, "Filamentation Analysis in Large-Mode-Area Fiber Lasers," J. Opt. Soc. Am. B. **24**, 2321 (2007).

S. Wu, P. Geiser, J. Jun, J. Karpinski, and R. Sobolewski, "Femtosecond Optical Generation and Detection of Coherent Acoustic Phonons in GaN Single Crystals," Phys. Rev. B **76**, 085210 (2007).

C. D. Zhou and R. Betti, "Hydrodynamic Relations for Direct-Drive Fast-Ignition and Conventional Inertial Confinement Fusion Implosions," Phys. Plasmas **14**, 072703 (2007).

Forthcoming Publications

B. Ashe, C. Giacofei, G. Myhre, and A. W. Schmid, "Optimizing a Cleaning Process for Multilayer Dielectric (MLD) Diffraction Gratings," to be published in the Proceedings of SPIE.

J. E. DeGroote, A. E. Marino, J. P. Wilson, A. L. Bishop, and S. D. Jacobs, "Removal Rate Model for Magnetorheological Finishing (MRF) of Glass," to be published in Applied Optics.

C. Dorrer, "Analysis of Pump-Induced Temporal Contrast Degradation in Optical Parametric Chirped-Pulse Amplification," to be published in the Journal of the Optical Society of America B.

V. N. Goncharov, "Ablative Richtmyer–Meshkov Instability: Theory and Experimental Results," to be published in the Proceedings of Scottish Summer School.

V. N. Goncharov, "Direct-Drive Inertial Fusion: Basic Concepts and Ignition Target Designing," to be published in the Proceedings of Scottish Summer School.

O. V. Gotchev, N. W. Jang, J. P. Knauer, M. D. Barbero, and R. Betti, "Magneto-Inertial Approach to Direct-Drive Laser Fusion," to be published in the Journal of Fusion Energy.

W. Guan and J. R. Marciante, "Pump-Induced, Dual-Frequency Switching in a Short-Cavity, Ytterbium-Doped Fiber Laser," to be published in Optics Express.

C. Kim, J. U. Wallace, A. Trajkovska, J. J. Ou, and S. H. Chen, "Quantitative Assessment of Coumarin-Containing Polymer Film's Capability for Photoalignment of Liquid Crystals," to be published in Macromolecules.

D. N. Maywar, K. Solomon, and G. P. Agrawal, "Remote Optical Control of an Optical Flip-Flop," to be published in Optics Letters.

A. V. Okishev, C. Dorrer, V. I. Smirnov, L. B. Glebov, and J. D. Zuegel, "ASE Suppression in a Diode-Pumped Nd:YLF Regenerative Amplifier Using a Volume Bragg Grating," to be published in Frontiers in Optics 2007.

T. C. Sangster, R. L. McCrory, V. N. Goncharov, D. R. Harding, S. J. Loucks, P. W. McKenty, D. D. Meyerhofer, S. Skupsky, B. A. Hammel, J. D. Lindl, E. Moses, J. Atherton, G. B. Logan, S. Yu, J. D. Kilkenny, A. Nikroo, H. Wilken, K. Matzen, R. Leeper, R. Olsen, J. Porter, C. Barnes, J. C. Fernandez, D. Wilson, J. D. Sethian, and S. Obenschain, "Overview of Inertial Fusion Research in the United States," to be published in Nuclear Fusion.

S. N. Shafrir, J. C. Lambropoulos, and S. D. Jacobs, "Toward Magnetorheological Finishing of Magnetic Materials," to be published in the Journal of Manufacturing Science and Engineering.

C. Stoeckl, T. R. Boehly, J. A. Delettrez, S. P. Hatchett, J. A. Frenje, V. Yu. Glebov, C. K. Li, J. E. Miller, R. D. Petrasso, F. H. Séguin, V. A. Smalyuk, R. B. Stephens, W. Theobald, B. Yaakobi, and T. C. Sangster, "Hydrodynamics Studies of Direct-Drive, Cone-in-Shell, Fast-Ignitor Targets on OMEGA," to be published in Physics of Plasmas.

J. U. Wallace, R. H. Young, C. W. Tang, and S. H. Chen, "Charge-Retraction Time-of-Flight Measurement for Organic Charge Transport Materials," to be published in Applied Physics Letters.

D. Wang, A. S. Cross, G. Guarino, S. Wu, A. Mycielski, and R. Sobolewski, "Studies of Coherent Acoustic Phonons in CdMnTe Diluted-Magnetic Single Crystals," to be published in the Journal of Physics: Conference Series.

L. Welser-Sherrill, R. C. Mancini, J. A. Koch, N. Izumi, R. Tommasini, S. W. Haan, D. A. Haynes, I. E. Golovkin, J. A. MacFarlane, J. A. Delettrez, F. J. Marshall, S. P. Regan, and V. A. Smalyuk, and G. Kyrala, "Spectroscopic Determination of Temperature and Density Profiles and Mix in Indirect-Drive Implosion Cores," to be published in Physical Review E.

S. Wu, J. Zhang, P. Geiser, J. Jun, J. Karpinski, and R. Sobolewski, "Ultra-Long-Lived Coherent Acoustic Phonons in GaN Single Crystals," to be published in the Journal of Physics: Conference Series.

Conference Presentations

A. Trajkovska-Petkoska, T. Z. Kosc, K. L. Marshall, and S. D. Jacobs, "Electro-Optics of Polymer Cholesteric Liquid Crystal Flakes: Applications Toward Electronic Paper," ECLC 2007, 9th European Conference on Liquid Crystals, Lisbon, Portugal, 2–6 July 2007.

K. L. Marshall, A. Trajkovska-Petkoska, K. Hasman, M. Leitch, G. Cox, T. Z. Kosc, and S. D. Jacobs, "Polymer Cholesteric Liquid Crystal (PCLC) Flake/Fluid Host Electro-Optic Suspensions and Their Applications in Color Flexible Reflective Displays," International Display Manufacturing Conference 2007, Taipei, Taiwan, 3–6 July 2007.

T. Z. Kosc, A. Trajkovska-Petkoska, K. L. Marshall, S. D. Jacobs, K. Hasman, and C. Coon, "Polymer Cholesteric Liquid Crystal Flakes: A Novel Medium for Electro-Optical Particle-Based Technologies," Particles 2007, Toronto, Canada, 18–21 August 2007.

The following presentations were made at SPIE Optics and Photonics 2007, San Diego, CA, 26–30 August 2007:

J. E. DeGroote, A. E. Marino, J. P. Wilson, A. L. Bishop, and S. D. Jacobs, "The Role of Nanodiamonds in the Polishing Zone During Magnetorheological Finishing (MRF)."

K. L. Marshall, Z. Culakova, B. Ashe, C. Giacofei, A. L. Rigatti, T. J. Kessler, A. W. Schmid, J. B. Oliver, and A. Kozlov, "Vapor-Phase–Deposited Organosilane Coatings as 'Hardening' Agents for High Peak Power Laser Optics."

K. L. Marshall, R. Wang, M. Coan, A. G. Noto, K. Leskow, R. Pauszek, and A. Moore, "Using Time-Dependent Density Functional Theory (TDDFT) in the Design and Development of Near-IR Dopants for Liquid Crystal Device Applications."

C. Miao, K. M. Bristol, A. E. Marino, S. N. Shafrir, J. E. DeGroote, S. D. Jacobs, "Magnetorheological Fluid Template for Basic Studies of Mechanical-Chemical Effects During Polishing."

S. N. Shafrir, J. C. Lambropoulos, and S. D. Jacobs, "MRF Spotting Technique for Studying Subsurface Damage in Deterministic Microground Polycrystalline Alumina."

The following presentations were made at the 37th Anomalous Absorption Conference, Maui, HI, 27–31 August 2007:

J. A. Delettrez, V. N. Goncharov, P. B. Radha, C. Stoeckl, A. V. Maximov, T. C. Sangster, D. Shvarts, R. D. Petrasso, and J. A. Frenje, "Simulations of the Effect of Energetic Electrons Produced from Two-Plasmon Decay in the 1-D Hydrodynamics Code *LILAC*."

D. H. Edgell, W. Seka, J. A. Delettrez, R. S. Craxton, V. N. Goncharov, I. V. Igumenshchev, J. Myatt, A. V. Maximov, R. W. Short, T. C. Sangster, and R. E. Bahr, "Time-Dependent Spectral Shifts of Scattered Laser Light in Direct-Drive Inertial Confinement Fusion Implosion Experiments."

D. H. Edgell, W. Seka, V. N. Goncharov, I. V. Igumenshchev, R. S. Craxton, J. A. Delettrez, J. Myatt, A. V. Maximov, and R. W. Short, "Time-Resolved Scattered-Light Spectroscopy in Direct-Drive Implosion Experiments."

M. G. Haines and J. Myatt, "Competition Between the Resistive Weibel Instability and the Electrothermal Instability in Fast Ignition."

A. V. Maximov, J. Myatt, R. W. Short, W. Seka, and C. Stoeckl, "Modeling of Two-Plasmon-Decay Instability Under Incoherent Laser Irradiation."

J. Myatt, P. Nilson, W. Theobald, M. Storm, A. V. Maximov, and R. W. Short, "Determination of Hot-Electron Conversion Efficiency and Isochoric Heating of Low-Mass Targets Irradiated by the Multi-Terawatt Laser."

W. Seka, D. H. Edgell, J. P. Knauer, C. Stoeckl, V. N. Goncharov, I. V. Igumenshchev, J. A. Delettrez, J. Myatt, A.V. Maximov, R. W. Short, and T. C. Sangster, "Laser–Plasma Interaction Processes Observed in Direct-Drive Implosion Experiments."

R. W. Short and J. Myatt, "Modeling the Filamentation Instability of Relativistic Electron Beams for Fast Ignition."

D. Shvarts, V. A. Smalyuk, R. Betti, J. A. Delettrez, D. H. Edgell, V. Yu. Glebov, V. N. Goncharov, R. L. McCrory, P. W. McKenty, D. D. Meyerhofer, F. J. Marshall, P. B. Radha, T. C. Sangster, W. Seka, S. Skupsky, C. Stoeckl, B. Yaakobi, J. A. Frenje, C. K. Li, R. D. Petrasso, and F. H. Séguin, "The Role of Fast-Electron Preheating in Low-Adiabat Cryogenic and Plastic (CH) Shell Implosions on OMEGA."

V. A. Smalyuk, D. Shvarts, R. Betti, J. A. Delettrez, D. H. Edgell, V. Yu. Glebov, V. N. Goncharov, S. X. Hu, F. J. Marshall, R. L. McCrory, P. W. McKenty, D. D. Meyerhofer, P. B. Radha, T. C. Sangster, W. Seka, S. Skupsky, C. Stoeckl, B. Yaakobi, J. A. Frenje, C. K. Li, R. D. Petrasso, and F. H. Séguin, "Effects of Hot-Electron Preheat in Direct-Drive Experiments on OMEGA."

A. A. Solodov, K. S. Anderson, R. Betti, V. Gotcheva, J. Myatt, J. A. Delettrez, and S. Skupsky, "Integrated Simulation of Fast-Ignition ICF."

The following presentations were made at IFSA 2007, Kobe, Japan, 9–14 September 2007:

R. Betti, W. Theobald, C. D. Zhou, K. S. Anderson, P. W. McKenty, D. Shvarts, and C. Stoeckl, "Shock Ignition of Thermonuclear Fuel with High Areal Densities."

V. N. Goncharov, P. B. Radha, R. Betti, T. J. B. Collins, J. A. Delettrez, R. Epstein, S. X. Hu, I. V. Igumenshchev, R. L. McCrory, P. B. McKenty, D. D. Meyerhofer, S. P. Regan, T. C. Sangster, W. Seka, S. Skupsky, V. A. Smalyuk, and D. Shvarts, "Modeling High-Compression, Direct-Drive ICF Experiments."

D. R. Harding, D. D. Meyerhofer, T. C. Sangster, S. J. Loucks, R. L. McCrory, R. Betti, J. A. Delettrez, D. H. Edgell, L. M. Elasky, R. Epstein, V. Yu. Glebov, V. N. Goncharov, S. X. Hu, I. V. Igumenshchev, D. Jacobs-Perkins, R. J. Janezic, J. P. Knauer, L. D. Lund, J. R. Marciante, F. J. Marshall, D. N. Maywar, P. W. McKenty, P. B. Radha, S. P. Regan, R. G. Roides, W. Seka, W. T. Shmayda, S. Skupsky, V. A. Smalyuk, C. Stoeckl, B. Yaakobi, J. D. Zuegel, D. Shvarts, J. A. Frenje, C. K. Li, R. D. Petrasso, and F. H. Séguin, "Cryogenic Target-Implosion Experiments on OMEGA."

D. N. Maywar, J. H. Kelly, L. J. Waxer, S. F. B. Morse, I. A. Begishev, J. Bromage, C. Dorrer, J. L. Edwards, L. Folnsbee, M. J. Guardalben, S. D. Jacobs, R. Jungquist, T. J. Kessler, R. W. Kidder, B. E. Kruschwitz, S. J. Loucks, J. R. Marciante, R. L. McCrory, D. D. Meyerhofer, A. V. Okishev, J. B. Oliver, G. Pien, J. Qiao, J. Puth, A. L. Rigatti, A. W. Schmid, M. J. Shoup, III, C. Stoeckl, K. A. Thorp, and J. D. Zuegel, "OMEGA EP High-Energy Petawatt Laser: Progress and Prospects."

P. W. McKenty, T. J. B. Collins, J. A. Marozas, S. Skupsky, D. R. Harding, J. D. Zuegel, D. Keller, A. Shvydky, D. D. Meyerhofer, and R. L. McCrory, "Multidimensional Numerical Investigation of NIF Polar-Direct-Drive Designs with Full Beam Smoothing."

S. P. Regan, T. C. Sangster, D. D. Meyerhofer, W. Seka, R. Epstein, S. J. Loucks, R. L. McCrory, C. Stoeckl, V. Yu. Glebov, O. S. Jones, D. Callahan, P. A. Amendt, N. B. Meezan, L. J. Suter, M. D. Rosen, O. L. Landen, E. L. DeWald, S. H. Glenzer, C. Sorce, S. Dixit, R. E. Turner, and B. MacGowan, "Hohlraum Energetics and Implosion Symmetry with Elliptical Phase Plates Using a Multi-Cone Beam Geometry on OMEGA."

D. Shvarts, V. A. Smalyuk, R. Betti, J. A. Delettrez, D. H. Edgell, V. Yu. Glebov, V. N. Goncharov, R. L. McCrory, P. W. McKenty, D. D. Meyerhofer, F. J. Marshall, P. B. Radha, S. P. Regan, T. C. Sangster, W. Seka, S. Skupsky, C. Stoeckl, B. Yaakobi, J. A. Frenje, C. K. Li, R. D. Petrasso, and F. H. Séguin, "The Role of Fast-Electron Preheating in Low-Adiabat Cryogenic Implosions on OMEGA."

S. Skupsky, V. N. Goncharov, and D. Li, "Nonlocal Ion-Heat and Momentum Transport in ICF Implosions."

A. V. Okishev, C. Dorrer, V. I. Smirnov, L. B. Glebov, and J. D. Zuegel, "ASE Suppression in a Diode-Pumped Nd:YLF Regenerative Amplifier Using a Volume Bragg Grating," Frontiers in Optics 2007/Laser Science XXIII, San Jose, CA, 16–20 September 2007.

The following presentations were made at the 8th International Conference on Tritium Science and Technology, Rochester, NY, 16–21 September 2007:

T. Duffy, R. Janezic, and W. T. Shmayda, "LLE's High-Pressure DT-Fill-Process Control System."

R. T. Janezic, W. T. Shmayda, G. P. Wainwright, P. Regan, K. Lintz, D. R. Harding, and S. J. Loucks, "Operational Experience of Tritium Handling During LLE's Cryogenic Target Filling Operation."

W. T. Shmayda, S. J. Loucks, R. T. Janezic, G. P. Wainwright, and T. Duffy, "Tritium Management on OMEGA at the Laboratory for Laser Energetics."

W. T. Shmayda, C. R. Shmayda, C. Waddington, and R. D. Gallagher, "Operation of a 2.6-Mg/Year Heavy-Water Detritiation Plant."

G. P. Wainwright, W. T. Shmayda, R. T. Janezic, and P. Regan, "Tritium Capture with Getter-Bed Technology at the Laboratory for Laser Energetics."

D. N. Maywar, "Optical Control of Flip-Flops Based on Resonant-Type SOA's," University of Tokyo Seminar, Tokyo, Japan, 18 September 2007.

The following presentations were made at the Boulder Damage Symposium, Boulder, CO, 24–26 September 2007:

B. Ashe, C. Giacofei, G. Myhre, and A. W. Schmid, "Optimizing a Cleaning Process for Multilayer Dielectric (MLD) Diffraction Gratings."

S. Papernov, A. W. Schmid, J. B. Oliver, and A. L. Rigatti, "Damage Thresholds and Morphology of the Front- and Back-Irradiated SiO_2 Thin Films Containing Gold Nanoparticles as Artificial Absorbing Defects."